MODEL-BASED ESTIMATION TECHNIQUES APPLIED TO GLOBAL NAVIGATION SATELLITE SYSTEM JAMMERS

A Dissertation

Presented to the Faculty of the Graduate School

of Cornell University

in Partial Fulfillment of the Requirements for the Degree of

Doctor of Philosophy

by

Ryan Harris Mitch

May 2014

MODEL-BASED ESTIMATION TECHNIQUES APPLIED TO GLOBAL NAVIGATION SATELLITE SYSTEM JAMMERS

Ryan Harris Mitch, Ph.D.

Cornell University 2014

Model-based estimation techniques have been developed and applied to data collected from real Global Navigation Satellite System (GNSS) jammers. Low-power civilian GNSS jammers pose a growing threat to the integrity of GNSS timing and navigation, and the present effort develops various countermeasures for these devices. The use of illegal civilian GNSS jammers has grown in recent years out of concern for personal privacy, sometimes on the part of innocents, but often in support of unauthorized or illegal activities. These civilian jammers are commonly referred to as personal privacy devices (PPDs). The effects of these PPDs are not limited to the individual user; they disrupt GNSS-enabled equipment in a radius of 100m–1000m or more around each device. GNSS systems are being further integrated into many aspects of our society; therefore, the rise in PPD use portends trouble for various pieces of civilian infrastructure. PPD use can be discouraged through more rigorous enforcement of spectrum interference laws. These enforcement actions will require specially designed equipment, and in particular, algorithms to be run by that equipment: algorithms that detect, acquire, track, and geolocate these PPDs.

Six contributions are made to the body of knowledge on PPDs and the model-based algorithms related to PPD signal detection, acquisition, and tracking, and to PPD geolocation. However, many of these contributions can be generalized to additional non-PPD signals. The first contribution is a survey of the signal characteristics of 18 different. The second contribution is a sensible

chirp-style signal model for the PPDs. The third contribution is a sensitive PPD chirp-style signal detection algorithm that has been extensively optimized for low computational burden. The fourth contribution is a two-part FFT-based signal acquisition procedure that can rapidly acquire a full state estimate of the target PPD using the data provided by the signal detection algorithm. The fifth contribution is a signal tracking Kalman filter for estimating the states of the received PPD signal. The sixth contribution is a time-of-arrival geolocation algorithm that enables low-bandwidth inter-receiver array communication. All of the developed algorithms have been verified on real PPD data collected in a laboratory or in the field.

BIOGRAPHICAL SKETCH

Ryan Mitch was born in Pittsburgh, PA. He is an identical twin. He spent four years at the University of Pittsburgh and eventually graduated with a B.S. in Mechanical Engineering. Upon graduation, he immediately enrolled in the graduate program at Cornell University's Sibley School of Mechanical and Aerospace Engineering, where he received his M.S. in Mechanical Engineering in 2012. He has been fortunate to receive the award for the best presentation in his session in three out of the four conferences he has attended, an Honorable Mention from the NSF Graduate Fellowship Research Program in 2010, an Honorable Mention for the Sibley Prize for Excellence in Graduate Teaching in 2012, and the NASA Space Grant Graduate Fellowship in 2012. He has recently been hired by the Johns Hopkins University Applied Physics Laboratory.

I dedicate this work to my family and friends. I rarely let them know what they mean to me; I love them all.

ACKNOWLEDGEMENTS

I would like to acknowledge the New York Space Grant Consortium for the NASA Space Grant Graduate Fellowship that funded me for one year of my graduate research.

I would also like to acknowledge the following two groups for providing me with the opportunity to verify my algorithms on real data. The Department of Homeland Security provided the PPDs used in this work, and they sponsored a jamming event at White Sands Missile Range. The U.S. Airforce's 746th test squadron prepared and operated those same jammers at White Sands Missile Range.

My associates at the University of Texas at Austin were extremely helpful at various stages throughout my graduate career. In particular, the efforts of Todd Humphreys, Jahshan Bhatti, Daniel Shepard, and Reese Shetrone at White Sands Missile Range were critical to the successful PPD data collection campaign.

Everyone in the Cornell GPS laboratory has been helpful and supportive during my time as a graduate student. Joanna Hinks provided great advice during my first few years at the Cornell GPS laboratory. Stephen Powell and Brady O'Hanlon were crucial to the design and execution of the jamming test at White Sands Missile Range, and they have provided me with technical advice on numerous topics. Ryan Dougherty has been a valuable partner for technical discussions during my entire graduate career. Ryan Dougherty and Tunc Ertan have both made contributions to some of the results presented in this thesis.

Most importantly, I would like to acknowledge my advisor Mark Psiaki. He is the most technically sound engineer that I have ever met and he has provided me with years of guidance of both a technical and personal nature.

TABLE OF CONTENTS

LIST OF TABLES

LIST OF FIGURES

CHAPTER 1

INTRODUCTION

The use of a personal privacy device (PPD) that jams GPS and other GNSS signals is illegal in many countries. However, the interests of individuals or groups willing to break the law may be served by interfering with the normal operation of GNSS-enabled systems. Three common examples of PPD are presented here for motivation, but other uses exist, and future uses are likely to emerge. First, a car or truck thief may wish to prevent geolocation of a GNSS-equipped stolen vehicle by the owner or by law-enforcement authorities [10]. Second, a tractor trailer driver may wish to stop the constant location-based scrutiny provided by an automated GNSS route logger that has been installed in his corporate vehicle. Third, a vehicle owner may wish to disable a GNSS-based speed logging device provided by his/her insurance company. That person may want to go above the speed limit, and PPDs provide the means to prevent the insurance company from knowing that he/she has driven faster than allowed by law. The use of the PPD will prevent his/her insurance rates from being altered by the insurance company due to his/her speeding.

In recent years, many GNSS jamming devices have become available for purchase over the Internet. These relatively cheap devices, some costing less than an inexpensive GNSS receiver, pose a significant risk to the normal operation of many systems reliant on GNSS. For example, the ground-based augmentation system for GPS at Newark International Airport experienced serious disruptions from a PPD that was used by a trucker to thwart GPS-based monitoring by his firm.

If the use of PPDs continues to increase, and they eventually become commonplace, then PPDs could cause GNSS-reliant systems to be unreliable, perhaps to the point of being useless. This scenario can be characterized as ex-

treme. However, even a small number of PPDs in a moderately sized town can hamper society's progress towards increased exploitation of ubiquitous position, navigation, and time (PNT) services. A society that can confidently rely on knowledge of its PNT is one that can enable the next generation of technological integration in our daily lives, via smart-phones, watches, glasses, autonomous vehicles, and other yet-to-be-developed applications. Society's dependence on GNSS has become so pervasive that many people in the navigation community have even begun to consider it as a government-provided utility, similar to water and electricity.

The problem posed by PPDs should be considered thoroughly. This thesis seeks to provide some of the necessary background information on PPDs that should be used in this consideration. It also provides some new algorithms that can be used to address PPD interference. These algorithms are developed using experimental understanding of PPDs and models that capture much of this understanding. The algorithms use the models to detect, acquire, track, and geolocate PPDs. The initial experiments, the PPD models, the resulting algorithms, and experimental evaluations of these algorithms are treated in-depth in the following chapters. Most of the technical challenges encountered in this thesis are addressed using tools from state-space modeling, probability theory, model-based estimation, optimization theory, and signal tracking theory. Emphasis has been placed on the verification of the developed algorithms using real data.

The remainder of this dissertation is organized as follows. Chapter 2 provides extensive background information on the PPDs, and it discusses the collection of their emitted signals during two different efforts: a laboratory campaign and a field campaign. Chapter 3 provides a new high-fidelity state-space model of the PPDs' chirp-style signals, both for a single jammer and for multi-

ple jammers. Chapter 4 develops a new PPD signal detection algorithm. The optimization of the computational load of the detection algorithm is treated in-depth. Chapter 5 uses the results of the detection test as *a priori* information for a new two-part signal acquisition procedure: a rough acquisition, followed by a fine acquisition. Chapter 6 develops a PPD chirp-style signal tracking Kalman filter that makes use of FFT-based measurements. Chapter 7 develops a low-dimensional PPD geolocation algorithm that uses many of the algorithms that have been developed in the earlier chapters.

CHAPTER 2

BACKGROUND AND DATA COLLECTION

Many types of intentional radio frequency (RF) interference exist, including tones, swept waveforms, pulses, narrowband noise, and broadband noise. There are a number of methods for mitigating the effects of jamming and interference, and additional methods exist to locate the sources of the interference. Mitigation and location methods can be improved by use of *a priori* information about the interference source.

This chapter provides such *a priori* information for a set of jammers and assesses their threats. This chapter's results are based on two tests. The first test records raw RF data from a selection of jammers and analyzes it using fast Fourier transform (FFT) spectral methods. The second test evaluates the effective range of a subset of the GPS jammers using a commercial off-the-shelf (COTS) receiver. The article presents results based on 18 different civil GPS jammers provided by the U.S. Department of Homeland Security. Note, there are other types of GPS jammers for sale that were not tested. Furthermore, civil jammer behavior and design is likely to evolve over time. Additional information on some PPDs can be found in [9, 26], and their impacts on GNSS equipment in [20, 43]. In this chapter, conclusions are drawn based only on the tested jammers. Note, this work was originally published in [36].

2.1 Overview of Civil GPS Jammers

Devices that claim to jam or block GPS signals are widely available through a number of websites and online entities. The cost of these devices ranges from a few tens of dollars to several hundred. Their price does not seem to correlate with the claims made by the purveyors of these devices regarding the features and effectiveness of the product in question. Effective ranges from a few meters

to several tens of meters are advertised, but the actual effective ranges are significantly greater. Claimed and true power consumptions range from a fraction of a watt to several watts.

The GPS jammers are categorized into 3 groups based on physical appearance. The first is a group of jammers designed to plug into an automotive 12-volt auxiliary power supply outlet (cigarette lighter socket); this class of jammer is referred to in the remainder of this chapter as Group 1. The second category contains those jammers that are both powered by an internal rechargeable battery and that have an external antenna connected via an SMA connector; these jammers are referred to as Group 2. The jammers in Group 3 are disguised as cell phones; they have batteries but no external antennas. Figure 2.1 shows an example of a device from each of Groups 1–3.

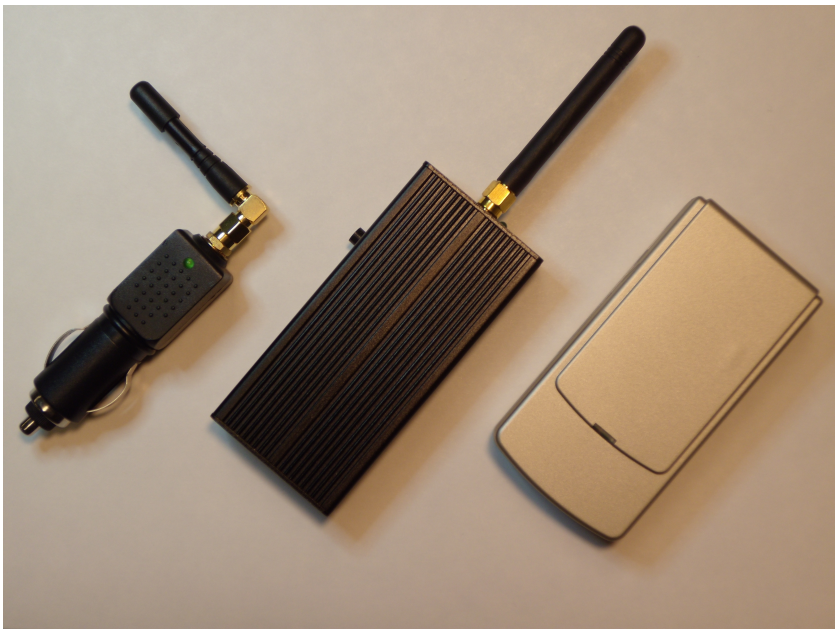

Figure 2.1: Three jammers are depicted, from left to right: Jammers 1, 5, and 15 from Groups 1, 2, and 3, respectively.

All 18 jammers broadcast power at or near the L_1 carrier frequency, six broadcast power at or near the L_2 carrier frequency, and none broadcast power at or near the L_5 carrier frequency. Some of the jammers also broadcast power at

frequencies outside of the GPS bands, typically cellular phone or Wi-Fi bands, but those frequencies are outside the scope of this work. Results in this chapter are for the current power levels broadcast in the GPS L_1 and L_2 bands, but examination of power levels in non- GPS bands indicate that many of these devices could be easily modified to broadcast much more power in the GPS bands.

The jammer antennas have been removed in most of the testing for this chapter, but their use in a real-world scenario will modify the jammer behavior. The antennas used by Group 1 and Group 2 jammers are loaded monopole antennas, Fig. 2.2. The antennas used by the Group 3 jammers are electrically short helical antennas that have approximately the same gain pattern as the loaded monopoles, Fig. 2.3. A ruler has been included in Figs. 2.2 and 2.3 to provided a reference for the size of the antennas. These antennas broadcast linearly polarized radiation, as opposed to the right-hand circular polarization of GPS signals. The polarization mismatch will cause some loss in received power at a right-hand circularly polarized GPS receiver antenna.

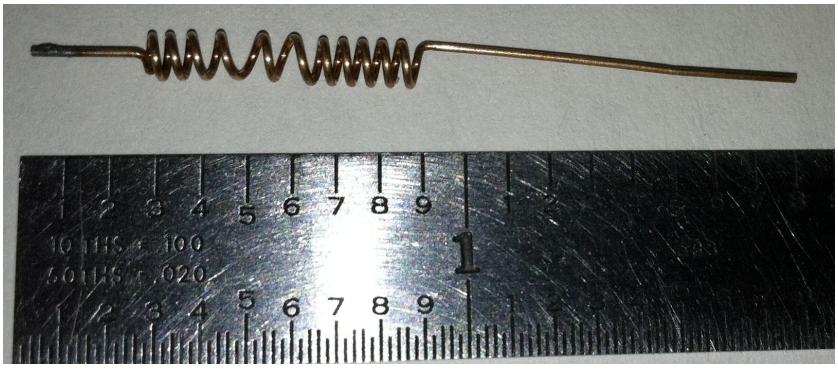

Figure 2.2: The antenna type used by the jammers in Groups 1 and 2.

2.2 Jammer Signal Characteristics Test

The goal of the first set of tests was to record complex samples of the jamming signals and to derive the jammer characteristics from these data. A two-step

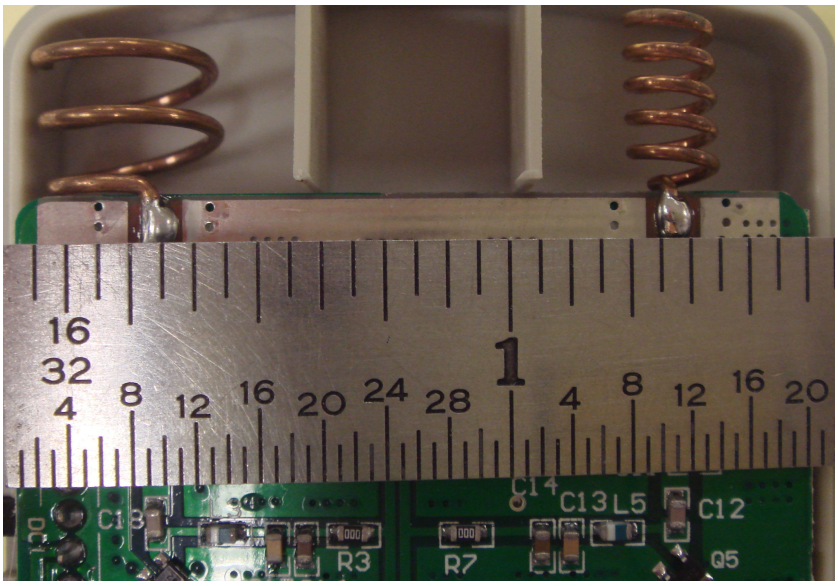

Figure 2.3: The antenna type used by the jammers in Groups 3.

procedure was used to collect useful data. The first step used a spectrum analyzer to find the frequency range of the jamming signal near L_1 and L_2. The spectrum analyzer is shown in Fig. 2.4. The second step used this frequency information to set the center frequency of a general-purpose RF digitization and signal storage device with a 12-drive RAID storage array. The setup for recording the RF data in step two is shown in Fig. 2.5. The data recording system is displayed on the left side of the picture. The box on the right side of the picture is discussed in the next paragraph. Offline analyses were then conducted on the recorded data.

The test procedure was as follows. For the first two groups, the jammer was placed inside an RF-shielded test enclosure shown in the right side of Fig. 2.5 and in more detail in Fig. 2.6, to prevent any signal leakage. The jammer's SMA signal output port was connected to the relevant data collection device using a shielded coaxial cable. The signal had to pass from the inside to the outside of the RF enclosure using the built-in coaxial feed-through. Note, therefore, that no jammer signal radiation occurred for Group 1 and 2 jammers even inside the

Figure 2.4: The spectrum analyzer used to determine the frequencies with appreciable jammer power.

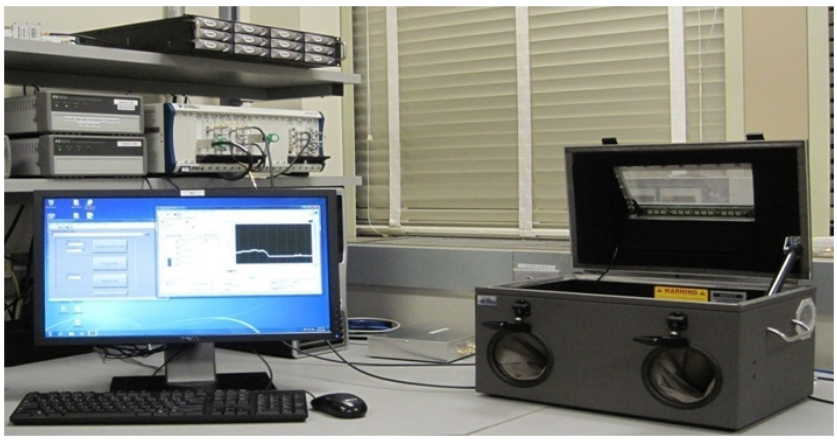

Figure 2.5: The laboratory setup used in the recording of the jammer signals.

RF enclosure. The enclosure was used primarily as a precaution.

Figure 2.6: RF-shielded test enclosure. Jammers were operated inside the enclosure to prevent emission of their RF signals.

None of the Group 3 jammers had external antennas. Therefore, they were allowed to radiate in the RF enclosure using their internal antennas. To capture the signal, a receiving patch antenna with active amplification was placed in the RF enclosure, and the antenna output was connected to the relevant RF recording device via the enclosure's coaxial feed-through. The jammer and receiving antenna were separated by about 14 centimeters. The antenna separation was short enough that near-field effects could affect some of this test's results. The patch antenna field-of-view center was pointed directly at the jammer. The jammer was oriented such that the axis of its helical antenna was pointed perpen-

dicular to the line from the receiving antenna to the jammer, i.e., the antenna was oriented so that the gain was maximized between the antennas.

2.3 Jammer Signal Characteristics Test Results

Although 18 jammers were tested, only a representative subset is discussed here. The signals were analyzed using FFT spectral methods and measurements of in-band power. Figure 2.7 displays the results of this analysis for a typical jammer from Group 1.

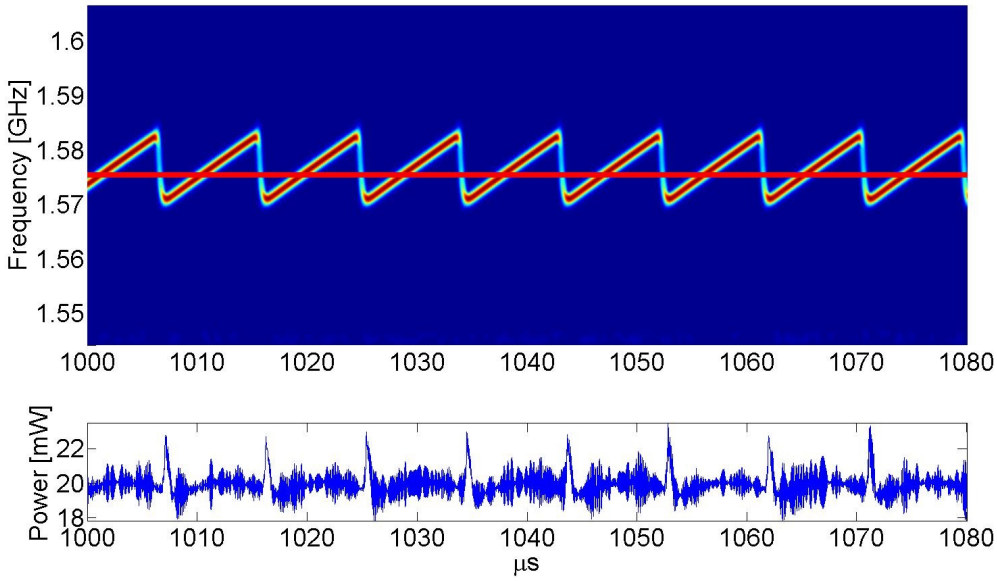

Figure 2.7: Jammer 4 power spectral density versus time, with color indicating relative power (top plot) and power versus time in a 62.5-MHz band centered at the L_1 carrier frequency (bottom plot). The horizontal red line in the top plot indicates the GPS L_1 frequency.

The top plot of Fig. 2.7 graphs frequency on the vertical scale versus time on the horizontal scale. The bottom plot graphs power on the vertical scale versus time on the horizontal scale. Each vertical slice of the recorded RF data plot is a single FFT frequency spectrum. It covers 62.5 MHz centered on the L_1

band and has a resolution of approximately 1 MHz. The relative power spectral density of each slice is indicated by color. The time axes of both plots span 80 microseconds.

The upper plot of Fig. 2.7 is that of a linear frequency modulation interspersed with rapid resets—a series of linear chirps. Each sweep takes nine microseconds and spans a range of about 14 MHz. This range includes the civil L_1 GPS band. The center frequency is depicted by the horizontal red line in the top plot. The power is about 20 milliwatts and remains fairly constant over the sweep.

Three of the Group 1 jammers appeared to be of the same model and one was slightly different. All of them broadcast power only at the L_1 frequency. Despite their similarities in external appearance, the three jammers of the same model exhibited markedly different signal properties. These differences will be presented later in terms of tabulated frequency modulation characteristics and in-band power levels.

One of the Group 2 jammers was unusual in two respects, as illustrated in Fig. 2.8. This figure plots the L_2 spectrum whose center is indicated by the horizontal red line in the top plot. The first obvious difference from Fig. 2.7 is that the frequency modulation in time is more accurately described as a triangular wave instead of a chirp. Additionally, the modulation frequency is very high in comparison to all of the other jammers; its period is only about 1 microsecond. Note that the horizontal scale of this figure spans only 8 microseconds, that is, 10 times less than in Fig. 2.7.

The other Group 2 jammers tended to broadcast chirp frequency modulations as in Fig. 2.7. They all broadcast jamming power at L_1. The jammer depicted in Fig. 2.7 broadcast power at L_2 as well. Only one other Group 2 jammer had L_2 jamming capability. Two of the jammers suffered from poor design of

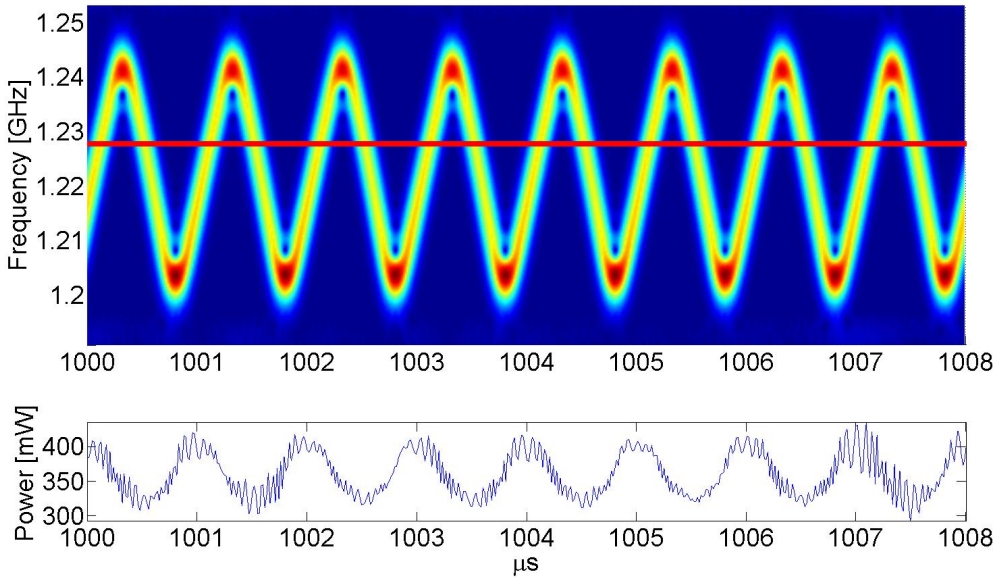

Figure 2.8: Jammer 10 power spectral density versus time (top plot), with resolution of about 3 MHz and color indicating relative power, and power versus time (bottom plot) in a 62.5-MHz band centered at the L_2 carrier frequency. The horizontal red line in the top plot indicates the GPS L_2 frequency.

their L_1 frequency modulation schemes: they placed no jamming power closer than 4.6 MHz away from the nominal L_1 carrier frequency.

Another unusual frequency modulation was encountered in a Group 3 jammer. The L_1 results for this jammer are depicted in Fig. 2.9. Again, a red line has been added at the nominal L_1 frequency. It seems to show a linear-type frequency modulation distorted by sudden frequency jumps, as seen in the upper plot of the figure. Despite its irregular nature, this waveform maintains its jamming efficacy.

All four jammers in Group 3 broadcast power at L_1, L_2, and additional frequency bands. Three of the jammers appeared to be of the same model, while a fourth was different. Jammers in this group normally use a standard chirp frequency modulation. Figure 2.9 represents the exception.

Additional types of distortion from the nominal chirp frequency modulation

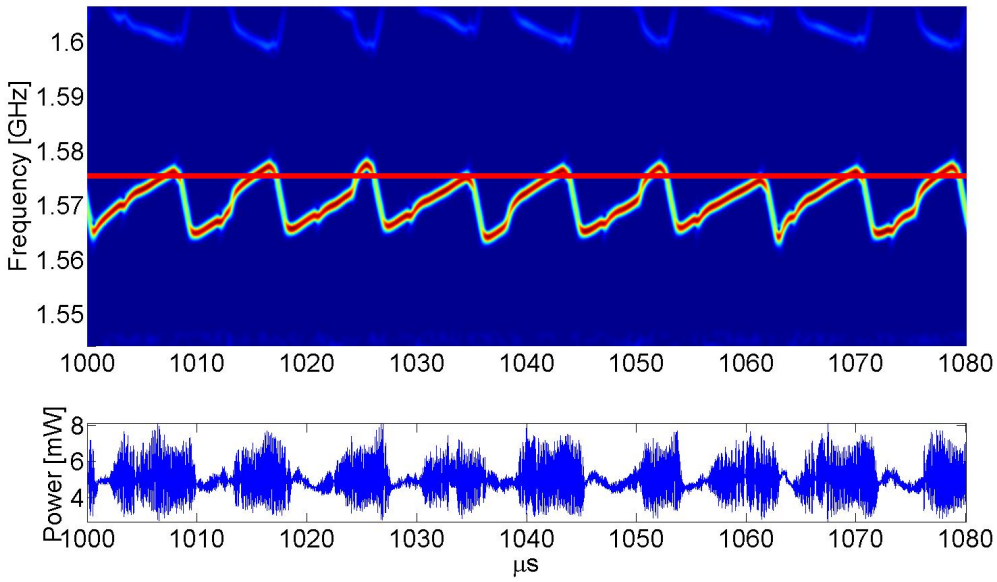

Figure 2.9: Jammer 15 power spectral density versus time, with color indicating relative power (top plot) and power versus time in a 62.5-MHz band centered at the L_1 carrier frequency (bottom plot). The horizontal red line in the top plot indicates the GPS L_1 frequency. Note the additional frequency jumps in the sweep pattern.

have been observed in some of the jammers. Discussion of each additional variation has been omitted here for the sake of brevity. More details can be found in the author's companion conference paper [35].

2.3.1 Frequency Modulation Periods and Ranges

The frequency modulation characteristics of all 18 jammers are listed in Table 2.1. The first two columns identify each jammer by group number and jammer number. The sweep period and frequency range for the L_1 sweep are shown in the third and fourth columns. The two numbers in the fourth column are the upper and lower bounds of the jamming tone sweep range in megahertz above and below the L_1 carrier frequency. For instance, the period between resets of the linear frequency modulation of Jammer 1 is 26 microseconds and the tone sweeps from 25.4 MHz below L_1 to 31.3 MHz above L_1. The fifth and sixth columns are analogous to the third and fourth columns, but for jamming in the L_2 band, with entries only for those jammers that broadcast in this band.

The sweep periods were calculated using four contiguous sweeps from near the beginning of each data set and another four sweeps 30 seconds later. The sweep periods exhibited standard deviations of less than 1 microsecond.

The reported sweep ranges are the minimum and maximum frequency observed in the same data used to calculate sweep periods. The sweep ranges changed by as much as 2.5 MHz between sweeps.

One can make a number of observations based on Table 2.1. First, as mentioned previously, jammers which appeared to be of the same model exhibited significant variations in sweep behavior. For instance, Jammers 1, 3, and 4 appeared to be of the same models, yet Jammer 1 has a sweep period nearly three times as long as Jammers 3 and 4. It also has a sweep range four times as wide. Second, some individual jammers were exceptional. For example, Jammer 10

Table 2.1: Frequency characteristics of GPS jammers

Group Number	Jammer Number	L_1 Sweep		L_2 Sweep	
		Period μs	Range (L_1+/-) MHz	Period μs	Range (L_2+/-) MHz
1	1	26	31.3 / 25.4	-	-
	2	27	31.3 / 31.3	-	-
	3	9	8.6 / 5.4	-	-
	4	9	9.6 / 4.4	-	-
2	5	9	11.6 / 7.4	-	-
	6	12	19.6 / 21.4	-	-
	7	9	7.6 / 6.4	-	-
	8	9	6.6 / 9.4	-	-
	9	9	5.6 / 8.4	-	-
	10	1	over / over	1	19.4 / 29.6
	11	9	5.6 / 6.4	9	3.4 / 7.6
	12	8	17.6 / -5.6	-	-
	13	9	18.6 / -4.6	-	-
	14	9	7.6 / 6.4	-	-
3	15	9	3.6 / 13.4	9	2.4 / 16.6
	16	8	over / over	8	16.4 / 26.6
	17	9	-5.4 / 16.4	9	-7.6 / 20.6
	18	9	10.6 / 8.4	9	0.4 / 15.6

has a sweep period nearly 10 times shorter than any other jammer, and its L_1 sweep range exceeded the 62.5 MHz bandwidth recorded by the RF sampling equipment. The sweep range of Jammer 16 also exceeded the sampled bandwidth, though its sweep period was not exceptional. Jammers 12 and 13 do not sweep through the L_1 carrier frequency, as indicated by the negative signs in the fourth column of Table 2.1. Jammer 17 suffered from the same problem, but for both L_1 and L_2.

2.3.2 In-Band Jammer Power Levels

The GPS signal is spread over several megahertz by the pseudorandom noise (PRN) codes that modulate the L_1 or L_2 carrier waves. Different GPS receivers exploit this spreading by processing more or less of the full bandwidth. The RF power of the GPS jamming signal within different bands centered at L_1 is an important concern because different receiver RF front-end bandwidths may allow different total amounts of jammer power to pass through them. For example, a C/A-code receiver with a 2-MHz RF front-end bandwidth will pass 10 dB less jammer power than will a 20-MHz bandwidth RF front end of a P(Y)-code receiver if the jammer in question spreads its power evenly over the 20-MHz band centered at the L_1 carrier frequency. If the jammer power is concentrated in a 2-MHz range, however, then both receiver front ends will pass equal total jammer power.

To determine the power in different bandwidths, the raw data were filtered to pass only the bandwidths of interest. The data were digitally filtered using a finite input response (FIR) equiripple band-pass filter, providing 60 dB of attenuation at 2 MHz past the roll-off frequency. Note that a real GPS receiver may not have analog filter frequency roll offs as sharp as those used in this work.

Table 2.2 presents the results of this study. It reports power measurements

Table 2.2: Jammer power levels in frequency bands of interest.

Group Number	Jammer Number	L_1 Bandwidth, MHz			L_2 Bandwidth, MHz			Other Bands
		2	20	50	2	20	50	
		Power in band, mW			Power in band, mW			Yes/No
1	1	1.7	9.5	22	-	-	-	No
	2	0.1	0.7	1.8	-	-	-	No
	3	5.8	20	20	-	-	-	No
	4	7.0	23	23	-	-	-	No
2	5	15	58	58	-	-	-	No
	6	6.3	40	77	-	-	-	Yes
	7	150	520	520	-	-	-	Yes
	8	87	334	334	-	-	-	Yes
	9	159	499	499	-	-	-	Yes
	10	1.2	6.5	19	27	146	351	No
	11	244	642	642	221	482	482	No
	12	0.00	58	109	-	-	-	No
	13	0.00	43	107	-	-	-	No
	14	18	42	42	-	-	-	Yes
3	15	1.18	4.76	4.95	0.60	5.44	7.70	Yes
	16	0.01	0.04	0.07	0.04	0.20	0.26	Yes
	17	0.00	1.46	3.44	0.00	0.37	7.74	Yes
	18	1.39	4.61	4.69	0.61	4.66	5.64	Yes

averaged over 15 milliseconds in three different bandwidths: 2, 20, and 50 MHz, all centered at the nominal L_1 or L_2 carrier frequency. The table also indicates whether each jammer broadcasts power at frequencies other than the GPS frequencies. No power data is given for the non-GPS frequencies because they are not the focus of this work.

A number of observations can be drawn from Table 2.2. First, there is a large variation in broadcast power among jammers, with Group 2 jammers being on average more powerful. Specifically, Jammer 11 is the most powerful, broadcasting more than a watt in the GPS bands! Second, jammers of the same model broadcast roughly the same amount of power despite the differences in sweep behavior mentioned above. For instance, Jammers 1, 3, and 4 broadcast roughly

the same amount of power, and Jammers 15, 17, and 18 do so as well. Third, the poor frequency plans of Jammers 12, 13, and 17 are apparent in the power measurements. According to Table 2.1, these jammers did not sweep a tone through L_1 or L_2, and effectively no power was measured in the 2-MHz band centered on the L_1 or L_2 carrier frequencies.

Although not shown in the tables, Jammers 12, 13, and 14 exhibited periodic variations in broadcast power. Their peak-to-peak power varies as a chirp with period approximately 15 milliseconds and amplitude on the order of 10 percent of the total broadcast power.

The measured power values in Table 2.2 for jammers of Groups 1 and 2 were derived using direct cable connections. Thus, they report an approximation of the total power into the transmitting antenna. The power received at a GPS receiver's RF front end will be affected by any antenna inefficiency, the antenna gain pattern, and the space loss, among other effects.

In contrast, the power reported for Group 3 jammers includes all of those effects for the given test configuration. Specifically, the receiving antenna picked up only a fraction of the radiated power because the receiving antenna subtended only a fraction of the 4π steradians around the transmitting antenna. Also, the power that was received was boosted by the receiving antenna's active low-noise amplifier. Finally, the radiation environment inside the RF enclosure is uncertain, and the enclosure constrains the separation of the antennas to be on the order of one wavelength, thereby giving rise to near-field effects. Therefore, the indicated power levels for the Group 3 jammers do not constitute measures of absolute power. The tabulated power levels for Group 3 jammers are included primarily for purposes of comparison within the group.

2.4 Maximum Effective Range Test

The goal of the second set of tests was to determine the effective ranges of the GPS jammers when interfering with a COTS receiver. This test was performed before the Department of Homeland Security provided access to White Sands Missile Range. A constraint on this test was that it could not broadcast harmful radiation to the environment. Ideally, the jammers and a receiver would be taken outside and tested with all antennas attached. However, this type of test would possibly interfere with other equipment and is illegal in the United States, unless you have government permission. A close approximation to this scenario can be constructed using a high-fidelity simulated GPS signal, a commercial GPS receiver, a GPS jammer in an RF enclosure, and a set of attenuators to simulate various distances. The conceptual setup for the second test is shown in the block diagram of Fig. 2.10. The physical equipment used in the test is shown in Fig. 2.11.

Each range test involved running a GPS jammer inside the RF enclosure, passing its signal through the enclosure's coaxial feed-through, and electrically combining that signal with a GPS simulator signal. The combined signal was then input to the antenna connector of the COTS GPS receiver. Attenuators were inserted in-line with the GPS jammer before it arrived at the combiner. Using this setup, two sub-tests were conducted. The first sub-test determined the jamming signal attenuation level necessary for continuous tacking. The second sub-test determined the attenuation level necessary to allow the receiver to acquire the simulator signal within five minutes from a cold start. As will be shown in the next section, the resulting attenuation values can be converted into effective ranges of the jammers if one makes certain reasonable assumptions about transmitting and receiving antenna gains and path losses.

The simulator power level was set so that the power into the receiver

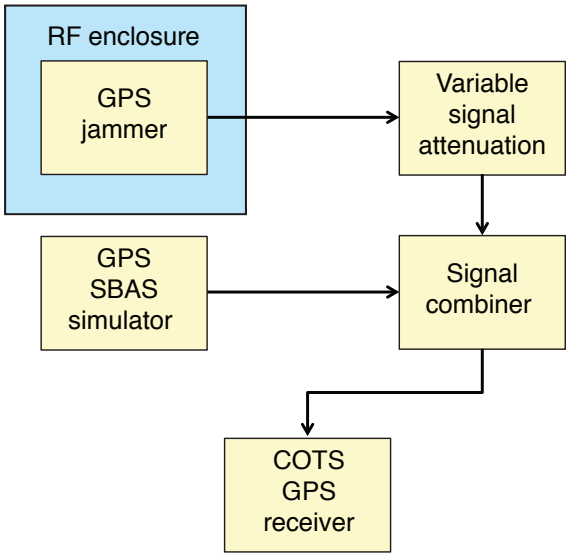

Figure 2.10: Block diagram of the test procedure and equipment used to determine the GPS jammers' effective ranges.

Figure 2.11: The physical equipment used to determine the GPS jammers' effective ranges.

matched that which it would receive from the actual GPS constellation through a typical roof-mounted passive patch antenna. This power level was checked by comparing the resulting carrier-to-noise density ratio $\frac{C}{N_0}$ for all of the visible satellites when using the simulator against typical $\frac{C}{N_0}$ values when using the roof-mounted antenna. Typical levels reported by the receiver were $\frac{C}{N_0}$ = 43 dB-Hz.

2.5 Maximum Effective Range Test Results

The jamming signal attenuation levels resulting from the two sub-tests are presented in Table 2.3. These tests were conducted on one jammer from Group 1 and three jammers from Group 2. No jammers from Group 3 were included because of the broadcast power uncertainties discussed in connection with Table 2.2.

Table 2.3: Jammer attenuation levels needed to allow COTS GPS receiver acquisition and tracking.

Group Number	Jammer Number	Tracking dB	Acquisition dB
1	1	82	92
2	10	82	88
	11	108	111
	13	77	89

The attenuation values by themselves are not very useful, but they can be converted into distance measurements with a number of assumptions. The ratio of received power to transmitted power can be expressed as:

$$\frac{P_r}{P_t} = G_t G_r \left(\frac{\lambda}{4\pi r}\right)^2 \tag{2.1}$$

where G_t is the transmitting antenna gain, G_r is the receiving antenna gain, and the term $\left(\frac{\lambda}{4\pi r}\right)^2$ is the path loss for radiation of wavelength λ over the dis-

tance r. This equation can be solved for the range, r:

$$r = \left(\frac{\lambda}{4\pi}\right)\sqrt{G_{\mathrm{t}}G_{\mathrm{r}}\frac{P_{\mathrm{t}}}{P_{\mathrm{r}}}} \tag{2.2}$$

The quantity in this formula that equates to the total electrical jammer attenuation produced in each bench-top test is the product of the antenna gains and the ratio of transmitted to received power: $G_{\mathrm{t}}G_{\mathrm{r}}\frac{P_{\mathrm{t}}}{P_{\mathrm{r}}}$.

To convert the results in Table 2.3 into effective ranges, the transmitting and receiving antennas can be assumed to be perfect, lossless, isotropic radiators. In this case, the gain terms, G_{t} and G_{r}, are unity. Each measured attenuation value can be converted to the unitless ratio, $\frac{P_{\mathrm{t}}}{P_{\mathrm{r}}}$, and substituted into the equation for r. Use of this equation at the L_1 carrier frequency yields the ranges in Table 2.4. If the range between the jammer and receiver is less than that listed in the third column of the table, then the jammer will prevent the receiver from tracking and acquiring. If the range is less than that listed in the last column but more than that listed in the third column, the receiver will continue to track but be unable to acquire. The effective ranges are at least an order of magnitude greater than the claims of the jammers' purveyors.

Table 2.4: Ranges of jammer effectiveness against COTS GPS receiver when using lossless isotropic antennas.

Group Number	Jammer Number	Tracking m	Acquisition m
1	1	308	973
2	10	308	614
	11	6140	8670
	13	173	689

Distinct scenarios with different antennas can be approximately tested using Table 2.3 and the range equation. For example, a patch antenna that is oriented perfectly skyward might have 10 dB of attenuation at very low elevation angles,

and the jammer might have an additional 3 dB loss due to polarization mismatch. In this scenario, the effective jamming range would be factored down by $10^{-13/20} = 0.22$. In this case, Jammer 11's tracking interference range would be reduced from 6.1 kilometers to 1.4 kilometers. Additional jammer signal attenuation might occur if the emissions passed through the reduced RF aperture of a vehicle's body and windows [3]. Such an effect could be incorporated into the range equation to determine a revised effective range.

Due to the ignored losses in the real system, it would likely be safe to assume that the effective ranges of the GPS jammers would be no greater than those listed in Table 2.4. The ranges could potentially be greater if a high-gain receiving antenna were aimed directly at the jamming source, or if the jamming source used a high-gain transmitting antenna aimed at the receiver. None of the jammers tested employed such an antenna.

2.6 Summary of the Jammer Signal Characteristics

This chapter presented the signal properties of 18 commercially available GPS jammers as determined from two types of live experimental tests. The first test examined the frequency structures and power levels of the jammer signals. It showed that all of the jammers used some sort of swept tone method to generate broadband interference. The majority of the jammers used linear chirp signals, all jammed L_1, only six jammed L_2, and none jammed L_5. The sweep period of the jammers is about 9 microseconds on average, and they tend to sweep a range of less than 20 MHz. Some of the jammers' sweep ranges failed to encompass the target L_1 or L_2 carrier frequencies. The second test provided an estimate of four of the jammers' effective ranges when deployed against a typical commercial receiver. An upper bound on the effective ranges was calculated

for idealized, lossless, isotropic radiating and receiving antennas with matched polarizations. The weakest of the four jammers affected tracking at a range of about 300 meters and acquisition at about 600 meters, while the strongest affected tracking at a range of about 6 kilometers and acquisition at about 8.5 kilometers.

2.7 Data Collection Campaign at White Sands Missile Range

The aforementioned laboratory-collected data are useful for many different types of algorithm verification. However, field tests include other effects that are typically not present in laboratory tests, such as multi-path. Additionally, some algorithms can only be truly verified on several sets of real data collected in a field campaign. The signal localization algorithm discussed in Chapter 7 is one such algorithm. Therefore, data were collected in the field and a summary of the data collection campaign is presented here only briefly, but more information can be found in [37].

The field scenario took place at a DHS-sponsored nighttime test at White Sands Missile Range (WSMR), which is located in New Mexico. Four different stations were deployed at locations shown in Fig 2.12, where the top and bottom stations were separated by approximately one kilometer and the left and right stations were separated by approximately half of that amount. PPDs were driven along the road that travels from the station at the top of the photo to the one at the bottom of the photo. A typical recording station is displayed in Fig 2.13. Each station had two antennas; one aimed at the road and meant for receiving the PPD signal and the other shielded and aimed away from the road and meant for receiving GPS signals with minimal PPD interference. The data were recorded at approximately 9 MHz with a mixing frequency set at GPS

L_1. Complex sampling was used. The data were recorded using a linked pair of Ettus^{TM} Universal Software Radio Peripheral (USRP) receivers running on a common clock; one USRP for each antenna. The equipment was powered by a car with a cigarette-lighter power inverter placed at each station. The true positions of the jammers were known based on data recorded by an accurate inertial measurement unit (IMU) placed in the vehicles with the PPDs.

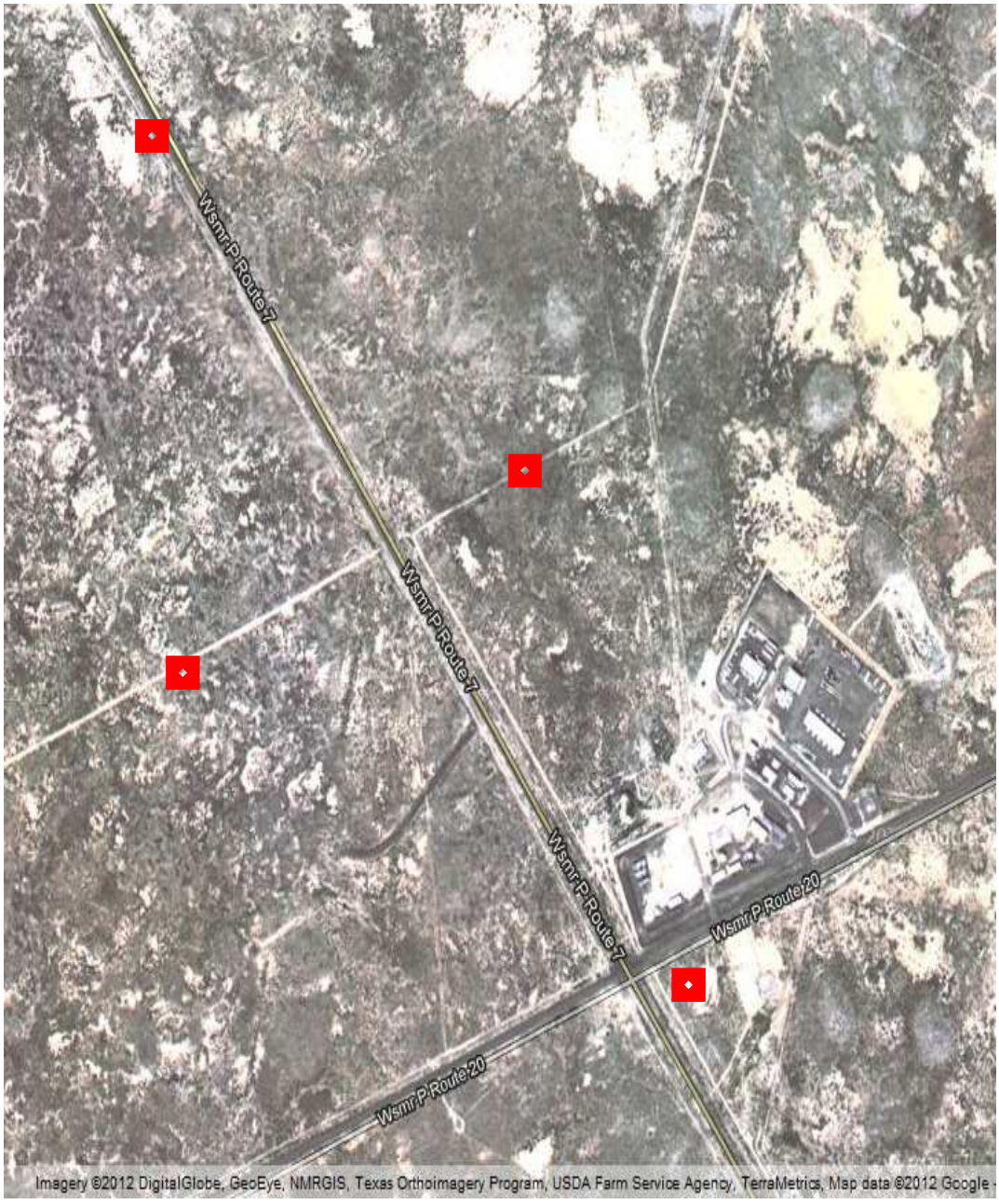

Figure 2.12: A Google Maps™ image of WSMR that has red squares added to denote the locations of the deployed receiver stations. (Imagery ©2012 DigitalGlobe, GeoEye, NMRGIS, Texas Orthoimagery Program, USDA Farm Service Agency, Map data ©2012 Google)

Figure 2.13: An image of a typical receiver station setup at WSMR.

CHAPTER 3

SIGNAL MODEL

3.1 Signal Model Considerations

The previous chapter and a paper by the author that surveyed 18 different PPDs provided by the DHS found that all of the jammers used some form of chirp-style signals [35]. Therefore, this chaper's modeling focus will be restricted to chirp-style signals.

The PPDs have inconsistent signal properties, which vary from model to model and even from device to device of the same model for the PPDs examined in [35]. For example, the chirp periods were in the range of 1–27 μs, with frequency spans in the range of 12–62.5 MHz, and the starting frequencies of the chirps varied by more than 36 MHz. An important consequence of this PPD signal variability is the requirement of a separate set of model parameters for every PPD.

Time-histories of the frequency power spectra and total received power of a common PPD signal are shown in Fig. 2.7. The chirp period is approximately 10 μs, and the power level is consistently near 20 mW. The signal's frequency can be modeled with both a first-order polynomial ramp-up and ramp-down. This simple chirp model will be referred to as a first-order chirp.

The frequency power spectra and total received power time-histories of an uncommon PPD signal are shown for Jammer 1 in Fig. 3.1. The first-order chirp model is a poor match for this PPD. Approximately 25% of the jammers from [35] cannot be modeled accurately by a first-order chirp. A more complicated model will be required to handle this type of signal behavior.

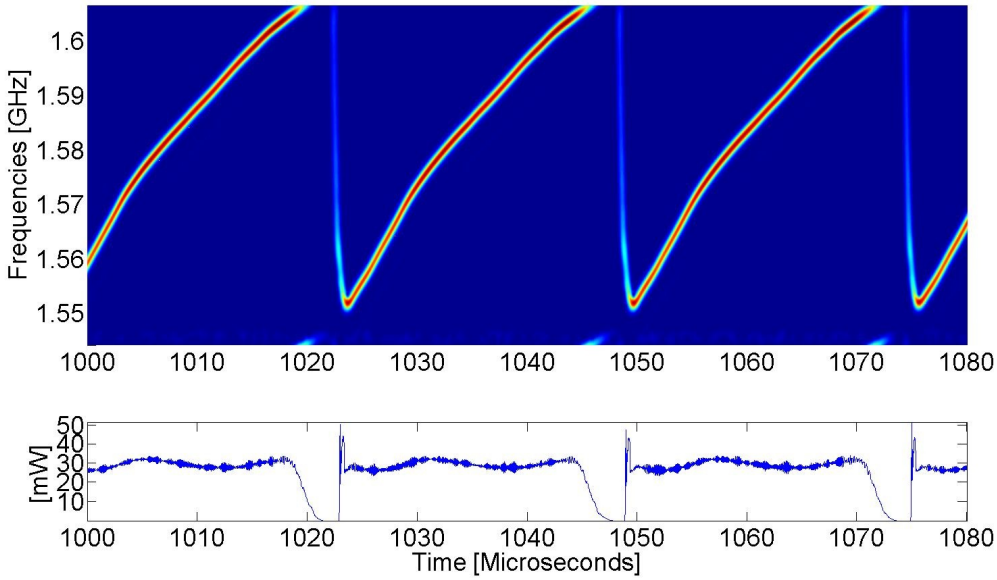

Figure 3.1: An atypical PPD's FFT power spectrum time-history (top plot), and total received signal power (bottom plot). The ramp up is not well modeled as a first-order chirp.

3.2 Jammer Polynomial Signal Model

There are many ways that the signals in Figs. 2.7 and 3.1 can be modeled. This chapter takes a state-space approach that is very similar to that in [38]. Other models exist that can capture part of the behavior of each PPD signal [40], but this chapter's model captures the PPDs' behavior at least as accurately as [40] for a fraction of the signal period, and it permits more accurate modeling in the remainder of the signal period.

The spectrum time-history in Fig. 2.7 has two distinct stages. The first stage is characterized by a positive rate of change of the frequency, the ramp upwards in the plot, which occupies the majority of the chirp period. The second epoch has a negative rate of change of the frequency, the ramp downwards in the plot, which occupies very little of the chirp period. The model developed in this chapter uses two frequency ramps to continuously describe the frequency and

phase of the signal over a single chirp period.

The model starts with an initial phase and frequency and then propagates them forward in time using a set of polynomials, one for the ramp-up and one for the ramp-down. Basis functions that are not polynomials could also be used to describe the model's frequency behavior over time, but they are not considered in this work because the polynomial model is easy to work with and provides sufficient fidelity for this dissertation's developments. A graphical representation of an example frequency time-history for this model is shown in Fig. 3.2.

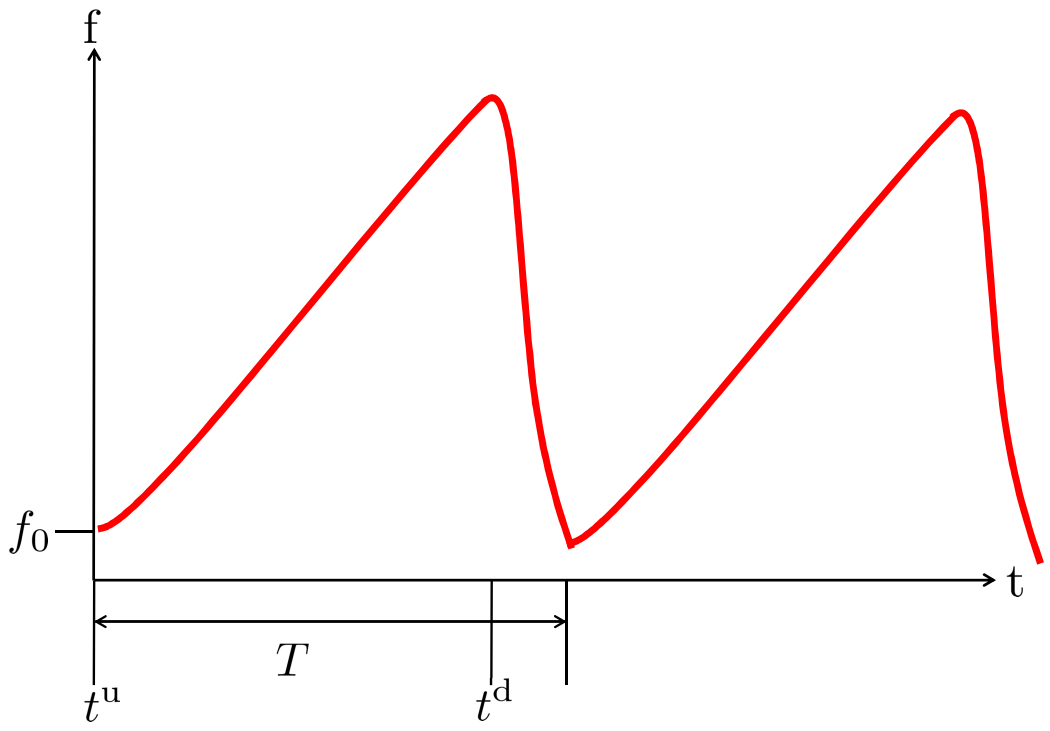

Figure 3.2: One possible frequency time-history for a frequency-polynomial model of a chirp style jammer.

The state vector, $\mathbf{x}$, for the polynomial chirp signal model is defined as:

$$\mathbf{x} = \begin{bmatrix} \theta_0 \\ f_0 \\ \mathbf{c}^{\mathrm{u}} \\ \mathbf{c}^{\mathrm{d}} \\ A \\ t^{\mathrm{u}} \\ t^{\mathrm{d}} \\ T \end{bmatrix} = \begin{bmatrix} \theta_0 \\ f_0 \\ \begin{bmatrix} c_1^{\mathrm{u}} \\ \vdots \\ c_{\mathrm{M_u}}^{\mathrm{u}} \end{bmatrix} \\ \begin{bmatrix} c_1^{\mathrm{d}} \\ \vdots \\ c_{\mathrm{M_d}}^{\mathrm{d}} \end{bmatrix} \\ A \\ t^{\mathrm{u}} \\ t^{\mathrm{d}} \\ T \end{bmatrix} \tag{3.1}$$

where θ_0 is the phase of the signal polynomial at an epoch time in units of cycles, f_0 is the frequency of the signal polynomial at the same epoch time in units of Hz, the vectors $\mathbf{c}^{\mathrm{u}}$ and $\mathbf{c}^{\mathrm{d}}$ contain the coefficients of the ramp-up and ramp-down frequency polynomials with various units, A is the received signal amplitude in units of volts, t^{u} is the ramp-up polynomial start time for the current chirp period in units of seconds, t^{d} is the ramp-down polynomial start time for the same period in units of seconds, and T is the chirp period in units of seconds.

This model is a hybrid system or switching mode model, but the full hybrid system formalism is not necessary for this dissertation's developments. The model uses two different modes of behavior. The first mode is for the ramp-up, and the second is for the ramp-down. Additional frequency ramps could be added to handle more complicated behavior. The mode of operation at any given time can be determined using only the two timing states t^{u} and t^{d}. If t^{u} is less than t^{d} then the mode of operation is a frequency ramp-up, which is called

Mode A. If t^{d} is less than t^{u} then the mode of operation is a frequency ramp-down, which is called Mode B. Once the system time passes the latter of the two timing states, t^{u} or t^{d}, the earlier time is incremented by the chirp period T, which will force a change in the mode of operation.

For example, if $t^{\mathrm{u}} = 0$, $t^{\mathrm{d}} = 1$, $T = 2$, and the system time $t = 0.5$, then the mode of operation would begin in the ramp-up mode, Mode A, but would then switch to ramp down Mode B when t reached 1, and the new value of t^{u} would become 2. To be explicit, the system mode is determined by the following equations:

$$\text{Mode} = \begin{cases} \text{A if } t^{\mathrm{u}} \leq t^{\mathrm{d}} \\ \text{B if } t^{\mathrm{d}} < t^{\mathrm{u}} \end{cases} \tag{3.2}$$

The frequency is modeled as polynomial in time-frequency space:

$$f(\mathbf{x}, t) = \begin{cases} f_0 + \sum_{j=1}^{\mathrm{M_u}} c_j^{\mathrm{u}} \left(t - t^{\mathrm{u}}\right)^j, \text{ if in Mode A} \\ f_0 + \sum_{j=1}^{\mathrm{M_d}} c_j^{\mathrm{d}} \left(t - t^{\mathrm{d}}\right)^j, \text{ if in Mode B} \end{cases} \tag{3.3}$$

where c_j^{u} and c_j^{d} are the frequency polynomial coefficients from the vectors $\mathbf{c}^{\mathrm{u}}$ and $\mathbf{c}^{\mathrm{d}}$, $\mathrm{M_u}$ is the number of coefficients for the frequency ramp-up, and $\mathrm{M_d}$ is the number of coefficients for the frequency ramp-down.

The phase is defined as the integral of the frequency polynomial:

$$\theta(\mathbf{x}, t) = \begin{cases} \theta_0 + f_0 \left(t - t^{\mathrm{u}}\right) + \sum_{j=1}^{\mathrm{M_u}} c_j^{\mathrm{u}} \frac{\left(t - t^{\mathrm{u}}\right)^{(j+1)}}{(j+1)}, \text{ if in Mode A} \\ \theta_0 + f_0 \left(t - t^{\mathrm{d}}\right) + \sum_{j=1}^{\mathrm{M_d}} c_j^{\mathrm{d}} \frac{\left(t - t^{\mathrm{d}}\right)^{(j+1)}}{(j+1)}, \text{ if in Mode B} \end{cases} \tag{3.4}$$

When in ramp-up Mode A, θ_0 and f_0 in the state vector of Eq. (3.1) apply at epoch time t^{u}. Conversely, when in ramp-down Mode B, θ_0 and f_0 in the state vector of Eq. (3.1) apply at epoch time t^{d}. For continuities sake, the initial

polynomial frequency, f_0, and phase, θ_0, are redefined after each mode switch, i.e. the final frequency and phase of the polynomial in one mode is the starting frequency and phase of the polynomial in the next mode.

The number of coefficients, M_u and M_d, determines the order of the frequency polynomial and is a user-defined tuning parameter. Higher-order polynomials are able to emulate the behavior of more complicated jammers, but the trade-off is a greater computational effort and a greater likelihood of numerical instability. A fifth-order polynomial appears to provide a good approximation to even the most complicated PPD surveyed in [35].

3.3 Jammer Polynomial Signal Model State-Space Dynamics

The dynamics of the jammer polynomial signal model can be cast into state-space form as follows:

$$\mathbf{x}_{k+1} = \mathbf{\Phi}\left(t_{k+1}, t_k; \mathbf{x}_k\right) \mathbf{x}_k + \mathbf{\Gamma}\left(t_{k+1}, t_k; \mathbf{x}_k\right) \mathbf{v}_k \tag{3.5}$$

where $\mathbf{x}_{k+1}$ is the state vector at time t_{k+1}, $\mathbf{x}_k$ is the state vector at time t_k, and $\mathbf{v}_k$ is the process noise vector that applies during the transition from t_k to t_{k+1}. The matrix $\mathbf{\Phi}\left(t_{k+1}, t_k; \mathbf{x}_k\right)$ is the state transition matrix (STM) and $\mathbf{\Gamma}\left(t_{k+1}, t_k; \mathbf{x}_k\right)$ is the process noise influence matrix. Note that this dynamic model is potentially nonlinear due to the possible dependence of $\mathbf{\Phi}\left(t_{k+1}, t_k; \mathbf{x}_k\right)$ and $\mathbf{\Gamma}\left(t_{k+1}, t_k; \mathbf{x}_k\right)$ on the state $\mathbf{x}$. Their state dependencies result solely from the timing states t^{u} and t^{d} and the system time t. If it were desired to model only one ramp, then the dynamic model would be linear, i.e., it would stay in only one mode. The matrix $\mathbf{\Phi}\left(t_{k+1}, t_k; \mathbf{x}_k\right)$ is defined as:

$$\mathbf{\Phi}\left(t_{k+1}, t_k; \mathbf{x}_k\right) = \prod_{l=1}^{L} \mathbf{\Phi}'_l\left(t_{l+1}^{\text{change}}, t_l^{\text{change}}; \mathbf{x}_{k,l}\right) \tag{3.6}$$

where $\mathbf{\Phi}'_l\left(t_{l+1}^{\text{change}}, t_l^{\text{change}}; \mathbf{x}_{k,l}\right)$ is a STM from time t_l^{change} to time t_{l+1}^{change}, the time t_l^{change} is either t_k, a t^{d}, or a t^{u}, the time t_{l+1}^{change} is either a t^{d}, a t^{u}, or t_{k+1}, L is one plus the number of mode transitions (number up plus number down) past which t must be propagated, and $\mathbf{x}_{k,l}$ is the state in the limit as t approaches t_l^{change} from below. This STM corresponds to the sequence of partial propagation steps:

$$\mathbf{x}_{k,l+1} = \mathbf{\Phi}'_l\left(t_{l+1}^{\text{change}}, t_l^{\text{change}}; \mathbf{x}_{k,l}\right)\mathbf{x}_{k,l} \tag{3.7}$$

for $l = 1, ..., L$. The propagation starts with $l = 1$, $t_l^{\text{change}} = t_k$, and $\mathbf{x}_{k,l} = \mathbf{x}_k$. The propagation ends with $l = L$, $t_{L+1}^{\text{change}} = t_{k+1}$, and thus $\mathbf{x}_{k+1} = \mathbf{\Phi}'_L\left(t_{L+1}^{\text{change}}, t_L^{\text{change}}; \mathbf{x}_{k,L}\right)\mathbf{x}_{k,L}$. The type of STM $\mathbf{\Phi}'_l\left(t_{l+1}^{\text{change}}, t_l^{\text{change}}; \mathbf{x}_{k,l}\right)$ is determined by the three possible cases of t_{l+1}^{change}:

$$\text{Case 1: } t_{l+1}^{\text{change}} = t_{k,l}^{\text{d}} \tag{3.8}$$

$$\text{Case 2: } t_{l+1}^{\text{change}} = t_{k,l}^{\text{u}} \tag{3.9}$$

$$\text{Case 3: } t_{l+1}^{\text{change}} = t_{k+1} \tag{3.10}$$

where $t_{k,l}^{\text{u}}$ and $t_{k,l}^{\text{d}}$ are the corresponding mode transition states from $\mathbf{x}_{k,l}$ and where:

$$t_{l+1}^{\text{change}} = \min\left(\max\left(t_{k,l}^{\text{u}}, t_{k,l}^{\text{d}}\right), t_{k+1}\right) \tag{3.11}$$

The STM can take one of the following three forms:

$$\mathbf{\Phi}'_l\left(t_{l+1}^{\text{change}}, t_l^{\text{change}}; \mathbf{x}_{k,l}\right) = \begin{cases} \mathbf{\Phi}_{\text{up}}\left(t_{k,l}^{\text{d}} - t_{k,l}^{\text{u}}\right), & \text{if Case 1} \\ \mathbf{\Phi}_{\text{down}}\left(t_{k,l}^{\text{u}} - t_{k,l}^{\text{d}}\right), & \text{if Case 2} \\ \mathbf{I}, & \text{if Case 3} \end{cases} \tag{3.12}$$

where the matrices $\mathbf{\Phi}_{\text{up}}$ and $\mathbf{\Phi}_{\text{down}}$ are only functions of the states t^{d} and t^{u} defined at time t_l^{change}. Most of their rows equal rows of the corresponding identity matrix. The only exceptions are the first and second rows, i.e. those corresponding to θ_0 and f_0, and the third-to-last or second-to-last row, i.e. the t^{u} row or the

t^{d} row. The matrix $\mathbf{\Phi}_{\mathrm{up}}$ propagates the phase in the first row and the frequency in the second row using Mode A of, respectively, Eqs. (3.4) and (3.3). Its third to last row updates t^{u} to become $t^{\mathrm{u}} + T$. The matrix $\mathbf{\Phi}_{\mathrm{down}}$ acts similarly, except it uses Mode B in Eqs. (3.4) and (3.3) to define its first two rows, and its second-to-last row updates t^{d} to $t^{\mathrm{d}} + T$. The term $\mathbf{I}$ is the identity matrix, and it does not modify the state, $\mathbf{x}$ in any way. A $\mathbf{\Phi}$ of $\mathbf{I}$ occurs when there is no mode transition, as is in Case 3 of Eq. (3.10).

The following is an example of how the dynamics would create the STM to propagate a state, $\mathbf{x}_k$, from time t_k that is before t^{u} to time t_{k+1} that is after t^{u}, but with no other mode change times between t_k and t_{k+1}; this example has a single mode transition:

$$\begin{aligned}
\mathbf{\Phi}\left(t_{k+1}, t_k; \mathbf{x}_k\right) &= \prod_{l=1}^{2} \mathbf{\Phi}'_l\left(t_{l+1}^{\text{change}}, t_l^{\text{change}}; \mathbf{x}_{k,l}\right) \\
&= \mathbf{\Phi}'_2\left(t_3^{\text{change}}, t_2^{\text{change}}; \mathbf{x}_{k,2}\right) \mathbf{\Phi}'_1\left(t_2^{\text{change}}, t_1^{\text{change}}; \mathbf{x}_{k,1}\right) \\
&= \mathbf{\Phi}'_2\left(t_{k+1}, t_{k,1}^{\mathrm{u}}; \mathbf{x}_{k,2}\right) \mathbf{\Phi}'_1\left(t_{k,1}^{\mathrm{u}}, t_k; \mathbf{x}_{k,1}\right) \\
&= \mathrm{I}\, \mathbf{\Phi}_{\mathrm{down}}\left(t_{k,1}^{\mathrm{u}} - t_{k,1}^{\mathrm{d}}\right) \\
&= \mathbf{\Phi}_{\mathrm{down}}\left(t_{k,1}^{\mathrm{u}} - t_{k,1}^{\mathrm{d}}\right)
\end{aligned} \tag{3.13}$$

where the final STM in this example is simply the matrix $\mathbf{\Phi}_{\mathrm{down}}\left(t_{k,1}^{\mathrm{u}} - t_{k,1}^{\mathrm{d}}\right)$. The matrix $\mathbf{\Phi}_{\mathrm{down}}\left(t_{k,1}^{\mathrm{u}} - t_{k,1}^{\mathrm{d}}\right)$ will propagate the frequency and phase according to Mode B in the polynomials in Eqs. (3.3) and (3.4) with the argument of t^{u} for t. It will not increment t^{u}, but it will increment t^{d} by T. The state $\mathbf{x}_{k,1}$ starts as the initial state $\mathbf{x}_k$, then Eq. (3.11) is evaluated for t_2^{change} which is found to be $t_{k,1}^{\mathrm{u}}$, then the state is propagated to time $t_2^{\text{change}} = t_{k,1}^{\mathrm{u}}$, at which point it is defined as $\mathbf{x}_{k,2}$, where $\mathbf{x}_{k,2} = \mathbf{\Phi}_{\mathrm{down}}\left(t_{k,1}^{\mathrm{u}} - t_{k,1}^{\mathrm{d}}\right)\mathbf{x}_{k,1}$. Equation (3.11) is then evaluated using state $\mathbf{x}_{k,2}$, and it is determined that $t_3^{\text{change}} = t_{k+1}$, so the STM $\mathbf{\Phi}'_2\left(t_{k+1}, t_{k,1}^{\mathrm{u}}; \mathbf{x}_{k,2}\right) = \mathrm{I}$. The complete STM that propagates the state from t_k to t_{k+1} is the final line in Eq. (3.13). A similar procedure would be used to handle the other mode change

and propagate a state from a time before t^{d} to a time after t^{d}. If the time t_{k+1} were several periods later than t_k, then the series would contain multiple mode change matrices.

The process noise influence matrix is defined using the following discrete-time recursion from linear systems theory, where the arguments and k dependence have been dropped for the moment:

$$\mathbf{\Gamma}_{l+1} = \mathbf{\Phi}'_l \mathbf{\Gamma}_l + \mathbf{\Gamma}'_l \tag{3.14}$$

where $\mathbf{\Phi}'_l$ is the STM and $\mathbf{\Gamma}'_l$ is the process noise influence matrix components due to the current time interval of the recursion, t_l^{change} to t_{l+1}^{change}. $\mathbf{\Gamma}_l$ is the component from the last recursion iteration and is specifically defined for $l = 1$ as $\mathbf{\Gamma}_1 = 0$. Equation (3.14) is evaluated the same number of times as there are product terms in Eq. (3.6), L times, and the final $\mathbf{\Gamma}_{l+1}$ matrix is defined as $\mathbf{\Gamma}(t_{k+1}, t_k; \mathbf{x}_k)$ from Eq. (3.5). The matrix $\mathbf{\Gamma}'_l$ is defined as:

$$\begin{aligned} \mathbf{\Gamma}'_l &= \mathbf{\Gamma}'_l\left(t_{l+1}^{\text{change}}, t_l^{\text{change}}; \mathbf{x}_{k,l}\right) \\ &= \begin{cases} \mathbf{\Gamma}_{\text{up}}, & \text{if Case 1} \\ \mathbf{\Gamma}_{\text{down}}, & \text{if Case 2} \\ 0, & \text{if Case 3} \end{cases} \end{aligned} \tag{3.15}$$

where the matrices $\mathbf{\Gamma}_{\text{up}}$ and $\mathbf{\Gamma}_{\text{down}}$ permit the introduction of process noise effects at the mode change times, $t_{k,l}^{\mathrm{d}}$ and $t_{k,l}^{\mathrm{u}}$ respectively, for the upcoming set of polynomials, and they are primarily user-selected. The matrices $\mathbf{\Gamma}_{\text{up}}$ and $\mathbf{\Gamma}_{\text{down}}$ have all zeros except for a single 1 in each column, and no row has more than a single 1. The matrix $\mathbf{\Gamma}_{\text{up}}$ has entries of 1 in rows corresponding to the following states: f_0, $\mathbf{c}^{\mathrm{d}}$, A, t^{u}, and T. The matrix $\mathbf{\Gamma}_{\text{down}}$ is effectively reversed with respect to the polynomial direction and is assumed to have only entries of 1 in the rows corresponding to states: f_0, $\mathbf{c}^{\mathrm{u}}$, A, t^{d}, and T. The total number of columns in $\mathbf{\Gamma}_{\text{up}}$

and $\mathbf{\Gamma}_{\text{down}}$ is $M_u + M_d + 5$. This equals the number of elements in $\mathbf{v}_k$. Process noise is not permitted to enter directly into the phase state, but noise can enter through the other state elements.

For ease of analysis the matrices $\mathbf{\Gamma}_{\text{up}}$ and $\mathbf{\Gamma}_{\text{down}}$ are assumed to be diagonal and have only entires of 1 or 0 along the diagonal. The matrix $\mathbf{\Gamma}_{\text{up}}$ is assumed to have entries of 1 on the following states: f_0, $\mathbf{c}^{\text{d}}$, A, t^{u}, and T. The matrix $\mathbf{\Gamma}_{\text{down}}$ is effectively reversed with respect to the polynomial direction and is assumed to have entries of 1 on the following states: f_0, $\mathbf{c}^{\text{u}}$, A, t^{d}, and T. Process noise is not permitted to enter directly into the phase state, but noise can enter through the other state elements.

The following is an example of how the dynamics would create the process noise influence matrix, $\mathbf{\Gamma}(t_{k+1}, t_k; \mathbf{x}_k)$, for the state $\mathbf{x}_k$ for the same scenario as the propagation of the state in the STM example of Eq. (3.13). The arguments and dependencies are again dropped for the moment, but can be determined by looking at Eqs. (3.13) and (3.15). The first iteration of the recursion is:

$$\begin{aligned}\mathbf{\Gamma}_2 &= \mathbf{\Phi}_1'\mathbf{\Gamma}_1 + \mathbf{\Gamma}_1' \\ &= \mathbf{\Phi}_1' 0 + \mathbf{\Gamma}_{\text{down}} \\ &= \mathbf{\Gamma}_{\text{down}}\end{aligned} \tag{3.16}$$

where Eq. (3.11) has been evaluated using $\mathbf{x}_{k,1}$ to determine $t_2^{\text{change}} = t_{k,1}^{\text{u}}$, which selects Case 2 for Eq. (3.15), and thus causes $\mathbf{\Gamma}_1'$ to equal $\mathbf{\Gamma}_{\text{down}}$. $\mathbf{\Gamma}_1$ has been initialized as the zero matrix. The matrix at the end of the iteration is $\mathbf{\Gamma}_2\left(t_2^{\text{change}}, t_1^{\text{change}}; \mathbf{x}_{k,1}\right) = \mathbf{\Gamma}_{\text{down}}$, and will be used in the next iteration:

$$\begin{aligned}\mathbf{\Gamma}_3 &= \mathbf{\Phi}_2'\mathbf{\Gamma}_2 + \mathbf{\Gamma}_2' \\ &= \mathbf{I}\,\mathbf{\Gamma}_{\text{down}} + 0 \\ &= \mathbf{\Gamma}_{\text{down}}\end{aligned} \tag{3.17}$$

where Eq. (3.11) has been evaluated again, but at $\mathbf{x}_{k,2}$, and it is determined that $t_3^{\text{change}} = t_{k+1}$, which finds that the case for Eq. (3.15) is Case 3, and thus determines $\mathbf{\Gamma}_2' = 0$. The final process noise influence matrix $\mathbf{\Gamma}(t_{k+1}, t_k; \mathbf{x}_k)$ is $\mathbf{\Gamma}_3$, which is $\mathbf{\Gamma}_{\text{down}}$ in this example.

Reasonable statistics for the process noise for a given PPD are not readily apparent. For ease of analysis the process noise is assumed to be a Gaussian random variable. However, if some information about the particular jammer being modeled is known *a priori*, then it can be incorporated into the statistics of $\mathbf{v}$. The *a priori* information could be determined from a survey of the process noise statistics of current PPDs, but such a survey is beyond the scope of this work. If a white Gaussian noise model is assumed, then the process noise vector is sampled from a normal distribution:

$$\mathbf{v} \sim \mathcal{N}(\mathbf{0}, \mathbf{Q}) \tag{3.18}$$

where $\mathbf{0}$ is a vector with only zero entries, and $\mathbf{Q}$ is the positive semidefinite symmetric process noise covariance matrix. The process noise covariance matrix $\mathbf{Q}$ is a user-defined tuning parameter.

There are several inherent assumptions in the above state-space model. Perhaps the most important is that the process noise vector applies equally at the end of each mode. This is a reasonable assumption if the propagation time, t_k to t_{k+1}, is no more than one full chirp period T, thereby involving no more than two mode end times. If the propagation time is greater than T, then the above state space dynamics model would tend to introduce unreasonable time correlations in its process noise model. Therefore, the restriction on t_k to t_{k+1} is enforced in this study.

3.4 Multi-Jammer Polynomial Signal Model State-Space Dynamics

There might be situations where the signals from multiple PPDs are received simultaneously at a receiver station. The previously developed state space model should be modified so that it can also work for the multi-signal case. Every PPD examined by the authors have been found to be independent of every other PPD. Therefore, the resulting multi-PPD model would use multiple independent hybrid systems, one for each PPD. Thus, the the matrices $\mathbf{\Phi}(t_{k+1}, t_k; \mathbf{x}_k)$ and $\mathbf{\Gamma}(t_{k+1}, t_k; \mathbf{x}_k)$ are only dependent on the single state vector $\mathbf{x}_k$ of a particular PPD and never on a second state vector from a different PPD. The arguments denoting the nonlinear dependencies of $\mathbf{\Phi}(t_{k+1}, t_k; \mathbf{x}_k)$ and $\mathbf{\Gamma}(t_{k+1}, t_k; \mathbf{x}_k)$ on the state vector are dropped in the remainder of this subsection for notational convenience.

The discrete-time state-space dynamics equation for multiple PPD chirp signals is:

$$\underline{\mathbf{x}}_{k+1} = \underline{\mathbf{\Phi}}\, \underline{\mathbf{x}}_k + \underline{\mathbf{\Gamma}}\, \underline{\mathbf{v}}_k \tag{3.19}$$

where the underlined terms are defined for N_J jammers as:

$$\underline{\mathbf{x}} = \begin{bmatrix} \mathbf{x}^1 \\ \vdots \\ \mathbf{x}^{N_J} \end{bmatrix} \tag{3.20}$$

$$\underline{\mathbf{v}} = \begin{bmatrix} \mathbf{v}^1 \\ \vdots \\ \mathbf{v}^{N_J} \end{bmatrix} \tag{3.21}$$

$$\underline{\mathbf{\Phi}} = \begin{bmatrix} \mathbf{\Phi}^1 & 0 & 0 \\ 0 & \ddots & 0 \\ 0 & 0 & \mathbf{\Phi}^{N_J} \end{bmatrix} \tag{3.22}$$

$$\underline{\mathbf{\Gamma}} = \begin{bmatrix} \mathbf{\Gamma}^1 & 0 & 0 \\ 0 & \ddots & 0 \\ 0 & 0 & \mathbf{\Gamma}^{N_J} \end{bmatrix} \tag{3.23}$$

where each term with a superscript * is the single-jammer form of that same term for jammer number *. These superscripts are not exponents. The propagation assumes that every PPD state vector is propagated from the same start time, t_k, to the same end time, t_{k+1}. Note, the mutli-PPD process noise vector $\underline{\mathbf{v}}$ has uncorrelated individual noise vectors $\mathbf{v}$ between the N_J jammers. Therefore, each of the N_J PPDs has completely independent dynamics and can be simulated independently.

3.5 Model of the Received Jammer Signal

The noise-free model of the received PPD signal is:

$$\begin{aligned} y(t_i; \mathbf{x}, f_{\text{mix}}) &= Ae^{\text{i}2\pi(\theta(t_i;\mathbf{x}))}e^{\text{i}2\pi(-f_{\text{mix}}t_i)} \\ &= Ae^{\text{i}2\pi(\theta(t_i;\mathbf{x})-f_{\text{mix}}t_i)} \\ &= Ae^{\text{i}2\pi(\Theta(t_i;\mathbf{x},f_{\text{mix}}))} \end{aligned} \tag{3.24}$$

where i is the imaginary number, i is the sample index, y is the received signal in units of volts, f_{mix} is the mixing frequency in units of Hertz, and $\Theta(t_i; \mathbf{x}, f_{\text{mix}})$ is the down-mixed phase time-history in units of cycles. This phase time-history is defined as the difference between $\theta(t_i; \mathbf{x})$ and $f_{\text{mix}}t_i$, where $\theta(t_i; \mathbf{x})$ is determined by evaluation of Eq. (3.4) at the current state. Complex sampling is assumed.

The total model of the received PPD signal includes measurement noise that will be represented by the white Gaussian random variable ν'_i, as in:

$$y_i = y(t_i; \mathbf{x}, f_{\text{mix}}) + \nu'_i \tag{3.25}$$

which leads to the definition of the complex measurement noise vector $\boldsymbol{\nu}'$ for samples 1...N:

$$\boldsymbol{\nu}' = \begin{bmatrix} \nu'_1 \\ \vdots \\ \nu'_N \end{bmatrix} \tag{3.26}$$

that is assumed to have the following statistics:

$$\boldsymbol{\nu}' \sim \mathcal{N}\left(\mathbf{0}, \sigma^2_{\nu'}\mathbf{I}\right) \tag{3.27}$$

where $\sigma^2_{\nu'}$ is the variance of the complex measurement noise.

If multiple jamming signals are present in the received data, then Eq. (3.25)

is modified as follows:

$$\begin{aligned} y_i &= \sum_{m=1}^{N_J} y_i^m(t_i; \mathbf{x}^m, f_{\text{mix}}) + \nu_i' \\ &= y_i^1(t_i; \mathbf{x}^1, f_{\text{mix}}) + \ldots + y_i^{N_J}(t_i; \mathbf{x}^{N_J}, f_{\text{mix}}) + \nu_i' \end{aligned} \tag{3.28}$$

where the superscript ^{m} denotes jammer number m, and not the quantity raised to the power m. Only the case of the single received PPD signal is considered in all of the remaining chapters, with the exception of the Chapter 6. Although, many of the developed algorithms can be generalized to consider the case of multiple PPDs.

For notational convenience the model of the received RF samples from Eq. (3.25) is stacked in a real-valued column vector, $\mathbf{y}$, with the real and imaginary parts listed as separate entries:

$$\mathbf{y}(\mathbf{t}; \mathbf{x}, f_{\text{mix}}) = \begin{bmatrix} Re\left(y(t_1; \mathbf{x}, f_{\text{mix}}) + \nu_1'\right) \\ Im\left(y(t_1; \mathbf{x}, f_{\text{mix}}) + \nu_1'\right) \\ \vdots \\ Re\left(y(t_N; \mathbf{x}, f_{\text{mix}}) + \nu_N'\right) \\ Im\left(y(t_N; \mathbf{x}, f_{\text{mix}}) + \nu_N'\right) \end{bmatrix} \tag{3.29}$$

where $\mathbf{t}$ is the vector of the sample times $1...N$, $Re(*)$ is defined as the real part and $Im(*)$ is defined as the imaginary part of the quantity $*$. The realistic received signal can be further be broken up into separate vectors, one for the ideal received signal and one for the noise:

$$\mathbf{y} = \bar{\mathbf{y}} + \boldsymbol{\nu} \tag{3.30}$$

where the functional dependence has been dropped for notational convenience, and the vector $\bar{\mathbf{y}}$ is the deterministic part of the measurement as modeled by the real and imaginary parts of the function $\mathbf{y}(\mathbf{t}; \mathbf{x}, f_{\text{mix}})$ evaluated at N sample times.

Note that it is also the expectation value of the random variable vector **y**:

$$\bar{\mathbf{y}} = E[\mathbf{y}] \tag{3.31}$$

where $E[\ ]$ is the expected value operator, and where $\boldsymbol{\nu}$ is assumed to have the following statistics:

$$\boldsymbol{\nu} \sim \mathcal{N}(\mathbf{0}, \mathbf{P}_{\nu\nu}) \tag{3.32}$$

where:

$$\begin{aligned} \mathbf{P}_{\nu\nu} &= \sigma_{\nu}^2 \mathbf{I} \\ &= \frac{1}{2}\sigma_{\nu'}^2 \mathbf{I} \end{aligned} \tag{3.33}$$

CHAPTER 4

SIGNAL DETECTION

4.1 Jammer Signal Detection Background and Overview

There are many methods that could be applied to the problem of detecting the PPDs' chirp-style signals. A full survey of the potentially applicable techniques is beyond the scope of this work, but several techniques are mentioned here for reference. The radar community has extensively studied chirp-style signals, and the matched filtering technique is well understood [32, 55, 33, 45, 56]. Time-frequency representation-based methods have also been shown to work well. Some of the more common methods are the Wigner-Ville distribution [25, 12, 49], which has been shown to be equivalent to the dechirp method [29], the Altes distribution [42], the Hough and Radon Transforms [27, 53, 15, 48], and the Bertrand distribution [11]. Other authors have had success using discrete wavelet transorms [51], polynomial phase transforms [60], fast chirp transforms [23], and the sample covariance matrix [41]. Several authors have specifically considered the problem of detecting GNSS interference [41, 21, 22, 30]. One approach uses the automatic gain control (AGC) on a given front-end for interference detection [22, 30].

The detection tests considered in the remainder of this chapter use the standard coherent integration possibly followed by further noncoherent integration. The detection method has been selected based on two criteria. The first criterion is that the signal detection test be sensitive, practical, and easy-to-implement. The second criterion is that the detection test aid in signal acquisition. The first criterion is satisfied by the well-known coherent/noncoherent test statistics, as is evidenced by their numerous applications. The second criterion is satisfied because the state vector that optimizes the test statistic is the same vector that

would be produced by a maximum likelihood state estimator that used the raw samples as its measurements.

The dominant challenge in the detection of the real PPD's chirp-style signals is that the full signal structure is not known *a priori*, as can be verified from a simple visual inspection of Figs. 2.7 and 3.1. The order and shape of the polynomials that would best describe Figs. 2.7 and 3.1 are not the same. The periods T, the starting frequencies f_0, the ramp rates c_1^{u}, and the signal amplitudes A, are significantly different. This is true even in PPDs with physically identical appearances. The only similarities between different jammers appears to be the general form of the two-ramp frequency behavior, and a common target frequency, the GPS L_1 frequency. The coherent and noncoherent summation statistics will be evaluated based on their abilities to meet this challenge.

4.2 Coherent Hypothesis Test

The most powerful type of hypothesis test for signal detection is a Neymann-Pearson hypothesis test, also known as a generalized likelihood ratio test. If a statistical distribution of the states in the vector $\mathbf{x}$ were known *a priori* then the pdfs used in the Neymann-Pearson test would be integrated over the known distributions to effectively remove the hypothesis test dependence on those states. The resulting test would take the form:

$$\Lambda' = \frac{p\left(\mathbf{y}|\mathrm{H}_1\right)}{p\left(\mathbf{y}|\mathrm{H}_0\right)} \tag{4.1}$$

where the numerator term $p\left(\mathbf{y}|\mathrm{H}_1\right)$ is the probability density function (pdf) for hypothesis H_1: the hypothesis that the vector of the received samples $\mathbf{y}$ is drawn from the pdf with the PPD signal present. The denominator term $p\left(\mathbf{y}|\mathrm{H}_0\right)$ is the pdf for hypothesis H_0: the hypothesis that the vector of the received samples $\mathbf{y}$ is drawn from the pdf with no PPD signal present.

Unfortunately, *a priori* distributions are not available for any of the elements of $\mathbf{x}$, and a formal Neymann-Pearson test cannot be evaluated. Therefore, a common suboptimal test is formulated that attempts to optimize the test statistic over the state vector $\mathbf{x}$ through a state search. This effectively tests many different hypothesis states until one that is close to the real state causes signal detection, or no signal is detected for any hypothesis state. The suboptimal test statistic takes the following form:

$$\Lambda = \max_{\mathbf{x}} \frac{p\left(\mathbf{y}|\mathbf{t};\mathbf{x},f_{\text{mix}},\text{H}_1\right)}{p\left(\mathbf{y}|\text{H}_0\right)} \tag{4.2}$$

where the probabilities are the same as before, but the numerator pdf is now conditioned on the hypothesis state and the two system parameters: the time vector and the mixing frequency. It should be noted that the above test is normally only slightly suboptimal and is very useful for signal detection.

If Gaussian pdfs are assumed for the measurement noise in Eq. (4.2), and the resulting pdf ratio is optimized over the amplitude, A, and initial phase, θ_0, then the coherent integration test statistics, γ_{c}, is:

$$\gamma_{\text{c}} = \frac{1}{N\sigma_\nu^2}\left(I^2 + Q^2\right) \tag{4.3}$$

where I and Q are defined as:

$$\begin{aligned} I &= \sum_{i=1}^{N} Re\left(y_i\right) Re\left(\frac{\bar{y}_i}{A}\right) + Im\left(y_i\right) Im\left(\frac{\bar{y}_i}{A}\right) \\ &= \sum_{i=1}^{N} I_i \end{aligned} \tag{4.4}$$

$$\begin{aligned} Q &= \sum_{i=1}^{N} Im\left(y_i\right) Re\left(\frac{\bar{y}_i}{A}\right) - Re\left(y_i\right) Im\left(\frac{\bar{y}_i}{A}\right) \\ &= \sum_{i=1}^{N} Q_i \end{aligned} \tag{4.5}$$

The final coherent test statistic, γ_{c}, is then maximized with respect to the remaining elements of the state, $\mathbf{x}$, beyond the initial phase, θ_0, and the amplitude, A. If

the resulting statistic is greater than a user-defined threshold, then a PPD signal is considered to be detected.

The final coherent hypothesis test has one important limitation that will degrade its utility for PPD signal detection. It requires phase coherency over the full accumulation period of Eqs. (4.4) and (4.5). The state used in the hypothesis test must be very close to the true signal state to satisfy the phase coherency requirement. This is typically achieved using a state grid search. When more samples are used in the test statistic to improve its sensitivity, the requirement of phase coherency forces a finer resolution on the state search. The high dimensionality of the signal state makes the coherent test's grid search computationally unattractive for even a modest value of N, the number of samples. A low value of N can be used, but the power of the test will not be high enough. Furthermore, coherent integration will be limited to at most one chirp period due to a level of process noise that can sometimes dramatically changes the PPD polynomial behavior. Significant chirp-to-chirp polynomial variation is present in the PPD that produced Fig. 2.9.

4.3 Standard Noncoherent Hypothesis Test

The noncoherent hypothesis test is better suited to the detection of signals with phase coherency issues. If the accumulations I and Q are assumed to contain stationary Gaussian noise, as in Eq. (3.32), then the standard noncoherent hypothesis test statistic, γ_{nc}, takes the following form from [50]:

$$\begin{aligned}\gamma_{\text{nc}} &= \frac{1}{N}\sum_{n=1}^{N_T}\left(\left(\sum_{i=1}^{N}\frac{I_i}{\sigma_\nu}\right)^2+\left(\sum_{i=1}^{N}\frac{Q_i}{\sigma_\nu}\right)^2\right)_n \\ &= \frac{1}{N\sigma_\nu^2}\sum_{n=1}^{N_T}\left(\left(\sum_{i=1}^{N}I_i\right)^2+\left(\sum_{i=1}^{N}Q_i\right)^2\right)_n \end{aligned} \tag{4.6}$$

where N is the number of complex samples used in the coherent accumulations and N_T is the number of coherent accumulations that have been summed together to produce the noncoherent test statistic, γ_{nc}. There should be no shared samples in any of the N_T accumulations.

The noncoherent hypothesis test effectively re-estimates the initial phase at each of the N_T intervals and assumes that it is independent from the other intervals. If the signal phase were coherent and if the true states that produced the phase time-history were known then this would involve a significant loss of detection power. However, if the signal was coherently integrated over the NN_T samples and the hypothesis state's predicted phase time-history was incorrect, then the loss of detection power could be orders of magnitude worse. Therefore, the noncoherent integration model is the more robust approach and it will be pursued in the remainder of this chapter.

The signal is said to be detected, and hypothesis H_1 accepted, if γ_{nc} is greater than a threshold value $\gamma_{\text{nc,Th}}$:

$$\text{Accept H}_1 \text{ if: } \gamma_{\text{nc}} \geq \gamma_{\text{nc,Th}} \tag{4.7}$$

otherwise the signal is not detected and hypothesis H_0 is accepted:

$$\text{Accept H}_0 \text{ if: } \gamma_{\text{nc}} < \gamma_{\text{nc,Th}} \tag{4.8}$$

The pdf for γ_{nc} under hypothesis H_1, the signal present hypothesis, is a noncentral χ^2 distribution:

$$p\left(\gamma_{\text{nc}}|\mathbf{x}, f_{\text{mix}}, \text{H}_1\right) = \frac{1}{2}\left(\frac{\gamma_{\text{nc}}}{\lambda}\right)^{\frac{1}{2}(N_T-1)} e^{-\frac{1}{2}(\gamma_{\text{nc}}-\lambda)} I_{N_T-1}\left(\sqrt{\lambda\gamma_{\text{nc}}}\right) \tag{4.9}$$

where $I_{N_T-1}(*)$ is a modified Bessel function of the first kind. When the optimally estimated state used in the detection statistic is exactly the same as the true state used in the signal the term λ becomes:

$$\lambda = NN_T\left(\frac{A}{\sigma_\nu}\right)^2 \tag{4.10}$$

The dependence of λ on the state appears to be restricted to only the amplitude state A, but this is only the case under the restricted scope listed above. A more complicated expression could be derived for the case when the hypothesized state, $\mathbf{x}$, is different from the true signal state. In that case, λ could potentially be influenced by all of the elements of $\mathbf{x}$, with the exception of the initial phase state, θ_0, because the joint optimization with respect to A and θ_0 that produced Eq. (4.3) acts to remove all θ_0 dependence. The development of an approximate expression for λ that depends on the other state elements is deferred until the results in Section 4.7.

The pdf for γ_{nc} under hypothesis H_0, the no signal hypothesis, is a standard χ^2 distribution of degree $2N_T$:

$$p\left(\gamma_{\text{nc}}|\text{H}_0\right) = \frac{1}{2^{N_T}\Gamma\left(N_T\right)}\gamma_{\text{nc}}^{N_T-1}e^{-\gamma_{\text{nc}}/2} \tag{4.11}$$

where $\Gamma(*)$ is the gamma function with argument $*$, and not the state-space $\mathbf{\Gamma}$ from Chapter 3.

The two important probability quantities for a signal detection hypothesis test are the probability of false alarm, P_{FA}, and the probability of missed detection, P_{MD}. The P_{FA} is the probability that H_1 will be accepted when H_0 is correct, and the P_{MD} is the reverse. They are determined as follows. The user arbitrarily selects a P_{FA} and determines the corresponding test statistic threshold, $\gamma_{\text{nc,Th}}$, by inverting the cumulative distribution function (cdf) associated with H_0:

$$P_{\text{FA}} = \int_{\gamma_{\text{nc,Th}}}^{\infty} p\left(\gamma_{\text{nc}}|\text{H}_0\right) d\gamma_{\text{nc}} \tag{4.12}$$

Then the P_{MD} is determined by integrating the cdf associated with H_1:

$$P_{\text{MD}} = \int_{\infty}^{\gamma_{\text{nc,Th}}} p\left(\gamma_{\text{nc}}|\mathbf{x}, f_{\text{mix}}, \text{H}_1\right) d\gamma_{\text{nc}} \tag{4.13}$$

It follows that the probability of signal detection is:

$$P_{\text{D}} = 1 - P_{\text{MD}} \tag{4.14}$$

4.4 Specific Noncoherent Hypothesis Test

The detection algorithm designer must still make at least four choices. The first choice is the probability of false alarm, P_{FA}, which is an arbitrary user-selected quantity. A typical value might be 0.0001. The second choice is the value of N, the number of samples used in the coherent accumulations. The third choice is the value of N_T, the number of noncoherent sums to use in the hypothesis test. The fourth choice is the selection of the set of state hypotheses to test, which must yield at least one state that is sufficiently close to the optimum state. The limiting factors on the selection of values for N and N_T will be discussed in the next four paragraphs, and then the important considerations for the selection of the detection test's set of hypothesis states will be discussed.

The first limiting factor on the selection of N and N_T is the amount of available computational resources. As discussed in the previous section on coherent hypothesis testing, a larger value of N will require that more hypothesis states be evaluated until one is found that will produce a phase time-history that closely matches the true signal's phase time-history. Additionally, if either N or N_T increases, then so does the number of computations that must be performed for every single hypothesis state's coherent accumulation. The increase in computational effort is related to the number of samples used in each noncoherent accumulation, NN_T.

The second limiting factor on the selection of N and N_T is the effect of process noise. The hypothesis test's model assumes that the phase time-history produced by each hypothesized state is unaffected by process noise. Without this assumption the process noise would need to be added as another set of parameters for which the test statistic would be evaluated, and the resulting increase in search space dimensionality would likely make the full detection algorithm numerically intractable. Process noise can perturb many of the states

in Eq. (3.1).

An illustrative subset of three possible frequency time-histories is shown in Fig. 4.1. The top plot in Fig. 4.1 is the frequency time-history of a PPD without process noise. The middle plot is the frequency time-history of a PPD that has a non-zero process noise value applied to the chirp period state, T, as might occur in a drifting PPD clock. For illustrative purposes the frequency span is assumed to remain constant. A varying T is not modeled in this chapter's noncoherent detection statistic and will cause a significant loss of signal detection power. Signal power will only be accumulated for the fraction of the interval where the frequencies are matched closely enough for effective coherent integration. Unfortunately, the chirp period in the middle plot changes over time, so there is no one value for T that will align the true signal frequency and the hypothesized signal frequency over the entire displayed interval. Therefore, some accumulation energy and signal detection power will be lost. The bottom plot contains non-zero process noise on the frequency polynomial coefficients in $\mathbf{c}^{\mathrm{u}}$ and $\mathbf{c}^{\mathrm{d}}$. This type of process noise effect is not modeled in this chapter's noncoherent detection statistic and will therefore cause a moderate loss of signal detection power. The amount of lost accumulation energy will be determined by the resulting phase drift during the accumulations. If an error of the type shown in the middle or bottom plots of Fig. 4.1 occurs, and that error is significant enough that no power is accumulated in the final chirp period's coherent integrations, then the accumulation interval, NN_T, is too long.

The above two paragraphs on the factors limiting the sizes of N and N_T imply the following two constraints. N should be constrained to span at most one or two chirp periods. If not, the number of operations becomes computationally intractable on some current desktop computers. N_T's constraint is strongly dependent on the available computational resources, the signal's process noise,

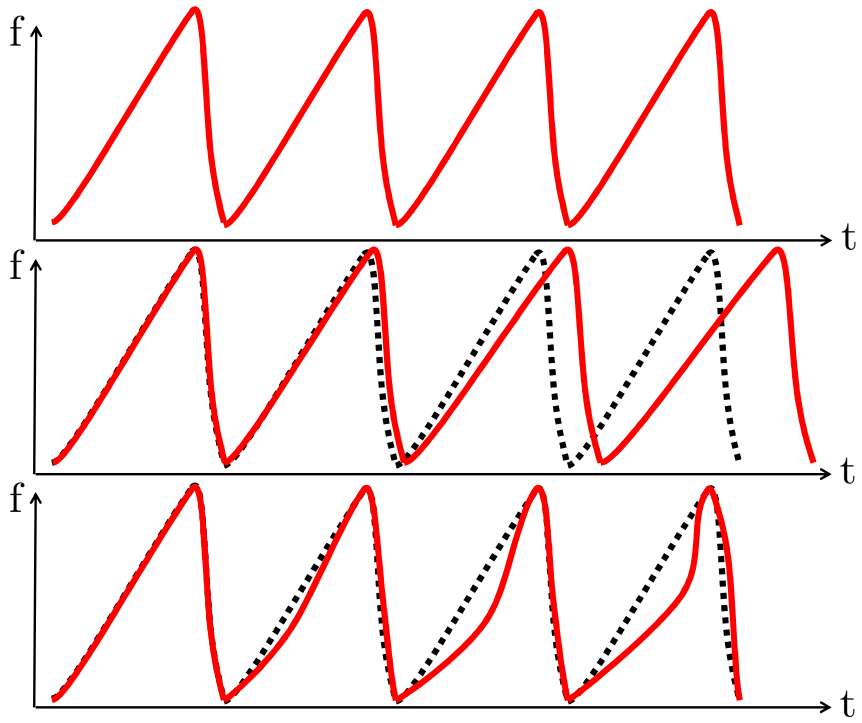

Figure 4.1: Three possible frequency time-histories for a PPD. The top plot is the no-process noise case, the middle plot has process noise perturbing only the T state, and the bottom plot has process noise perturbing only the $\mathbf{c}^{u}$ and $\mathbf{c}^{d}$ state vectors.

and the desired signal detection power. As can be inferred from the next section of this chapter, the number of hypothesis states that must be evaluated increases nonlinearly with an increasing N_T. The process noise level on the signal period T is dependent on the individual PPD signal and the quality of the receiver's clock. Therefore, the algorithm designer must select this value to meet his/her needs, but an $N_T = 50$ can be computed in a short amount of time on a modern desktop computer in MATLAB, and it appears to still contribute signal detection power in the final chirp period of the PPDs tested in this chapter. Larger values of N_T are likely possible.

The hypothesized state vectors, $\mathbf{x}$, used in the noncoherent test must still be determined. In fact, many different values of the state must be tried to find one that maximizes γ_{nc}. As currently formulated, all of the elements of the state vector from Eq. (3.1), with the exception of states θ_0 and A, must be optimized via a brute-force search. Recall that each choice of these values is used in Eqs. (4.4) and (4.5) to define the quantity $\frac{\bar{y}_i}{A}$. The dimensionality of $\mathbf{x}$ is large enough to make brute-force search methods very slow or even computationally intractable. Therefore, the focus of the next few paragraphs will be on ways to structure the noncoherent hypothesis test so that the state dimensionality is reduced to a form more numerically tractable for such a search. Of course, this reduction will also make the model's signal detection test further sub-optimal.

Figs. 2.7 and 3.1 show that a typical PPD spends the majority of its time, and therefore energy, in the frequency ramp-ups. As a result, the frequency ramp-downs will be ignored for signal detection. The restriction of the hypothesis test to the positive frequency ramps removes the hypothesis test's dependence on the vector $\mathbf{c}^{\text{d}}$ and the time down state t^{d}. The remaining states that must be searched are: f_0, t^{u}, T, and $\mathbf{c}^{\text{u}}$. The resulting search dimensionality is $3+\text{M}_{\text{u}}$. Depending on the resources available and the order of the jammer polynomial, this

may be a computationally tractable number for testing the signal detection hypotheses in a brute-force grid search. This assumption causes the loss of phase coherency from chirp-to-chirp. Therefore, the maximum coherent accumulation interval must be no more than the ramp-up portion of a single chirp.

The number of the search dimensions can be further reduced by assuming that $M_u = 1$, i.e. the jammer polynomial order is only one. The level of validity of this assumption can be verified by examining Figs. 2.7 and 3.1. Although, there is clearly higher-order behavior in the some of the frequency polynomials, the linear assumption is valid over a fraction of the chirp period. This assumption is conceptually similar to using a first-order derivative to approximate a curved line over a short length. This assumption is appropriate for PPD signal detection, but it is not necessarily valid for precise signal tracking. The resulting search dimensionality after making this assumption is four. This search dimensionality is computationally tractable in many, but not all, systems.

If a search of four dimensions is still too large for the available computational resources, then the jammer frequency state, f_0, can also be removed from the test. This can be accomplished by assuming that the jammer is targeting a specific frequency, and that the jamming signal will pass through that target frequency. The PPDs in this current work were designed to target the GPS L_1 frequency, $f_{L_1} = 1575.42$ MHz, and the detection model will assume that the mid-point of each ramp-up crosses f_{L_1} exactly. As will be discussed later in Section 4.7, inaccuracies in this model assumption will cause loss of detection power, but experience shows that the the losses are usually acceptable, especially when weighed against the advantage of reducing the search-space dimensionality. Thus, in this model the chirp signal ramps linearly from $f_{L_1} - c_1^u \frac{T}{2}$ to $f_{L_1} + c_1^u \frac{T}{2}$. The final noncoherent hypothesis test must be evaluated using many different partial state hypotheses in a brute-force grid search over the follow-

ing three quantities: c_1^{u}, t_{L_1} and T. These quantities comprise the partial state hypothesis vector $\mathbf{x}_{\mathrm{p}}$:

$$\mathbf{x}_{\mathrm{p}} = \begin{bmatrix} c_1^{\mathrm{u}} \\ t_{\mathrm{L}_1} \\ T \end{bmatrix} \tag{4.15}$$

The new term t_{L_1} is similar to t^{u}. It is the time that the frequency of the modeled signal equals f_{L_1}. In the remainder of the chpater it is assumed that a 3 dimensional search space is tractable.

The final detection algorithm requires a brute-force search over three dimensions. A graphical representation of the search is shown in Fig. 4.2. The red line is the frequency-time history of the true signal and the dashed black line is the frequency-time history used in the coherent integrations of the noncoherent test statistic, i.e. the one that generates $\frac{\bar{y}_i}{A}$ for Eq. (4.4) and (4.5). The actual jammer's center frequency is the solid black horizontal line that is labeled f_{L_1}. The three plots have identical parameters for the black dashed lines. These lines vary in different ways, depending on which state is being searched, to produce the brown, blue, and green dashed lines. The top plot shows the frequency time-history for three possible values for c_1^{u}, the middle plot shows three possible values for t_{L_1}, and the bottom plot shows three possible values for T. The coherent accumulations computed on each chirp would be summed to calculate the noncoherent test statistic of Eq. (4.6) for each state hypothesis. If only three values were used for the grid search in each state, then the total number of hypothesis states would be $3^3 = 27$.

The final algorithm is summarized as follows:

1. Select a probability of false alarm, P_{FA}.
2. Select the coherent accumulation interval, which dictates N. This selection is guided by the model parameters to keep the model frequency inside the

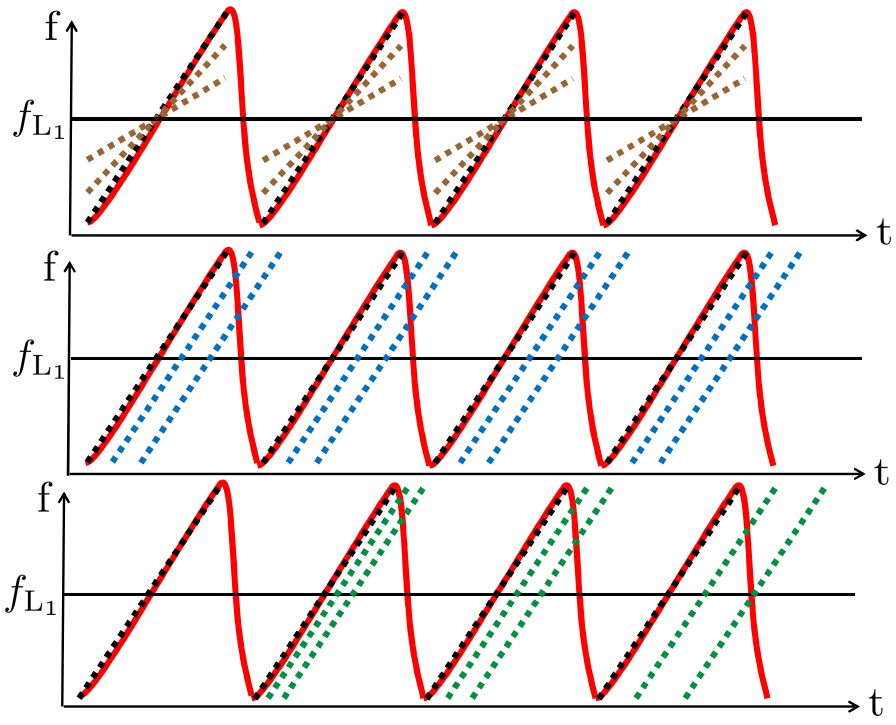

Figure 4.2: The three search dimensions represented graphically for an $N_T = 4$. The top plot depicts the search over c_1^u, the middle over t_{L_1}, and the bottom over T.

range $f_{L_1} - \frac{f_s}{2}$ to $f_{L_1} + \frac{f_s}{2}$, where f_s is the sampling frequency and the bounds are the Nyquist frequency range. Front-end filtering makes any signals outside of this range of dubious value.

3. Select the number of coherent accumulations to use in the noncoherent sum, N_T.
4. Compute the test statistic threshold $\gamma_{\text{nc,Th}}$.
5. Select an untested partial state hypothesis vector, $\mathbf{x}_p$, from the set of hypothesis grid points.
6. Compute the hypothesis phase time-history of the modeled state, with the target frequency f_{L_1} as the frequency in the midpoint of the accumulation.
7. Compute the accumulations of Eqs. (4.4) and (4.5).
8. Compute the final noncoherent test statistic γ_{nc} from Eq. (4.6).
9. Compare the test statistic to the threshold, $\gamma_{\text{nc,Th}}$. Accept hypothesis H_1 if Eq. (4.7) is satisfied, and terminate the grid search.
10. If the grid search of $\mathbf{x}_p$ is completed, then accept hypothesis H_0 and end the grid search.
11. Otherwise, go to step 5).

Note how this algorithm cycles from steps 5) through 11) until it terminates either at step 9) with a detected signal or at step 10) having confirmed the absence of jamming. Also note that the N of Step 2) may not integrate over the full chirp period, because the ramp-up frequency may go outside of the Nyquist frequency bounds. It is assumed that analog RF filters in the data recording system will significantly attenuate signals with frequencies outside of the system's Nyquist range. Therefore, those intervals with a frequency outside of the Nyquist range should be blanked, or the value of N should be reduced so that

the frequency never goes outside of the Nyquist bounds. This is shown graphically in Fig. 4.3. The solid red line is the frequency time-history of a PPD that exceeds the Nyquist bounds of the recording system. The chirp components with frequencies below the lower f_{Nyquist}, and those with frequencies above the upper f_{Nyquist} will be attenuated by the analog RF filters. The frequency time-history that includes the blanking of the samples for the portion of the coherent integration interval outside of the Nyquist range is shown by the black dashed line.

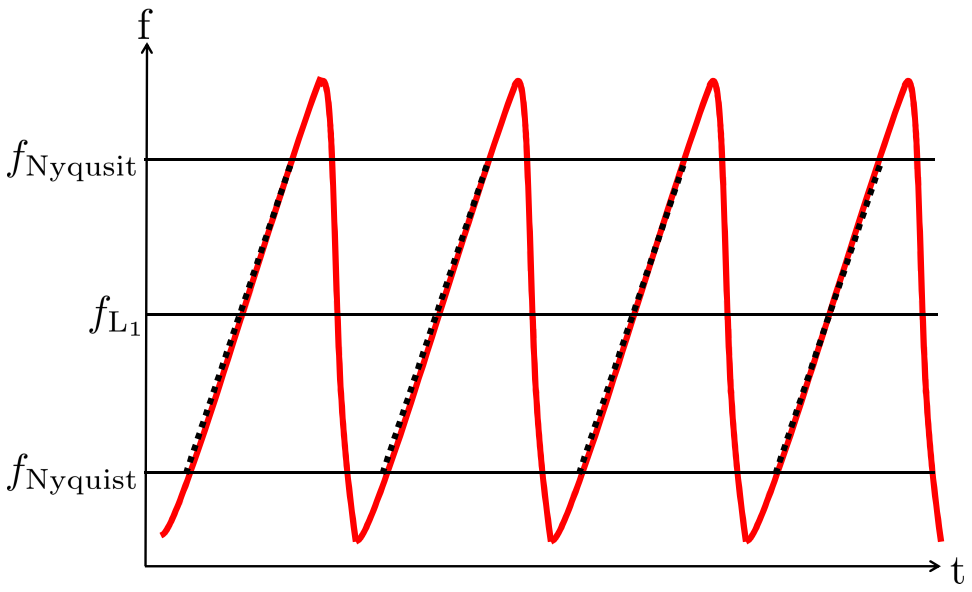

Figure 4.3: An example of a PPD signal that exceeds the Nyquist bounds. The solid red line is the frequency time-history of the received PPD signal and the dashed black line is the corresponding frequency time-history of the optimal hypothesized state for use in computing the detection statistic.

The noncoherent detection algorithm outlined above has not yet addressed how to select the trial set of hypothesis partial state vectors $\mathbf{x}_{\text{p}}$. An efficient procedure for the selection of the partial state hypothesis is presented in the

next section along with practical implementation considerations.

4.5 Jammer State Spacing for a Grid Search

A computationally efficient noncoherent signal detection algorithm attempts to minimize the number of computations while still maintaining the ability to reliably detect weak signals. If the noncoherent detection algorithm of Section 4.4 is adopted, then the algorithm will require a brute-force grid search over the following three quantities: c_1^{u}, t_{L_1}, and T. These quantities comprise the partial state hypothesis vector $\mathbf{x}_{\mathrm{p}}$ in Eq. (4.15). The signal detection's grid search is defined by a uniform spacing between states in each dimension and minimum and maximum values in those same dimensions. A survey of PPDs such as that in [35] can produce reasonable guesses for the possible minimum and maximum values for the states c_1^{u} and T: $c_{1,\min}^{u}$, $c_{1,\max}^{u}$, and $T_{\min}$, $T_{\max}$. The state search range for the quantity t_{L_1} is 0–T.

If a range of minimum and maximum values for each state is known, then the only remaining grid search parameters that need to be selected are the grid spacings for each state. The spacing between two consecutive hypothesis states in each search dimension will comprise a new parameter vector, $\mathbf{p}$:

$$\mathbf{p} = \begin{bmatrix} \delta c_1^{\mathrm{u}} \\ \delta t_{\mathrm{L}_1} \\ \delta T \end{bmatrix} \tag{4.16}$$

where each $\delta *$ element is the distance between consecutive hypothesis states in the * state direction.

The remainder of this section will address the selection of an appropriate vector $\mathbf{p}$. The selection of $\mathbf{p}$ is driven by two criteria. The first is the minimization of the total number of computations required to complete the grid search.

The second criteria is that the spacing must be fine enough that at least one evaluated hypothesis state produces a phase time-history that is close enough to the true signal to cause sufficient power to be generated in the accumulations. The next two subsections develop a formula that quantifies both the total number of computations as a function of $\mathbf{p}$, and the worst-case accumulation energy as a function of $\mathbf{p}$, and the third subsection uses these formulas to develop an optimization problem for selecting $\mathbf{p}$.

4.5.1 Formulation of the Grid Search Computational Cost Using p

The number of state vector values that need to be evaluated in the grid search is the product of the number of values tested in each dimension of the search grid:

$$\mathrm{N}_{\mathbf{x}_\mathrm{p}}(\mathbf{p}) = N_{c_1^{\mathrm{u}}}(\mathbf{p})\, N_{t_{\mathrm{L}_1}}(\mathbf{p})\, N_T(\mathbf{p}) \tag{4.17}$$

where $N_*(\mathbf{p})$ is defined as:

$$N_*(\mathbf{p}) = \left\lfloor \mathrm{floor}\left(\frac{*_{\max} - *_{\min}}{\delta *}\right) + 1 \right\rfloor \tag{4.18}$$

for the grid search state *, and where "floor( )" is the operator that rounds its argument to the nearest integer in the direction of $-\infty$. $\mathrm{N}_{\mathbf{x}_\mathrm{p}}(\mathbf{p})$ can be considered as a measure of the computational cost of the proposed algorithm. A larger $\mathrm{N}_{\mathbf{x}_\mathrm{p}}(\mathbf{p})$ means a larger number of state vector values that must be evaluated in the noncoherent hypothesis test, and therefore a larger number of computations.

Equation (4.17) can be reformulated to facilitate optimization with respect to $\mathbf{p}$. Minimizing $\mathrm{N}_\mathbf{p}$ is functionally equivalent to minimizing $-\frac{1}{\mathrm{N}_{\mathbf{x}_\mathrm{p}}}$. The resulting

cost function, and its linearized approximation are:

$$\mathrm{J_a}\left(\mathbf{p}\right) = \frac{-1}{\mathrm{N}_{\mathbf{x}_\mathrm{p}}\left(\mathbf{p}\right)} \tag{4.19}$$

$$\approx -M_{c_1^{\mathrm{u}}}\left(\mathbf{p}\right) M_{t_{\mathrm{L}_1}}\left(\mathbf{p}\right) M_T\left(\mathbf{p}\right) \tag{4.20}$$

where $\mathrm{J_a}$ is defined as the computational cost of the given state spacing, $\mathbf{p}$, for the grid search noncoherent hypothesis testing of the many possible values of $\mathbf{x}_\mathrm{p}$, and $M_*\left(\mathbf{p}\right)$ is defined as:

$$M_*\left(\mathbf{p}\right) = \left(\frac{\delta *}{*_{\max} - *_{\min}}\right) \tag{4.21}$$

where the approximation in Eq. (4.20) is more useful in some optimization algorithms because each $M_*\left(\mathbf{p}\right)$ is linear with respect to its state vector element, $\delta *$ from Eq. (4.16).

A computationally efficient signal detection algorithm would be designed using a $\mathbf{p}$ that minimizes the computational cost, $\mathrm{J_a}$, of Eq. (4.19), which is equivalent to minimizing Eq. (4.17). The minimization, however, must be carried out subject to a constraint on power loss due to errors between grid states and the optimal state. Otherwise, the optimal elements of $\mathbf{p}$ will grow without bound to yield a very "efficient" search that executes rapidly but without hope of finding the signal.

4.5.2 Accumulation Energy Constraint on the Size of p

A minimum energy constraint ensures that a significant amount of energy is accumulated in at least one of the grid search's hypothesized states, as per Eq. (4.6). As a by-product, such a constraint restricts the size of the entries of $\mathbf{p}$. The constraint takes the form:

$$\mathrm{E}\left(\mathbf{p}\right) \geq \eta \mathrm{E}_{\max} \tag{4.22}$$

where $\mathrm{E}(\mathbf{p})$ is the worst-case maximum energy over the search grid and $\mathrm{E}_{\max}$ is the maximum energy of a noise-free statistic:

$$\mathrm{E}_{\max} = N_T N^2 A^2 \tag{4.23}$$

$\mathrm{E}_{\max}$ occurs when the hypothesis state perfectly matches the signal state and when there is no noise in the recorded samples. η is a tuning parameter with a value between 0 and 1. It is the minimum fraction of the maximum energy ($\mathrm{E}_{\max}$) that is required to be in the accumulation of at least one state in the set of all hypothesized states. In general, a larger value of η will create a more sensitive signal detection test by forcing $\mathrm{E}(\mathbf{p})$ to be larger. However, it will also increase the computational load by forcing the grid search to evaluate more hypothesis states in order to satisfy the constraint of Eq. (4.22). The accumulation energy constraint can also be interpreted as a scaled constraint on the minimum value of the maximum noncoherent test statistics, γ_{nc}, in the absence of signal noise.

The worst-case energy term on the left side of the inequality in Eq. (4.22) can be derived from the noncoherent accumulation of Eq. (4.6):

$$\mathrm{E}(\mathbf{p}) \approx \frac{A^2}{T_{\mathrm{s}}^2} \sum_{n=1}^{N_T} \left(\left(\int_0^{NT_{\mathrm{s}}} \cos\left(\Delta\phi(t, n, \mathbf{p})\right) dt \right)^2 + \left(\int_0^{NT_{\mathrm{s}}} \sin\left(\Delta\phi(t, n, \mathbf{p})\right) dt \right)^2 \right) \tag{4.24}$$

where the coherent sums in Eq. (4.6) have been approximated by their continuous-time integral forms and the term $\Delta\phi(t, n, \mathbf{p})$ is the maximum possible phase difference between the phase predicted by the hypothesized signal state that is closest to the real signal state and the phase of the real signal at time t. Note that $T_{\mathrm{s}} = \frac{1}{f_{\mathrm{s}}}$, the sample period.

The maximum possible phase difference $\Delta\phi(t, n, \mathbf{p})$ is a direct function of the grid search intervals in $\mathbf{p}$, but not a function of the $\mathbf{x}_{\mathrm{p}}$ used in the hypothesis test because a worst-case scenario is assumed in this derivation. The worst case scenario occurs for each state * when the real signal state and the hypothesized

state closest to it differ by exactly $\frac{\delta *}{2}$. In other words, the grid search will evaluate many states that will be consecutively spaced $\delta *$ apart, and the maximum error possible would occur if the true signal state were halfway between the closest two evaluated states for state element $*$. Although, it is unlikely that the true signal state will differ from the closest hypothesized state by the maximum amount for all three states simultaneously, that will be the assumption made in this chapter, and it is conjectured that this is a conservative assumption. A less conservative approach might be to assume that the errors for each state are uniformly distributed along the $\delta *$ interval.

A conservative expression for $\Delta\phi\left(t, n, \mathbf{p}\right)$ is developed in three parts in the next few paragraphs. Each state element of $\mathbf{x}_{\mathrm{p}}$, and the corresponding entry of $\mathbf{p}$, is assumed to create a different form of phase error; one for c_1^{u}, another for t_{L_1}, and yet a third type for T. The errors can be seen for each state in the frequency domain in Fig. 4.2, but they would be integrated to find the phase error. The maximum phase errors would likely occur if the true signal state (solid red line) were to have a value halfway between any of the dashed lines.

An error in the first state of $\mathbf{p}$, δc_1^{u}, will cause an error in the frequency ramp rate. The conservative phase error equation that results from δc_1^{u}, in units of cycles, is:

$$\Delta\phi_{\delta c_1^{\mathrm{u}}} = 2\pi\left(\frac{\delta c_1^{\mathrm{u}}}{2}\right)\frac{t^2}{2} \tag{4.25}$$

An error in the second state of $\mathbf{p}$, δt_{L_1}, will cause an error in the initial frequency of the phase time-history. In other words, if the frequency ramp of the true and hypothesis signals are misaligned in time only and the frequency polynomial is assumed to be first-order, then the frequency used to calculate $\frac{\bar{y}_i}{A}$ will be offset from the true signal frequency by an amount related to the time offset and the frequency ramp rate c_1^{u}. The amount of the frequency offset is determined by the frequency ramp rate of the real signal. In lieu of the actual fre-

quency, a reasonable upper bound will be used: the maximum ramp rate used in the search procedure, $c^{\mathrm{u}}_{1,\max}$. The conservative phase error equation that results from δt_{L_1} in units of cycles is:

$$\Delta\phi_{\delta t_{\mathrm{L}_1}} = 2\pi\left(\frac{\delta t_{\mathrm{L}_1}}{2}\right) c^{\mathrm{u}}_{1,\max} t \tag{4.26}$$

An error in the third state of $\mathbf{p}$, δT, will cause a similar frequency offset as δt_{L_1}. The difference between the two is that errors in δT will also be a function of the current noncoherent summation index, n in Eq. (4.24). If $n = 1$, then this term will have no effect because the initial time offset is solely determined by δt_{L_1}, and the period state T does not enter into the calculations. A linear increase in frequency offset is assumed for every term where $n > 1$. The conservative phase error equation that results from δT, in units of cycles, is:

$$\Delta\phi_{\delta T} = 2\pi\left(\frac{\delta T}{2}\right)(n-1)\, c^{\mathrm{u}}_{1,\max} t \tag{4.27}$$

The resulting conservative form of the phase error function, $\Delta\phi\,(t, n, \mathbf{p})$, is a linear combination of the three phase error terms from Eqs. (4.25), (4.26), and (4.27):

$$\Delta\phi\,(t, n, \mathbf{p}) = \Delta\phi_{\delta c^{\mathrm{u}}_1} + \Delta\phi_{\delta t_{\mathrm{L}_1}} + \Delta\phi_{\delta T} \tag{4.28}$$

This function has linear and quadratic terms in t. Therefore, the time integrals of the cos/sin of this function that appear in Eq. (4.24) are Fresnel integrals, which cannot be evaluated analytically. This means that one cannot develop a closed-form expression for the constraint function E($\mathbf{p}$) that is defined in Eq. (4.24) and used in Eq. (4.22). The integrals in Eq. (4.24) are evaluated numerically as part of the procedure for selecting the optimal $\mathbf{p}$. Note that E($\mathbf{p}$) is highly nonlinear in $\mathbf{p}$.

4.5.3 Solution for the Optimal Grid Search Spacing Vector p

The final form of the constrained optimization problem cost function that is used to determine the grid search spacing vector $\mathbf{p}$ is:

$$\min_{\mathbf{p}} J_a(\mathbf{p})$$
$$\text{subject to } E(\mathbf{p}) \geq \eta E_{max} \tag{4.29}$$

where the energy constraint function is defined in Eqs. (4.24)–(4.28), and J_a is either the exact nonsmooth cost function from Eq. (4.19) or the smoothed approximation of Eq. (4.20).

The constrained optimization of Eq. (4.29) can be accomplished in various ways. Fortunately, the optimization does not involve the search for a single peak in an otherwise noisy landscape, as is the case for the state grid search of possible values for $\mathbf{x}_p$ in the noncoherent signal detection algorithm developed in Section 4.4. Equation (4.29) contains no noise and has an approximation that varies smoothly with respect to changes in $\mathbf{p}$. Yet another grid search, one that spans the set of possible values for $\mathbf{p}$, would provide an accurate solution to this optimization, but it would be an unnecessarily slow procedure. Fortunately, the number of dimensions in the optimization of Eq. (4.29) is only 3, which is small enough that many heuristic and gradient-based methods will find a sufficiently low-cost solution quickly.

Experience has shown that heuristic methods are more effective than gradient-descent or Newton-type method for optimizing the original cost function in Eq. (4.19) because of the nonlinear and non-smooth "floor$(*)$" terms. Common heuristic methods include random sampling, simulated annealing, and genetic algorithms. A 3 dimensional search space is small enough that random sampling can provide a parameter vector $\mathbf{p}$ with a low cost J_a in a short amount of time. The procedure used in this work is as follows:

1. Draw a random sample of **p**.
2. Compute the cost of the current sample using Eq. (4.19).
3. If the cost is below the minimum cost of all previous states then check if the constraint of Eq. (4.24) is satisfied. If the constraint is satisfied, accept the current sample of **p** as the new guess of the optimum value.
4. If the cost is not the minimum cost of all previous states, or if the constraint is not satisfied, then return to Step 1).
5. Compare the current cost to the user-defined terminal cost threshold, $J_{a,Th}$. If the threshold is satisfied, then use **p** as the final optimum value and terminate the random sampling algorithm.
6. Determine if the number of candidate **p** evaluations has reached a user-defined upper-limit, N_{evals}. If N_{evals} has been exceeded, then return the current lowest cost **p** and terminate the random sampling algorithm. Otherwise return to Step 1).

In the above random sampling algorithm, the cost should be evaluated before the constraint because the evaluation of the integral in Eq. (4.24) is more time-consuming than the evaluation of the cost function in Eq. (4.19).

Experience has shown that Newton's method and gradient-descent-type methods are more effective than many heuristic methods for optimizing the approximate cost function in Eq. (4.20). The gradient based methods are preferential because Eq. (4.20) is a smooth equation. However, the nonlinear constraint function of Eq. (4.24) can sometimes complicate the minimization. A Gauss-Newton method has been applied with analytic derivatives to the optimization of the approximate cost function of Eq. (4.29), and the nonlinear constraint has been enforced within the gradient method using the method of Lagrange multipliers. An initial guess that was moderately close to the local optimum caused

convergence of the algorithm in as little as two steps.

Experience with both the heuristic and gradient-based methods has led to the following conclusions and recommended optimization procedure for selecting $\mathbf{p}$. The heuristic methods take a long time to find a $\mathbf{p}$ with a cost equivalent to a moderately well initialized Newton-type method, but the final cost of the Newton-type methods can be sensitive to the initial $\mathbf{p}$ estimate and the proximity to some local minima. Therefore, a reasonable optimization procedure is to perform a low iteration-count random-sampling-based optimization of Eq. (4.29), perhaps with 100–10,000 samples, and then to refine the lowest cost $\mathbf{p}$ estimate using a Gauss-Newton method, Lagrange multipliers, and the approximate cost function of Eq. (4.20).

Keep in mind that this is an optimization within an optimization. That is, the procedure just outlined finds the optimum $\mathbf{p}$ for minimizing the amount of computation needed to approximately maximize the signal detection statistic γ_{nc} from Eq. (4.6). The maximization of γ_{nc} must be performed on-line using actual receiver data, which is why it is important to perform this maximization in an efficient manner. Fortunately, the optimization that yields this efficiency, i.e. the optimization of $\mathbf{p}$, can be performed once in an off-line basis for a given set of parameters that define the search intervals of $\mathbf{x}_{\text{p}}$ and the coherent and noncoherent accumulation intervals.

4.6 Further Considerations for Practical Implementation of the Signal Detection Algorithm

There are several practical ways to modify this work's signal detection calculations to reduce the total computation time. Three methods are listed below.

The first method to reduce the computation time is to provide a more accu-

rate initial guess of the signal period, T. If only one PPD signal is assumed to be present, then an accurate estimate of T can be computed using the raw signal's autocorrelation function. A region about the initial T estimate should still be searched to provide accurate results, but the range of $T_{\min}$–$T_{\max}$ can be reduced. If multiple signals are present, or if the correlation interval approaches the 1 ms GPS C/A code, then multiple autocorrelation peaks could appear, and this approach becomes problematic.

The second method to reduce the computation time is to use FFTs to compute the coherent accumulations of Eqs. (4.4) and (4.5) at multiple offsets of the frequency crossing time t_{L_1} for fixed values of c_1^u. This method is well known in the GPS community, and is based on the FFT method for expediting circular cross-correlations [44]. Details are not provided because this work does not implement this method. The numerical results presented in this work are equivalent, but the algorithm execution speed is slower.

The third method to reduce computation time is to make use of correlated states to reduce the total number of accumulations that must be computed. Two of the states used in the search procedure are time quantities, and are not completely independent of each other. The combined search of t_{L_1} and T can create a much denser spacing of accumulations in time than would be required by the δt_{L_1} spacing of the t_{L_1} search or the δT spacing of the T search. Some coherent accumulations will effectively be repeats of earlier computations. An example repeat accumulation is shown graphically in Fig. 4.4. The solid black line represents the frequency time-history of the nominal coherent accumulation, the dotted line uses a perturbed value of t_{L_1}, and the dot-dashed line uses a perturbed value of T. The second accumulation of the perturbed t_{L_1} and the second accumulation of the perturbed T are identical in this example. Recomputing this particular accumulation would be a waste of computational resources. These re-

peat, or near-repeat, accumulations will be very common if a small state spacing is used in the state search grid. The accumulation density will grow in a manner that is related to the product $N_{t_{L_1}}(\mathbf{p})\, N_T(\mathbf{p})$ from Eq. (4.17). This work will make use of the above observations to reduce the total algorithm computation time.

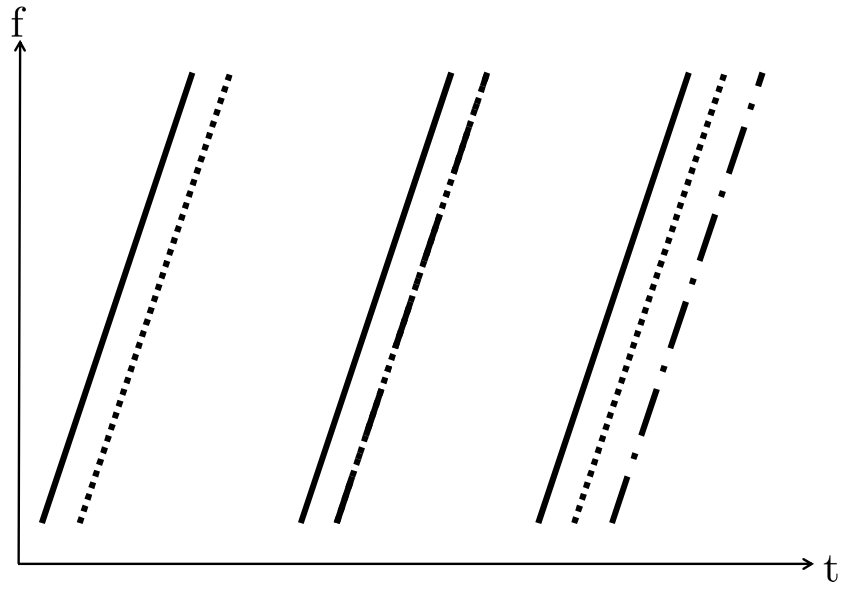

Figure 4.4: The frequency time-histories for a fixed value of c_1^{u} and for two different values of t_{L_1} and T. The solid black line uses the nominal values, the dotted line uses a perturbed t_{L_1}, and the dot-dashed line uses a perturbed T.

The correlated nature of the states implies that the algorithm might not be required to evaluate all three state dimensions, c_1^{u}, t_{L_1}, and T independently in a brute-force search. The computation of the coherent accumulations will be reduced to a 2D search, but the noncoherent sum of Eq. (4.6) will be evaluated in a 3D search. The first dimension of the 2D coherent accumulation grid is due to c_1^{u}, which is not correlated with the time states and must be evaluated independently. The second dimension of the 2D coherent accumulation grid is due to the states t_{L_1} and T. The second dimension will be evaluated using a new

time spacing parameter: δt. This work uses $\delta t = \min[\delta t_{L_1}, \delta T]$. The coherent accumulations are computed in the standard manner for a given c_1^u, but each independent start time is spaced apart by δt to form a grid of start times. The results of this procedure are two 2D arrays of coherent accumulation values, one for I and one for Q. The first dimension corresponds to many different c_1^u values and the second dimension corresponds to many different coherent accumulation start times. The size of the second dimension is a function of N_T, $T_{\max}$, and δt.

The computation of γ_{nc} from Eq. (4.6) for a given $\mathbf{x}_p$ is accomplished by first computing the start times for each coherent accumulation in the noncoherent sum as dictated by the particular t_{L_1} and T values at the given $\mathbf{x}_p$ grid point and then interpolating the existing 2D arrays via a nearest neighbor interpolation to find all of the I and Q coherent accumulation values to use in the noncoherent sum. The original grid spacing, $\mathbf{p}$, for the determination of the set of $\mathbf{x}_p$ values should be reduced to account for possible additional errors that may result from the nearest-neighbor interpolation. This work used a resolution of $\mathbf{p}$ that was twice as fine as the original spacing, and therefore evaluated $2^3 = 8$ times as many noncoherent sums γ_{nc}. The increase in the number of computed γ_{nc} values is very often computationally advantageous over the original full 3D search. If desired, a cost function similar to Eq. (4.19) that uses only two N_* terms, one for δc_1^u and one for δt, can be formulated and optimized to further reduce the computation time.

An example implementation of the above modification was tested on a problem with $N_T = 10$ elements in its noncoherent sum and a state spacing determined from the procedure outlined earlier in this chapter. The number of required accumulations using the single δt term would be approximately 1% of that required by the method of computing an accumulation for each state

hypothesis. The improvement increases as the range for each time state $*$, $*_{\max} - *_{\min}$, increases, and as the spacing for δt_{L_1} and δT decreases. The final computation time improvement is significant because the slowest part of the signal detection procedure is the computation of the coherent accumulations for each hypothesis state, $\mathbf{x}_p$.

4.7 Jammer Signal Detection Results

In this section the noncoherent signal detection algorithm developed earlier in this chapter is tested on real PPD data collected in a laboratory environment. The data were collected at 62.5 MHz with complex samples and uses the same data files as those used to create Figs. 2.7 and 3.1.

4.7.1 The Proposed Algorithm's Probability of False Alarm

The probability of false alarm, P_{FA}, presented in Eq. (4.12) must be modified before it can be used in the current algorithm. Equation. (4.12) assumes that a single sample is drawn from the H_0 pdf (the one that applies when there is no signal). The detection algorithm developed in the previous sections performs a grid search and effectively evaluates many different hypothesized signal states. If the chirp signal is not present then the search effectively samples the distribution of Eq. (4.11), and therefore, the random variable γ_{nc}, many times. The effective number of independent samples of γ_{nc} is defined as $N_{\gamma_{eff}}$.

The probability of false alarm when the number of samples drawn from the distribution is $N_{\gamma_{eff}}$ is defined as $P_{FA,N_{\gamma_{eff}}}$. This is the user-desired probability of false alarm for the total algorithm. $P_{FA,N_{\gamma_{eff}}}$ increases as $N_{\gamma_{eff}}$ increases because more samples are drawn from the distribution. The increased number of samples makes it more likely that one of the samples will be above $\gamma_{nc,Th}$. The equa-

tion that relates $P_{\mathrm{FA},N_{\gamma_{\mathrm{eff}}}}$ and P_{FA} is:

$$P_{\mathrm{FA},N_{\gamma_{\mathrm{eff}}}} = 1 - (1 - P_{\mathrm{FA}})^{N_{\gamma_{\mathrm{eff}}}} \tag{4.30}$$

where P_{FA} is the single sample probability of false alarm and $P_{\mathrm{FA},N_{\gamma_{\mathrm{eff}}}}$ is the multi-sample probability of false alarm. The user would select $P_{\mathrm{FA},N_{\gamma_{\mathrm{eff}}}}$, perhaps 0.0001, and then determine P_{FA}. That value of P_{FA} would then be used to determine $\gamma_{\mathrm{nc,Th}}$ from Eq. (4.12). $\gamma_{\mathrm{nc,Th}}$ will increase as the effective number of independent samples, $N_{\gamma_{\mathrm{eff}}}$, increases.

There are many ways that $N_{\gamma_{\mathrm{eff}}}$ can be calculated. The upper bound on $N_{\gamma_{\mathrm{eff}}}$ is the total number of evaluated hypothesized states, $N_{\mathbf{p}}$. $N_{\gamma_{\mathrm{eff}}} = N_{\mathbf{p}}$ should be used if conservative results are desired. This work attempted to create a more precise estimate of $N_{\gamma_{\mathrm{eff}}}$ by making use of the correlation length of the three states of $\mathbf{x}_{\mathrm{p}}$ and the minimum and maximum search range for each state. The resulting formula for $N_{\gamma_{\mathrm{eff}}}$ is similar to Eq. (4.17):

$$N_{\gamma_{\mathrm{eff}}} \approx N_{c_1^{\mathrm{u}}}(\mathbf{p})_{\mathrm{eff}}\, N_{t_{\mathrm{L}_1}}(\mathbf{p})_{\mathrm{eff}}\, N_T(\mathbf{p})_{\mathrm{eff}} \tag{4.31}$$

where $N_*(\mathbf{p})_{\mathrm{eff}}$ is defined in a manner related to the inverse of Eqs. (4.21):

$$N_*(\mathbf{p})_{\mathrm{eff}} = \left(\frac{*_{\mathrm{max}} - *_{\mathrm{min}}}{*_{\mathrm{corr}}}\right) \tag{4.32}$$

where $*_{\mathrm{max}}$ is the maximum value, $*_{\mathrm{min}}$ is the minimum value, and $*_{\mathrm{corr}}$ is the correlation length of the state $*$. The term $*_{\mathrm{corr}}$ can be determined by first computing many different accumulations on the same data samples for many different values of state $*$. The numerical cross-correlation of the I and Q accumulations are then computed between each of the offsets of state $*$ and the result is normalized. The numerical cross-correlation of the accumulations will drop off as the state $*$ increases. A correlation distance is then assumed. In this work the first null, a numerical cross-correlation of 0, was used. Results are omitted for the sake of brevity.

4.7.2 The Proposed Algorithm's Probability of Detection

The probability of detection, P_{D}, for a given carrier to noise density ratio ($\frac{C}{N_0}$) is a common metric that can be used to analyze the effectiveness of a signal detection algorithm. A closed form solution for the ideal P_{D} can be developed from Eqs. (4.10)–(4.14), and (4.30), for a given set of parameters. Unfortunately, the λ from Eq. (4.10), where $\lambda = NN_T \left(\frac{A}{\sigma_\nu}\right)^2$, and the P_{D} that would result from using this λ, would be optimistic. A more conservative lower bound for both λ and the P_{D} can be determined by approximating the effects of two implicit assumptions that were made in the derivation of this chapter's detection algorithm. Other effects exist that might affect the value of λ, but they are not considered in this work.

The first implicit assumption used in the computation of λ is that the signal is coherently accumulated with the optimal signal phase over N samples. This is not true of the final algorithm proposed in Section 4.4 for at least two reasons. The first reason is that the received chirp signal may not span all N samples in its frequency ramp-up. For example, the actual received signal will have a frequency ramp-down, but this was ignored in the model's simplifying assumptions that led to the selection of $\mathbf{x}_{\mathrm{p}}$. Additionally, the jammer's center frequency may be offset from f_{L_1}. The second reason is that the polynomial order is not necessarily correct. For example, the signal detection test's model assumes that only the c_1^{u} polynomial coefficient is nonzero, but this is not true for some PPDs. As a result, an approximation should be used for N, defined as N_{test}:

$$N_{\mathrm{test}} = \epsilon N \tag{4.33}$$

where ϵ is a number between 0 and 1 that attempts to capture the above listed effects. Conceptually, ϵ is a normalized measure of the validity of the detection test's model for the received PPD signal. For common PPDs, such as that in

Fig. 2.7, ϵ is close to one.

The second implicit assumption used in the computation of λ is that the optimal signal amplitude that results from the signal detection algorithm is the same as that received by the data recording system. A conservative lower bound on the actual amplitude that should be used in the test, A_{test}, can be derived from the constraint in Eq. (4.22):

$$\begin{aligned} \mathrm{E}(\mathbf{p}) &\geq \eta \mathrm{E}_{\max} \\ \left(N_T N^2 A_{\text{test}}^2\right) &\geq \eta \left(N_T N^2 A_{\text{received}}^2\right) \\ A_{\text{test}} &\geq \sqrt{\eta} A_{\text{received}} \end{aligned} \tag{4.34}$$

where the lower bound on A_{test} is $\sqrt{\eta} A_{\text{received}}$.

The more conservative λ, λ_{test}, can now be calculated using Eq. (4.10), (4.33), and (4.34), and is $\lambda_{\text{test}} = N_{\text{test}} N_T \left(\frac{A_{\text{test}}}{\sigma_\nu}\right)^2$. The algorithm designer may try various values of η, N, and N_T until the desired detection sensitivity is met for a given value of $P_{\text{FA,N}_{\gamma_{\text{eff}}}}$ and a given PPD signal.

Figure 4.5 plots the P_{D} versus $\frac{C}{N_0}$ that results from using λ and λ_{test}. The solid lines represent the ideal cases where ϵ and η are 1 (it uses λ). The dashed lines represent the likely conservative lower bound on the P_{D} where ϵ and η are arbitrarily set to 0.95 and 0.8 respectively (it uses λ_{test}). Four different values of N_T are plotted for a $P_{\text{FA,N}_{\gamma_{\text{eff}}}}$ of 0.001 and a coherent integration interval (NT_{s}) of approximately 7μs.

Figure 4.6 plots the P_{D} that results from using λ, λ_{test}, and the numerical results of the proposed detection algorithm applied to the data that were used to produce Fig. 2.7. $P_{\text{FA},N_{\gamma_{\text{eff}}}}$ was set to 0.0001, the coherent integration interval (NT_{s}) to approximately 7μs, and N_T to 10. The solid and dashed lines have the same meaning as in Fig. 4.5. The red circles are the numerical estimates of the P_{D} of the developed algorithm using data collected from the PPD in a labora-

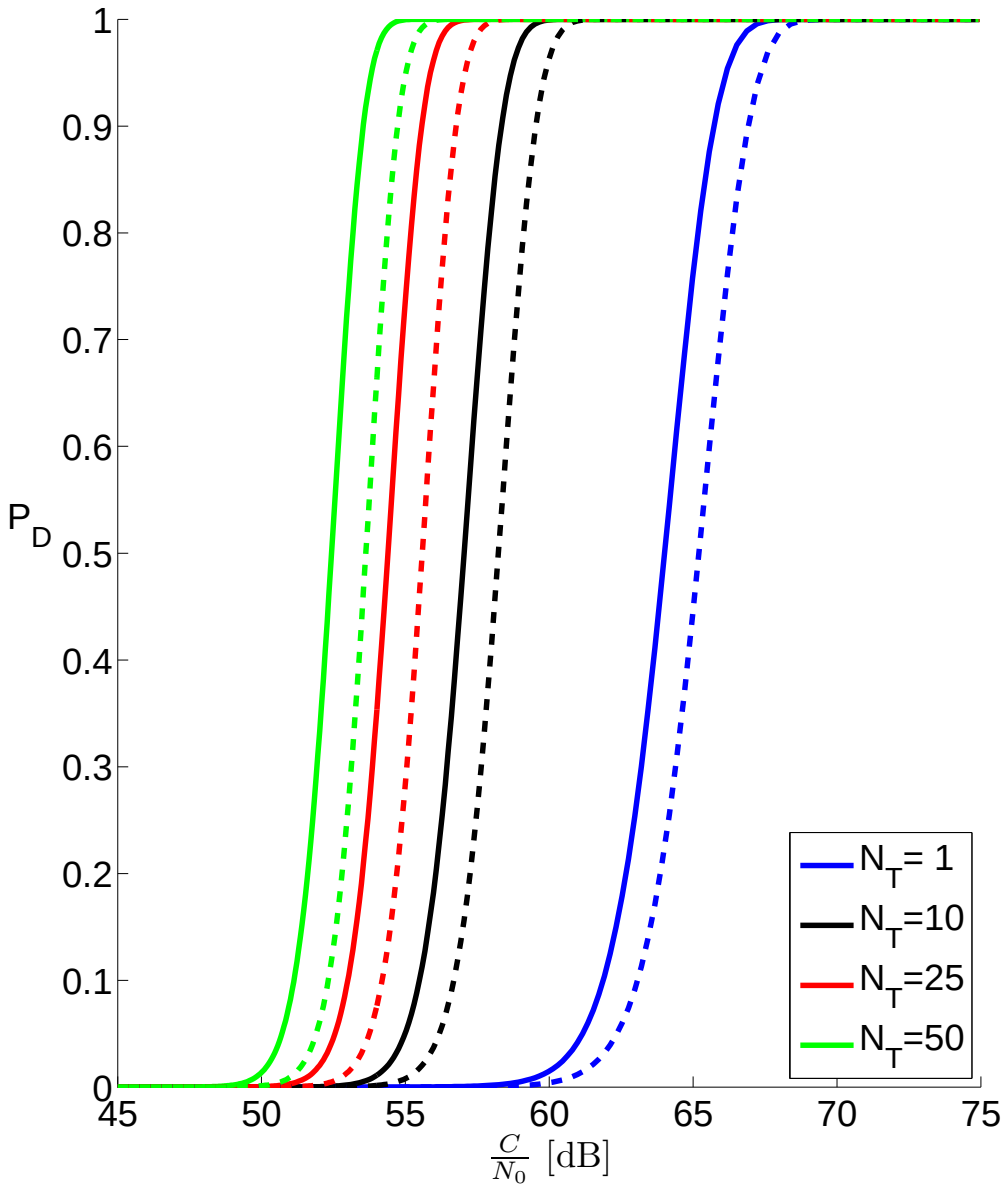

Figure 4.5: The P_{D} versus $\frac{C}{N_0}$ for an ϵ of 0.95 and an η of 0.80.

tory setting, but with noise added during post-processing in MATLAB. The test results were averaged over 100 trials with different noise realizations and used the same parameters as listed above. The results of the algorithm on real PPD data closely approximate that predicted by the theory. There were two effects that caused the numerical results to be closer to the ideal case than the lower bound. The first effect is that the specific algorithm implementation used to create Fig. 4.6 was slightly different than that prescribed in this work because of numerical considerations, and as a result it tended to search more state hypotheses than strictly necessary. The second effect is that the estimate of $N_{\gamma_{\text{eff}}}$ provided to the algorithm appears to be slightly low.

Figure 4.7 is similar to Fig. 4.6, but it was created using the same data from the PPD that produced Fig. 3.1. The ϵ value for this PPD is approximately 0.7, implying that the first-order frequency polynomial assumption is not as valid as for the PPD of Fig. 2.7 which had an ϵ of approximately 1. Therefore, the numerical P_{D} is below the theoretical optimum, but it still above the lower bound.

4.7.3 Real World Implementation Issues

The algorithm developed in this chapter has several minor implicit assumptions that might be violated in a real-world and real-time implementation. The assumption that is most likely to be violated is the implicit assumption of no RF filtering effects in the digitization equipment. If the RF receiver equipment used in the field has pronounced filtering effects then the white noise assumption is violated and the amplitude of the incoming signal will also be a function of the signal's frequency. The filtering effects of the receiver equipment can be determined off-line. The amplitude of the PPDs' signals might also be a function of frequency, but this will be difficult to determine before the first encounter in the field. A survey of the RF filter characteristics of many PPDs might provide a

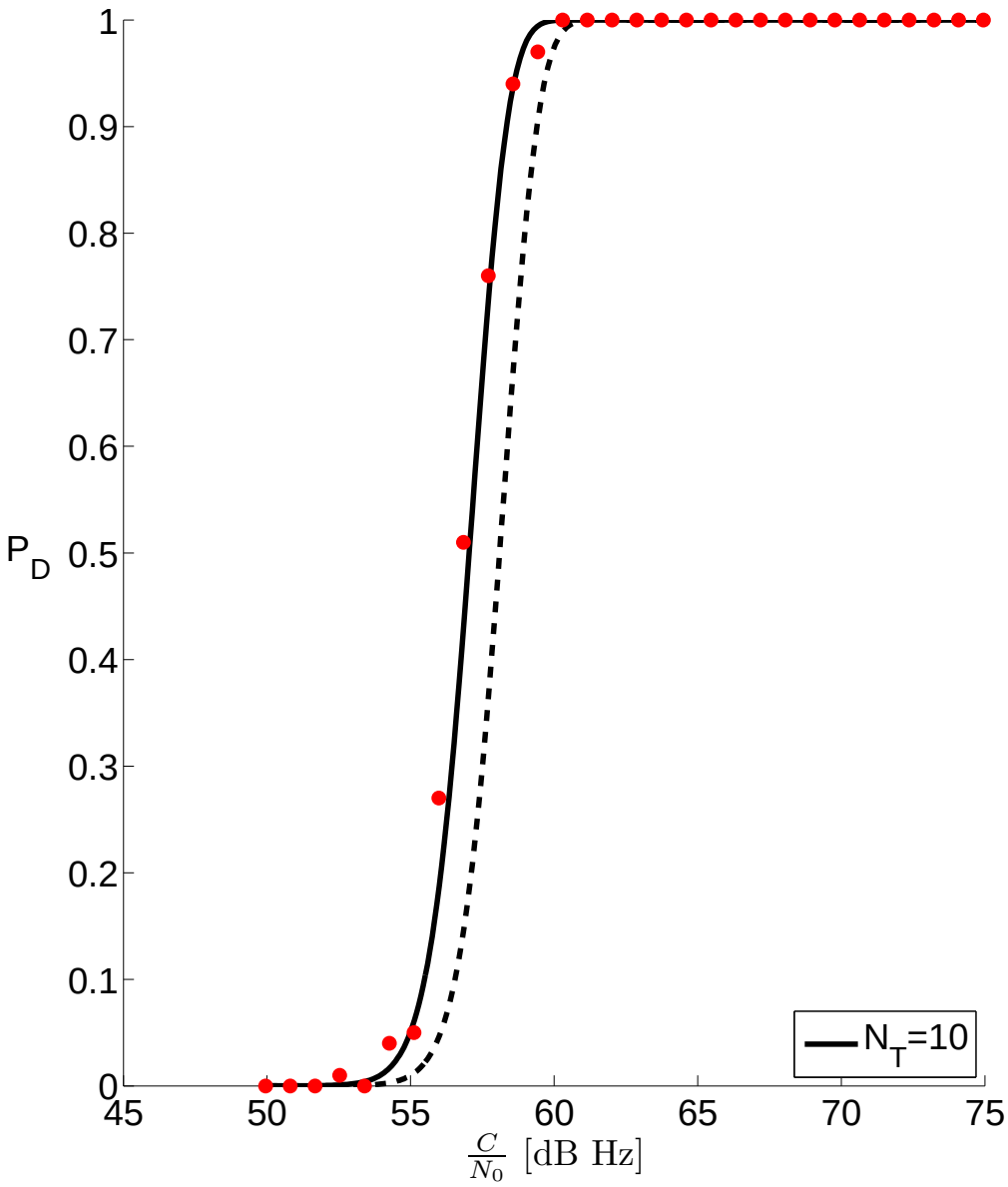

Figure 4.6: The numerical estimate of P_{D} versus $\frac{C}{N_0}$ for an η of 0.80 and averaged over 100 trials.

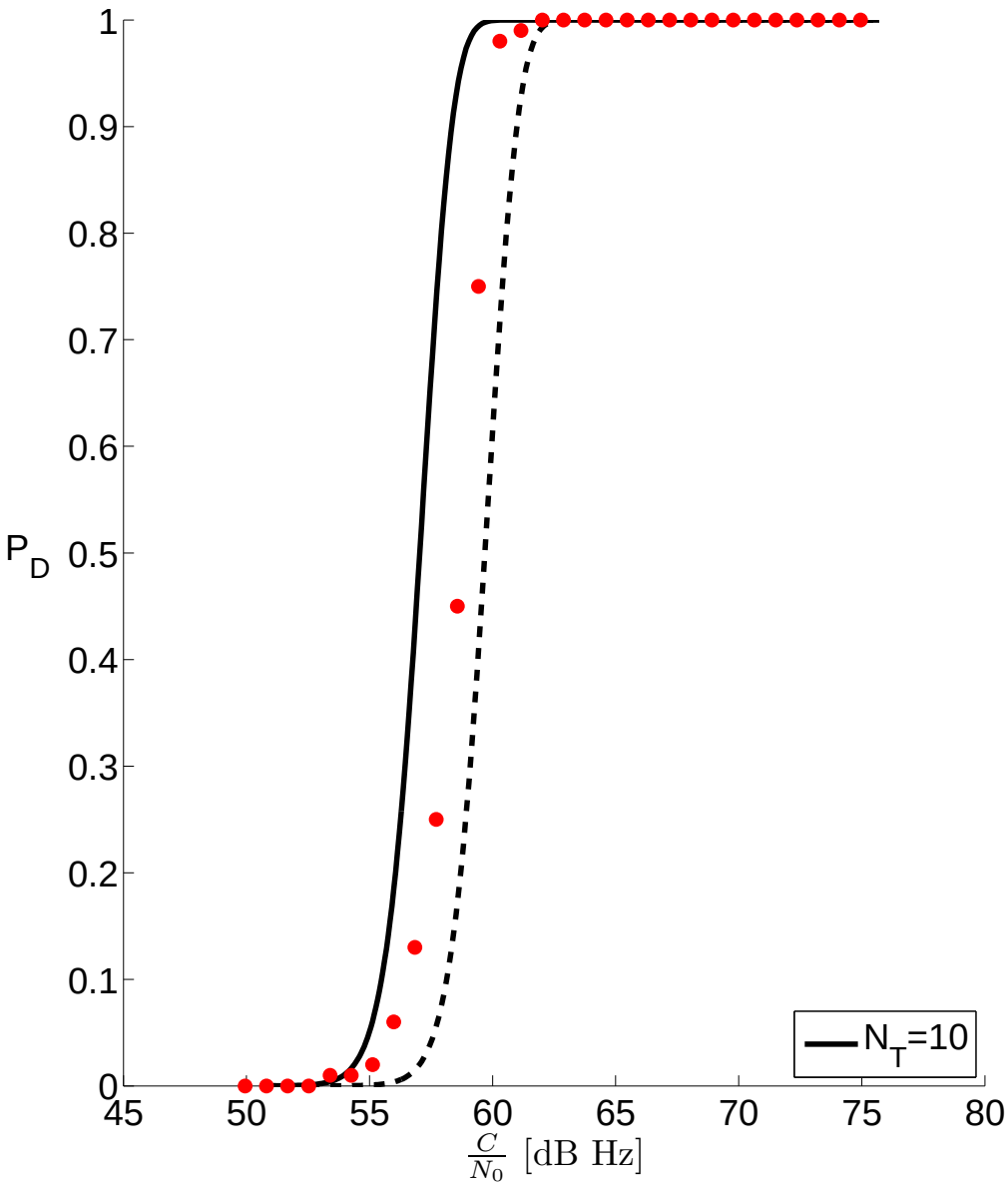

Figure 4.7: The numerical estimate of P_{D} versus $\frac{C}{N_0}$ for an η of 0.80 and averaged over 100 trials.

set of reasonable guesses to use in the development of a new test statistic that includes the RF filtering effects of the transmitter and receiver equipment, but that is beyond the scope of this current work.

CHAPTER 5

SIGNAL ACQUISITION

Once a signal is detected it may be desirable to track the signal in the sense of a Kalman filter [38]. Before Kalman filter tracking can occur however, it is necessary to acquire the signal in order to initialize every term in the Kalman filter's state vector, $\mathbf{x}$. This chapter focuses on the acquisition calculations that accomplish this.

5.1 Acquisition Overview

There are many methods that can develop a good initial estimate of the chirp signal state $\mathbf{x}$. A common method is the implementation of a maximum likelihood estimator (MLE) that uses the raw RF samples as its measurements. It then attempts to match the samples using the signal model. This method will provide the optimal signal state, but its total execution time can be significant. The primary time-increasing issue is that the MLE must distinguish the global minimum from other local minimum that exist due to the nonlinear equations in the signal's measurement model. Therefore, many different initial states would need to be evaluated in order to find one state that would allow the MLE to converge to the global optimum estimate. The acquisition procedure outlined in this disseration does not remove the nonlinear terms, but it does attempt to reduce the number of hypothesized state evaluations required for full signal state acquisition.

The initialization of the state will be accomplished using the results of this work's detection algorithm and a two-step procedure; a rough state acquisition followed by a fine state acquisition. The state, or partial state, output of each step will be used as *a priori* information in the next acquisition step or in the Kalman filter. The detection algorithm will provide $\mathbf{x}_p$, which contains the terms

c_1^{u}, t_{L_1}, and T. The resulting frequency time-history due to a possible $\mathbf{x}_{\mathrm{p}}$ detection output is shown in the top plot of Fig. 5.1. Notice how the top plot fails to include ramp-down portions in its black dashed signal model time-history.

The output of the signal detection test, $\mathbf{x}_{\mathrm{p}}$, will be provided to the rough acquisition procedure to constrain the possibilities for the rough acquisition's state vector, $\mathbf{x}_1$. $\mathbf{x}_1$ is the state vector that best fits the data when c_j^{u} and c_j^{d} are assumed to be 0 for all terms with $j > 1$ and when the signal detection test's output is included as *a priori* information for use in the rough acquisition. Specifically, the rough acquisition procedure will use the values of c_1^{u} and T from $\mathbf{x}_{\mathrm{p}}$ as the same values for those states in $\mathbf{x}_1$. Additionally, the information provided by t_{L_1} will be used along with the constraint that the signal frequency at the beginning of the chirp equals the signal frequency at the end of the chirp to reduce the state uncertainty to a two dimensional subspace. The rough acquisition procedure will then perform a 2D grid search over a small range of states to find the rough acquisition state, $\mathbf{x}_1$. The resulting frequency time-history due to a possible $\mathbf{x}_1$ from the rough acquisition is shown in the middle plot of Fig. 5.1. Notice how the ramp-down portions are modeled by $\mathbf{x}_1$.

The fine acquisition procedure applies an MLE to the model in order to fit the data. The MLE optimizes $\mathbf{x}$ in a way that permits variation on all states, but uses the state from the rough acquisition, $\mathbf{x}_1$, as its initial state estimate. The resulting frequency time-history due to a possible MLE-produced $\mathbf{x}$ is shown in the bottom plot of Fig. 5.1. Notice how the fit between the dashed modeled curve and the solid received data curve improves for each successive plot from top to bottom in Fig. 5.1.

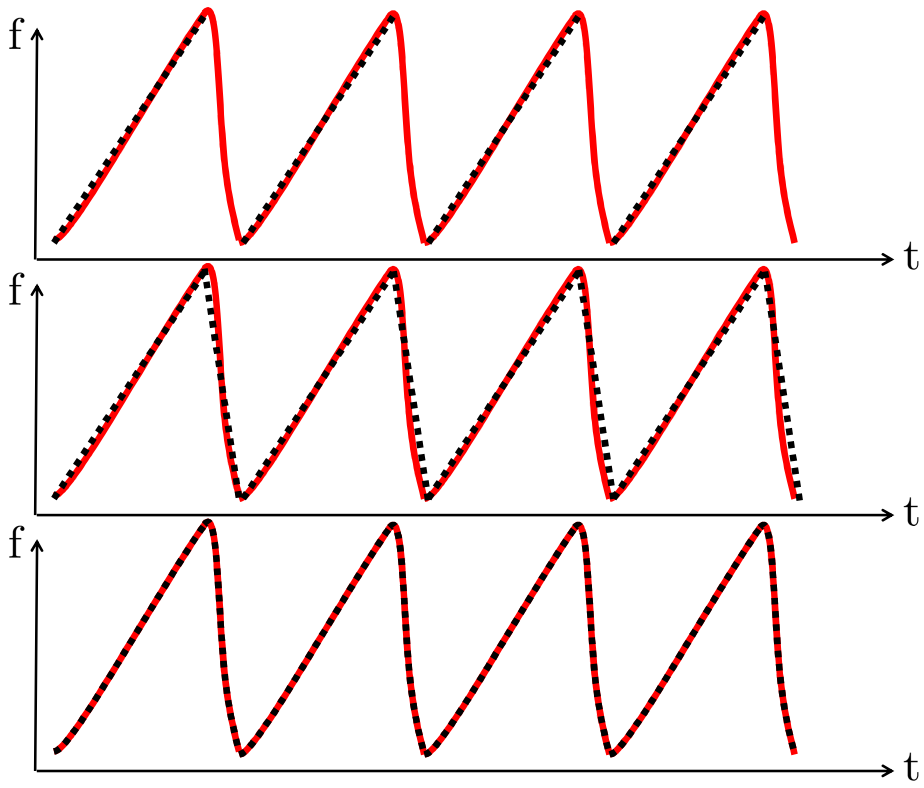

Figure 5.1: Possible frequency time-histories at different steps in the acquisition procedure. The top plot displays the frequency time-history resulting from the detection test's $\mathbf{x}_p$, the middle plot from the rough acquisition's $\mathbf{x}_1$, and the bottom plot from the fine acquisition's $\mathbf{x}$.

5.2 Rough State Acquisition

The rough acquisition procedure would ideally produce the state $\mathbf{x}_1$ that best fits the received data according to a yet-to-be-developed fit metric. The rough acquisition does not optimize every free element of $\mathbf{x}_1$ because that would be too computationally expensive. Instead, a suboptimal $\mathbf{x}_1$ will be computed using the output of the signal detection test, $\mathbf{x}_p$, as *a priori* information about some of the states in $\mathbf{x}$. This is conjectured to be only slightly suboptimal for most PPDs, and enables a significant reduction in computation time. This chapter's fit metric will yield a low fit error cost if the instantaneous frequency of the model's signal matches that of the received signal for the time duration of the fit interval. The evaluation of the frequency matching will be accomplished using FFTs. The carrier-to-noise density ratio, $\frac{C}{N_0}$, must be sufficiently large for this method to work. Several quantities must be developed before the fit metric can be presented.

The first quantity of interest is the FFT vector, $\mathbf{z}'_q$, computed using data batch number q, $\mathbf{y}_q$:

$$\mathbf{z}'_q\left(\mathbf{y}_q\right) = \begin{bmatrix} \mathbf{z}'_{q,1} \\ \vdots \\ \mathbf{z}'_{q,N_{FFT}} \end{bmatrix} \tag{5.1}$$

where N_{FFT} is the number of data points used in the FFT, and $\mathbf{z}'_{q,m}$ is the m^{th} element of the FFT vector. $\mathbf{z}'_q$ is assumed to be sorted so that $\mathbf{z}'_{q,1}$ corresponds to the frequency bin that is farthest below the mixing frequency, and $\mathbf{z}'_{q,N_{FFT}}$ corresponds to the frequency bin that is farthest above the mixing frequency. This

leads to the definition of the energy of the FFT vector, $\mathbf{z}_q$:

$$\mathbf{z}_q\left(\mathbf{y}_q\right) = \begin{bmatrix} \left(\mathbf{z}'_{q,1}\right)^H \left(\mathbf{z}'_{q,1}\right) \\ \vdots \\ \left(\mathbf{z}'_{q,N_{FFT}}\right)^H \left(\mathbf{z}'_{q,N_{FFT}}\right) \end{bmatrix} = \begin{bmatrix} \mathbf{z}_{q,1} \\ \vdots \\ \mathbf{z}_{q,N_{FFT}} \end{bmatrix} \tag{5.2}$$

where $(*)^H$ is the complex conjugate operator applied to the quantity $*$. Therefore, $\mathbf{z}_q\left(\mathbf{y}_q\right)$ is an N_{FFT}-by-1 vector of non-negative real values.

The next quantity of interest is b_q, the index of the FFT bin with the maximum energy over all $\mathbf{z}_{q,m}$ values:

$$b_q = \arg\max_m \left(\mathbf{z}_{q,m}\right) \tag{5.3}$$

thus b_q equals the index, m, of the FFT entry with the maximum amount of energy. This leads to the definition:

$$\Delta b_q = |\bar{b}_q - b_q| \tag{5.4}$$

where $|*|$ is the absolute value of the quantity $*$, b_q is the result of Eq. (5.3) applied to the FFT vector computed on the received data $\mathbf{y}_q$, and $\bar{b}_q$ is the result using the modeled data $\bar{\mathbf{y}}_q$. Recall that $\bar{\mathbf{y}}$ is a function of $\mathbf{x}_1$, the chirp state that allows nonzero entries on all states except c_j^u and c_j^d with $j > 1$.

When N_q sequential batches of data are considered, a vector of stacked FFT energy vectors, one for each batch of data, can be defined:

$$\mathbf{z} = \begin{bmatrix} \mathbf{z}_1 \\ \vdots \\ \mathbf{z}_{N_q} \end{bmatrix} \tag{5.5}$$

where $\mathbf{z}$ is the stacked vector using data from $\mathbf{y}$, and $\bar{\mathbf{z}}$ is the stacked vector using data from $\bar{\mathbf{y}}$. A corresponding vector $\Delta\mathbf{b}(\mathbf{x}_1, \mathbf{y})$ can be defined that has one entry for each FFT data batch:

$$\Delta\mathbf{b}(\mathbf{x}_1, \mathbf{y}) = \begin{bmatrix} \Delta b_1 \\ \vdots \\ \Delta b_{N_q} \end{bmatrix} \tag{5.6}$$

The entries of $\Delta\mathbf{b}$ are the magnitudes of the differences in the number of frequency bins between the maximum-energy FFT bin for the received and the modeled data. Every entry is an integer, but the entries could be multiplied by the frequency resolution, determined by N_{FFT} and f_s, to arrive at a frequency difference in units of Hz. This frequency difference is assumed to be the difference in the instantaneous frequencies of the received data and the modeled data, which is the quantity that this initialization procedure seeks to minimize. A cost function that uses $\Delta\mathbf{b}$ can thus be formed:

$$J_b(\mathbf{x}_1, \mathbf{y}) = \Delta\mathbf{b}(\mathbf{x}_1, \mathbf{y})^T \Delta\mathbf{b}(\mathbf{x}_1, \mathbf{y}) \tag{5.7}$$

where $(*)^T$ is the transpose of the quantity $*$.

Many different candidate values of $\mathbf{x}_1$ must be evaluated to determine the best fit to the real data. At least one full chirp period-worth of data should be used to ensure observability of T, and experience has shown that the use of several chirp periods' worth of data will improve the results. The results presented in this section assumed that no process noise entered during the acquisition interval. Additionally, too large a value for N_{FFT} will significantly violate the FFT's assumption of stationarity, and will attenuate the energy that will be accumulated in the FFT, which will degrade the algorithm's ability to estimate $\mathbf{x}_1$ accurately. The minimization of Eq. (5.7) will be difficult to accomplish with either a gradient-descent or a Newton-type method due to the discrete nature of

the entries in the cost function, e.g., the integer Δb_m terms. Therefore, Eq. (5.7) will be evaluated using a grid search. As mentioned previously, a grid search over all of the states in $\mathbf{x}_1$ that did not make use of any *a priori* information would provide the lowest cost solution to Eq. (5.7). Such a search would be extremely time consuming and would ignore the significant *a priori* information provided by the signal detection test. It will be shown that only 2 dimensions will need to be evaluated in a grid search if the *a priori* information is included, and that these two dimensions will have a very limited range of possible values. Therefore, in the remainder of this work it is assumed that $\mathbf{x}_1$ uses the *a priori* information from the detection.

A computationally efficient grid search for the determination of the $\mathbf{x}_1$ state that minimizes Eq. (5.7) subject to the *a priori* information of $\mathbf{x}_p$ is developed next. The cost function $J_b(\mathbf{x}_1, \mathbf{y})$ in Eq. (5.7) is independent of the initial phase θ_0 and the amplitude A. Therefore, it cannot be used to estimate these values. Values of θ_0 and A are needed, however, in order to calculate certain intermediate quantities. The value $\theta_0 = 0$ is chosen arbitrarily, and a value for A is chosen that is consistent with the expectation value of the noncoherent detection statistic γ_{nc}. There are four states that must still be initialized in $\mathbf{x}_1$: f_0, c_1^d, t^u , and t^d. Note that t_{L_1} is neither t^u nor t^d. However, t_{L_1} does provide a useful piece of information; the jammer's frequency has been estimated to cross through f_{L_1} at time t_{L_1}. Dimensionally, four unknown states plus the one piece of information provided by t_{L_1} and the one piece of information provided by the constraint that the frequency be the same at the beginning and end of the chirp period results in 2 unknown quantities.

The two uncertain dimensions that must be evaluated at many different points can be expressed in several ways, but this work considers both dimensions in terms of frequency. The first dimension is the frequency span of the

chirp, f_{span}, and the second dimension is the starting frequency, f_0. Figure 5.2 depicts possible frequency time-histories for given values of c_1^{u}, t_{L_1}, and T from $\mathbf{x}_{\text{p}}$. The top plot demonstrates three different possible f_{span} values, $f_{\text{span},1}$, $f_{\text{span},2}$, $f_{\text{span},3}$ and a fixed value of f_0. The bottom plot, on the other hand shows three different values of f_0, $f_{0,1}$, $f_{0,2}$, $f_{0,3}$ for a fixed value of f_{span}. Note how both plots start with the same upward-slopping chirp that has the same slope value c_1^{u} and the same intercept point f_{L_1} at t_{L_1}. Note, also, how all six frequency time-histories on the two plots have the same T. The ranges of the grid search dimensions are as follows. The maximum value for f_{span} is $c_1^{\text{u}}T$, and the minimum is close to zero, which corresponds to 100% of the chirp period being a ramp-up and 0% ramp-up. The maximum value of f_0 is f_{L_1}, and the minimum is $f_{\text{L}_1} - c_1^{\text{u}}T$.

The rough acquisition estimate of the first-order chirp state, $\mathbf{x}_1$, is the quantity that minimizes Eq. (5.7) via the above 2D grid-search. Typically 50–100 grid points have been used along each of these two axes, this represents an ad-hoc choice of spacing that seems reasonable, and it has produced many acceptable acquisitions.

5.3 Fine State Acquisition

The fine acquisition is accomplished through the use of a nonlinear square root information (SRI) form of the maximum likelihood estimator (MLE). The reader is assumed to be familiar with SRI MLEs, but more information can be found on SRI equations in [7] and MLEs in [5].

The MLE used an implementation of the Gauss-Newton method to minimize the following nonlinear cost function:

$$\text{J}_{\text{c}}\left(\mathbf{x},\mathbf{y}\right) = \langle \mathbf{R}_{\text{a}}^{-T}\left[\mathbf{z}\left(\mathbf{y}\right) - \bar{\mathbf{z}}\left(\mathbf{x}\right)\right]\rangle^{H}\langle \mathbf{R}_{\text{a}}^{-T}\left[\mathbf{z}\left(\mathbf{y}\right) - \bar{\mathbf{z}}\left(\mathbf{x}\right)\right]\rangle \tag{5.8}$$

where $\mathbf{R}_{\text{a}}$ is the square-root-covariance matrix that weights the errors. Recall

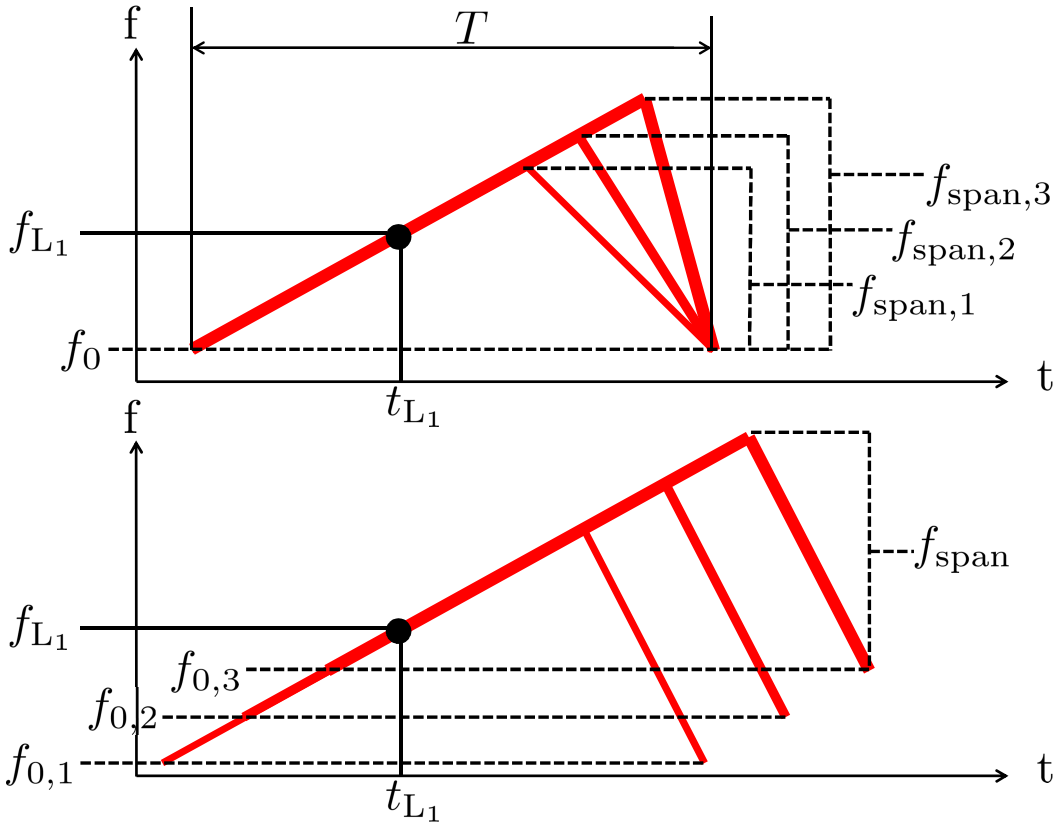

Figure 5.2: This work's two different initialization search parameters. The top plot shows three different possibilities for f_{span}, and the bottom plot shows three different possibilities for f_0.

that $\mathbf{z}(\mathbf{y})$ is the vector of measured energy spectra for N_{q} different FFT intervals, and $\bar{\mathbf{z}}(\mathbf{x})$ is the model's equivalent. Although, not mentioned previously, the FFTs contain some measurement noise, $\mathbf{w}$, that is assumed to behave as a Gaussian random variable vector with the following statistics:

$$\mathbf{w} \sim \mathcal{N}\left(2N_{\mathrm{FFT}}\sigma_{\nu}^{2}\mathbf{e}, \mathbf{R}_{\mathrm{a}}^{T}\mathbf{R}_{\mathrm{a}}\right) \tag{5.9}$$

where $\mathbf{e}$ is a column vector with all entries of 1, the term $2N_{\mathrm{FFT}}\sigma_{\nu}^{2}\mathbf{e}$ is the mean of $\mathbf{w}$, and $\mathbf{R}_{\mathrm{a}}^{T}\mathbf{R}_{\mathrm{a}}$ is its covariance. The details of the calculation of this covariance are omitted for the sake of brevity. The cost function of Eq. (5.8) has similarities to Eq. (5.7). Both attempt to match the real data and the model's simulation of the data, but $\mathrm{J_c}$ is more suited to nonlinear optimization using a Newton-type method.

The MLE-based fine state initialization process allows full frequency polynomial variation, i.e. it permits non-zero entries for the states c_j^{u} and c_j^{d} for all j. It will uses the first-order state from the rough initialization $\mathbf{x}_1$ as the initial state estimate for its nonlinear iterative solution with zero values filed in for c_j^{u} and c_j^{d} for $j > 1$. It should also be noted that the state θ_0 is unobservable in this batch estimation problem. Therefore, θ_0 has been arbitrarily set to 0. The state, $\mathbf{x}$, that minimizes the cost function of Eq. (5.8) is the output of the fine state initialization procedure.

5.4 Acquisition Results

The full acquisition algorithm developed in this chapter has been applied to the PPD data files that were used to create Figs. 2.7 and 3.1, and one data file collected in a field experiment. The results of the acquisition are presented in this section. Recall that Fig. 2.7 displays the output of a jammer that is modeled well by a first-order frequency polynomial, whereas the jammer used to

generate Fig. 3.1 is more accurately modeled by a higher-order polynomial. The PPD from the field experiment was also modeled well by a first-order frequency polynomial, but the data were recorded at a much lower bandwidth, 9 MHz.

Figure 5.3 contains two different normalized spectrum time-history plots, with one overlaid on top of the other, in the top graph, and the bottom graph uses vertical red lines to denote the mid-point of each FFT batch. The first spectrum time-history is generated from the real PPD data used to create Fig. 2.7. The second spectra is generated using the work's signal model and the final state estimate from the acquisition procedure described in the previous sections. The figure shows that the initial state estimate produces results that are nearly indistinguishable from the real data, hence, the figure appears to show just a single spectrum time-history. Note that the acquisition only operated on the first three full chirp periods. Therefore, the last two chirp periods in the figure show slight traces of divergence between the measured and modeled spectrum time-histories if one looks very closely.

Figure 5.4 is similar to Fig. 5.3, but it used the same data that were used to create Fig 3.1. The polynomial fit appears to be accurate for the frequency ramp-up, but the frequency span of the polynomial is slightly too small. The misfit is a result of the nonlinear nature of the measurement model and an incomplete search of the state space during the rough acquisition procedure. The state estimate from the rough initialization is not ideal, as it uses several assumptions and the incomplete *a priori* information from the signal detection algorithm. Therefore, the MLE's state estimate converges to a locally optimal state instead of the global optimum. This type of suboptimal frequency polynomial fit may occur for other PPDs with chirps that have higher-order variations, such as the PPD who's data created Figs. 3.1 and 5.4. The suboptimal fit is one of the unfortunate trade-offs that result from the adoption of the assumptions that reduce

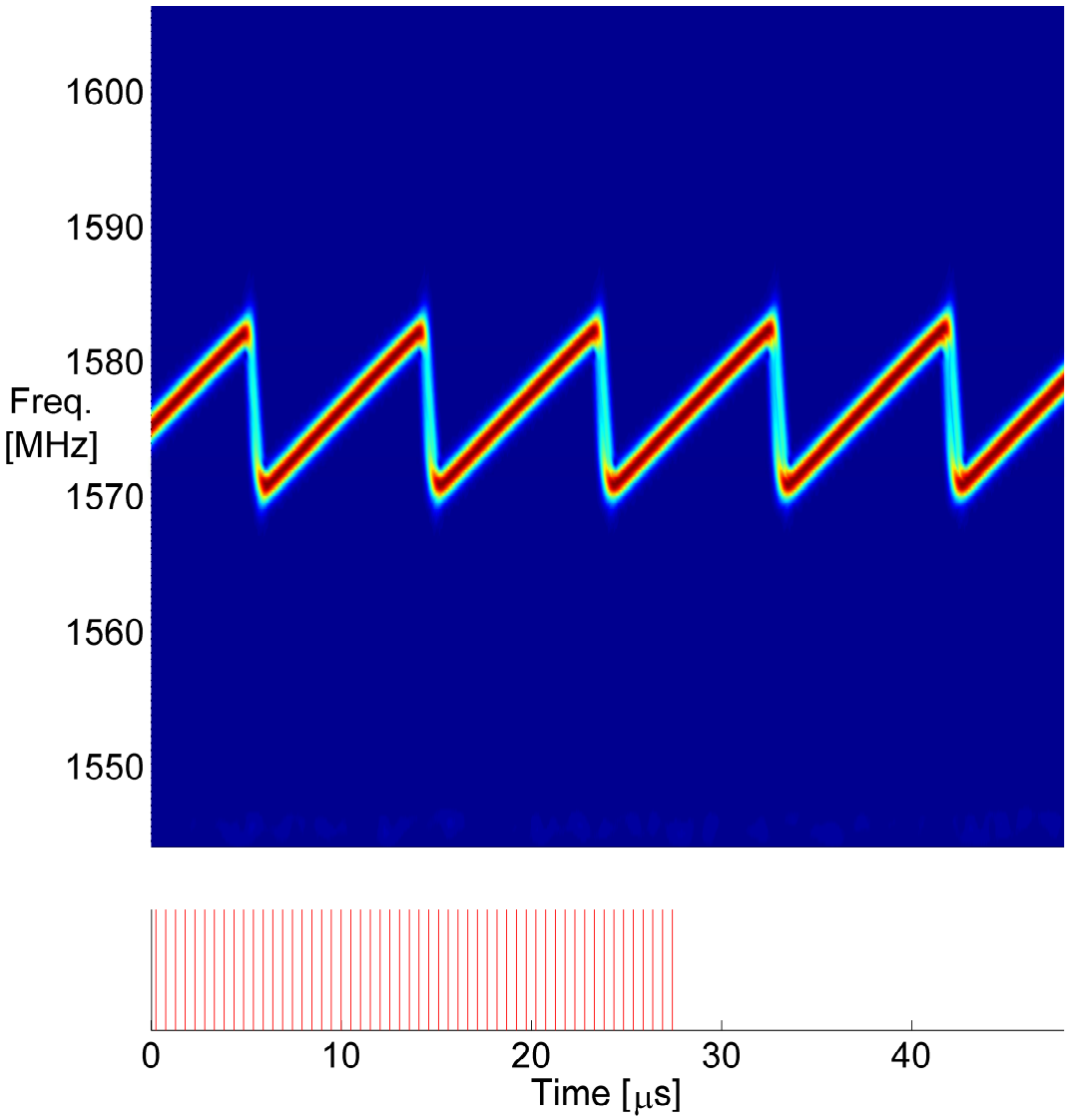

Figure 5.3: The initialized hypothesis jamming signal overlaid with the spectra of the real jamming signal. Laboratory data set 1.

the acquisition algorithm's computation time. Although not shown, the initial state estimate is still accurate enough for use in a Kalman filter signal tracking algorithm. Note that the frequency ramp-down is poorly estimated by the MLE for this PPD. Errors in the estimate of the frequency during the ramp-down will cause a smaller increase in the cost J_c then will errors in the estimate of the frequency during the ramp-up. The differing magnitudes of the cost increase is due to the mis-estimated frequencies is a result of the differing frequency ramp rates in the polynomials. The ramp-downs are much faster than the ramp-ups; so, less energy is accumulated in each of the FFTs of the ramp-down data versus the ramp-up data. Therefore, the MLE more heavily weights errors in the frequency ramp-ups.

Figure 5.5 plots the results for the data collected in the field. As before, the spectrum time-histories of the real data and the model's prediction are overlaid on top of each other. The initialization procedure works very well, despite the reduce sampling rate and the significant attenuation effects of the RF front-end.

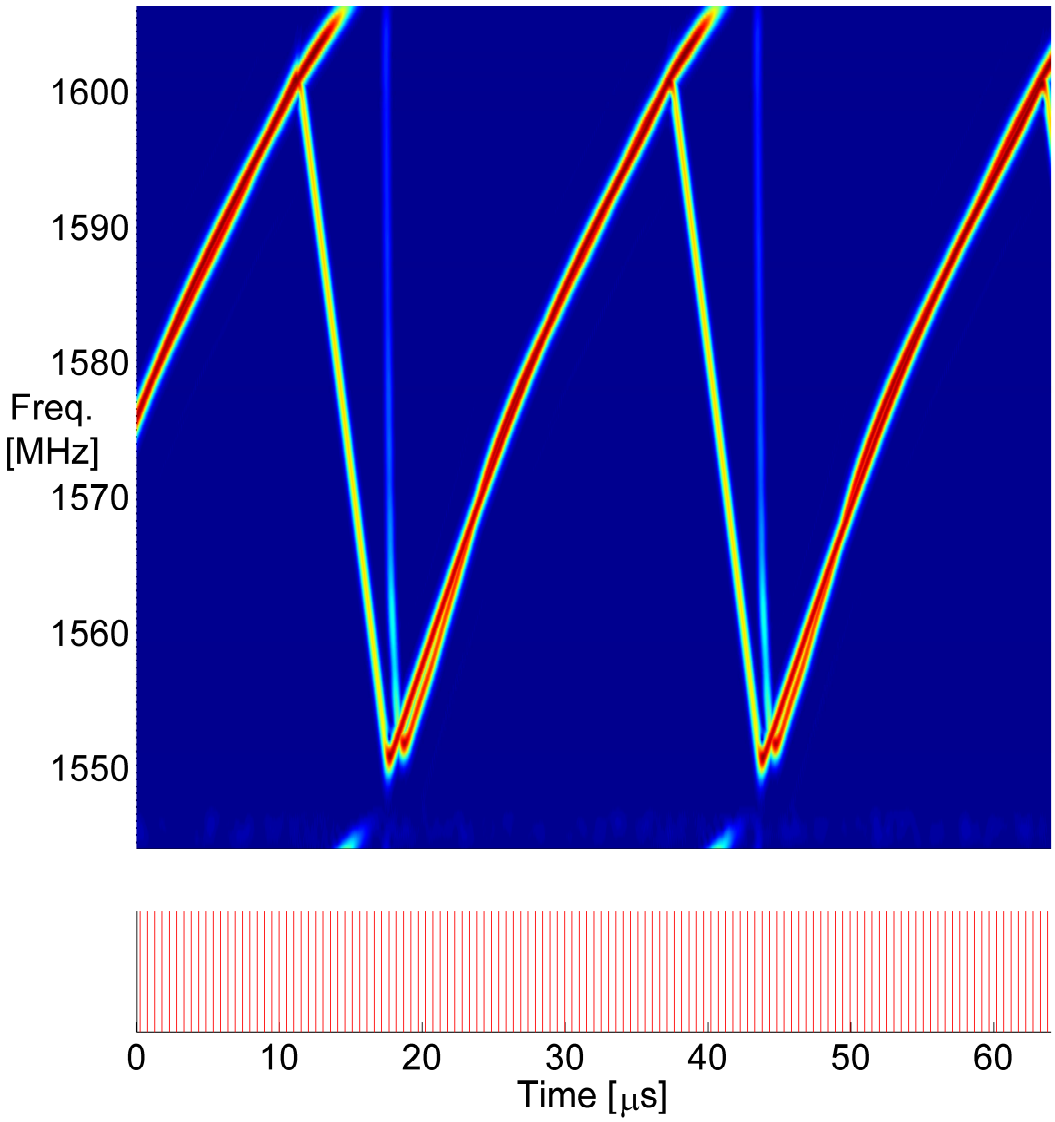

Figure 5.4: The initialized hypothesis jamming signal overlaid with the spectra of the real jamming signal. Laboratory data set 2.

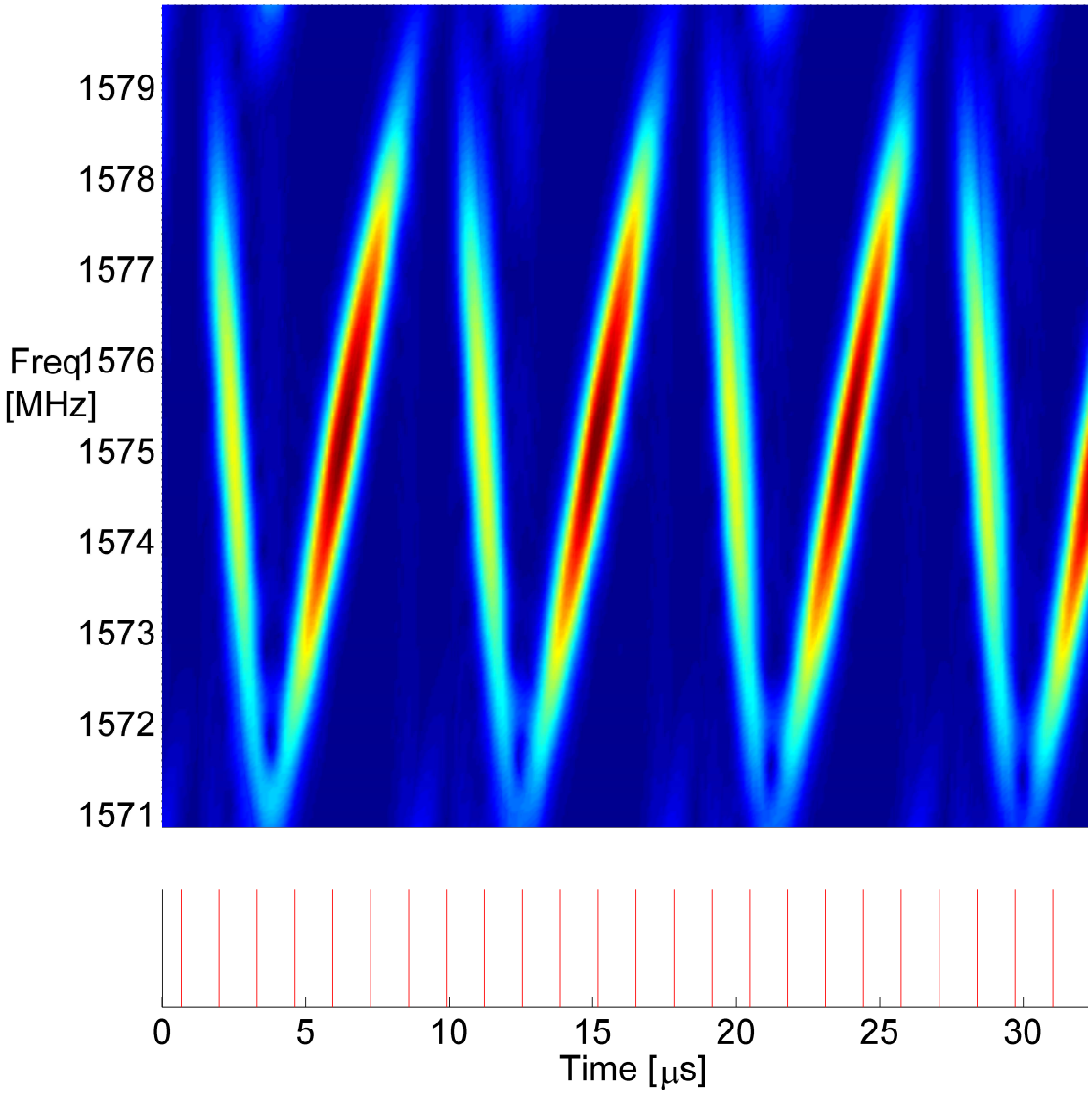

Figure 5.5: The initialized hypothesis jamming signal overlaid with the spectra of the real jamming signal. Field data set.

CHAPTER 6

SIGNAL TRACKING

6.1 Tracking Overview

This chapter is specifically concerned with the tracking of the chirp-style signals of PPDs. This chapter develops the measurement model and discusses the components of a PPD signal tracking Kalman filter. The multi-PPD case will also be considered. First, however, the previous work in this field will be discussed.

6.2 Background on Signal Tracking

There are many different kinds of chirp-style signals and many ways that these signals can be estimated. Additionally, while some methods seek to provide an estimate for every state in the signal model, other methods only consider how to estimate part of the state vector. A full survey of the topic is beyond the scope of this work, but several relevant references are provided and briefly discussed in the next paragraph.

Many authors have had success using Kalman filters to track chirp-style signals [24, 1, 18, 2, 19]. These methods typically use the raw RF data as their measurements, or they operate on the received signal in a sample-by-sample manner. Other authors have focused on different methods for estimating the instantaneous frequency of the chirp signals [8]. Some have used the Wigner distribution and clustering algorithms to track multiple chirp signals [14], while others have used specific minimum mean square error techniques, combined with the Choi-Williams time-frequency distribution, to track multiple linear/quadratic chirps [28]. The discrete chirp-Fourier transform has been applied to great effect on some chirp signals to estimate their chirp rate [57]. The ambiguity function

has been used extensively by the radar community [32, 55, 33, 45] and is suitable for application on both the standard chirp waveform and also on the chirp diverse waveform [52]. Other authors have had success using hidden Markov models [4], and the chirplet transform [31]. Integrated cubic phase functions and the dechirp method have also been used [54]. Some authors have passed the received signal through a collection of filters with known responses in order to determine the parameters of the chirp signal [46].

This work's signal tracking algorithm differs from the above works that also implemented Kalman filters in at least four distinct ways. First, it uses the energy in different FFT bins as its measurement model. Second, it uses a different state-space polynomial signal model for the PPD signals. Third, its Kalman filter architecture is different. This work uses a square-root implementation of the iterated extended Kalman filter for state estimation. Lastly, this work applies its developed algorithms on a number of real PPD signals, in both a laboratory and a field setting. Some of the PPDs have frequency behavior that is not modeled in other papers, and cannot be modeled with even the complicated chirp model used in this thesis. But results will still be presented for these PPDs. It should be noted, however, that some of the above signal tracking methods might provide similar results if they were to be applied to these PPD signals.

6.3 FFT-Based Single Jammer Measurement Model

This chapter will use the energy in a batch of FFTs computed on the sampled data as the measurements that drive its Kalman filter. This FFT batch data assimilation has desirable properties for chirp-style signal tracking. In this model, FFTs are effectively short-time-span accumulations at a set of frequencies that span the Nyquist range. The FFT algorithm is faster than using standard accu-

mulation techniques to compute the same quantities. They provide measures of the signal energy in every frequency bin within the Nyquist bounds. A measurement model that uses the energy in the FFT accumulations will have improved robustness to an incorrectly estimated initial phase state. The noise effects in the FFTs are effectively uncorrelated between frequency bins. Furthermore, FFT measurements can be generalized to the multi-PPD scenario in a straight-forward manner.

The development of this chapter's single-PPD measurements starts with the standard recipe for computing an FFT. The FFT measurement is then converted into the energy of the accumulation by multiplying that FFT by its complex conjugate. The corresponding measurement model is developed next. Then the Jacobian, the matrix of the partial derivatives of the energy model measurements with respect to the state vector elements, is developed.

The recipe for computing a single FFT measurement, z'_l, for frequency bin l is:

$$\begin{aligned} z'_l &= \sum_{n=0}^{N-1} w_n y_n e^{-\mathrm{i}2\pi \frac{ln}{N}} \quad \text{for} \quad l = 0...N-1 \\ &= I_l + (\mathrm{i}Q_l) \end{aligned} \tag{6.1}$$

where w_n is a user-defined window function such as the Hamming window, y_n is the RF sample at time t_n. For simplicity, the remainder of the derivation will assume that the FFTs are not windowed, e.g., $w_n = 1$. The terms I_l and Q_l are the in-phase and quadrature accumulations, respectively, for the frequency bin l. The FFT computed for frequency bin l from Eq. (6.1) can be converted to the energy in that bin. This leads to the definition of the FFT energy measurement vector, $\mathbf{z}$, which is the final measurement provided to the signal tracking Kalman

filter:

$$\mathbf{z} = \begin{bmatrix} I_0^2 + Q_0^2 \\ \vdots \\ I_{N-1}^2 + Q_{N-1}^2 \end{bmatrix} \tag{6.2}$$

The use of the energy in the FFTs will improve robustness to errors in the initial phase estimate. Unfortunately, this modification will also make the initial phase state, θ_0, unobservable. A functionally equivalent measurement model would use the absolute value of the FFT accumulations; the difference between the models is only the inclusion of a square-root operation. The results in this chapter make use of both models, but the derivation is provided only for the energy model.

Given the measurement recipe in Eqs. (6.1)–(6.2), a corresponding measurement model needs to be generated. The following form of the measurement model characterizes the relationship between the state vector $\mathbf{x}$, the measurement noise vector $\boldsymbol{\nu}' = \left[\nu'_0, ..., \nu'_{N-1}\right]^{\mathrm{T}}$, and the FFT energy vector $\mathbf{z}$. The model is developed by replacing y_n in Eq. (6.1) with $y_n(t_n; \mathbf{x}, f_{\mathrm{mix}}) + \nu'_n$ and carrying through the operations in Eqs. (6.1)–(6.2). The result of these calculations is a vector of modeled FFT energies for a given pair of vectors $\mathbf{x}$ and $\boldsymbol{\nu}'$:

$$\check{\mathbf{h}}(\mathbf{x}, \boldsymbol{\nu}') = \begin{bmatrix} \{I_{0,\mathrm{ideal}}(\mathbf{x}) + n_{0,I}(\boldsymbol{\nu}')\}^2 + \{Q_{0,\mathrm{ideal}}(\mathbf{x}) + n_{0,Q}(\boldsymbol{\nu}')\}^2 \\ \vdots \\ \{I_{N-1,\mathrm{ideal}}(\mathbf{x}) + n_{N-1,I}(\boldsymbol{\nu}')\}^2 + \{Q_{N-1,\mathrm{ideal}}(\mathbf{x}) + n_{N-1,Q}(\boldsymbol{\nu}')\}^2 \end{bmatrix} \tag{6.3}$$

where $I_{l,\mathrm{ideal}}(\mathbf{x})$ and $Q_{l,\mathrm{ideal}}(\mathbf{x})$ are the ideal, noise-free accumulations, and $n_{l,I}$ and $n_{l,Q}$ are the resulting accumulations if only noise were present in the received signal. The noise terms $n_{l,I}$ and $n_{l,Q}$ have the following Gaussian statistics:

$$n_{l,I}(\boldsymbol{\nu}') \text{ or } n_{l,Q}(\boldsymbol{\nu}') \sim \mathcal{N}\left(0, N\sigma_\nu^2\right) \tag{6.4}$$

and they are uncorrelated with each other and with the terms for different FFT index values $q \neq l$.

If there were no noise in the accumulations and if the state estimate were perfect, then $I_l = I_{l,\text{ideal}}(\mathbf{x})$ and $Q_l = Q_{l,\text{ideal}}(\mathbf{x})$; the model would match the measurements $\breve{\mathbf{h}}(\mathbf{x}, \mathbf{0}) = \mathbf{z}$. These ideal accumulations could be computed using Eq. (6.1), with the noise-free y_n substituted for y_n. The above model can be rewritten to separate the terms that are not functionally dependent on the noise, $\mathbf{h}(\mathbf{x})$, and those that are, $\mathbf{w}$:

$$\begin{aligned}\mathbf{h}(\mathbf{x}) + \mathbf{w} &= \breve{\mathbf{h}}(\mathbf{x}, \boldsymbol{\nu}') \\ &= \begin{bmatrix} I^2_{0,\text{ideal}}(\mathbf{x}) + Q^2_{0,\text{ideal}}(\mathbf{x}) \\ \vdots \\ I^2_{N-1,\text{ideal}}(\mathbf{x}) + Q^2_{N-1,\text{ideal}}(\mathbf{x}) \end{bmatrix} + \mathbf{w}\end{aligned} \tag{6.5}$$

where $\mathbf{w}$ is the N-by-1 stacked vector of measurement noise random variables for each FFT bin l, w_{l+1}. This $(l+1)^{\text{st}}$ element of $\mathbf{w}$ is defined as:

$$\mathrm{w}_{l+1} = 2\left[I_{l,\text{ideal}}(\mathbf{x}) n_{l,I}(\boldsymbol{\nu}') + Q_{l,\text{ideal}}(\mathbf{x}) n_{l,Q}(\boldsymbol{\nu}')\right] + \left[n^2_{l,I}(\boldsymbol{\nu}') + n^2_{l,Q}(\boldsymbol{\nu}')\right] \text{ for } l = 0...N-1 \tag{6.6}$$

To simplify the analysis, the measurement model's accumulation noise vector $\mathbf{w}$ is approximated as being Gaussian. Its statistics are:

$$\mathbf{w} \sim \mathcal{N}\{\bar{\mathbf{w}}(\boldsymbol{\nu}'), \mathbf{R}(\mathbf{x}, \boldsymbol{\nu}')\} \tag{6.7}$$

The term $\bar{\mathbf{w}}(\boldsymbol{\nu}')$ is the expected value of the noise in Eq. (6.6):

$$\bar{\mathbf{w}}(\boldsymbol{\nu}') = 2N\sigma^2_\nu \, \mathbf{e} \tag{6.8}$$

where $\mathbf{e}$ is a column vector with only entries of 1, and σ_ν is taken from the statistics of the measurement noise ν' from Eqs. (3.27) and (3.33). The term $\mathbf{R}(\mathbf{x}, \boldsymbol{\nu}')$ is the covariance of the noise. It is diagonal with diagonal elements $\mathbf{R}_{l+1,l+1}$:

$$\mathbf{R}_{l+1,l+1}(\mathbf{x}, \boldsymbol{\nu}') = 4N\sigma^2_\nu \left[I^2_{l,\text{ideal}}(\mathbf{x}) + Q^2_{l,\text{ideal}}(\mathbf{x})\right] + 4N^2\sigma^4_\nu \quad \text{for} \quad l = 0...N-1 \tag{6.9}$$

Because of its dependence on $\mathbf{x}$ the EKF that uses $\mathbf{R}(\mathbf{x}, \nu')$ will need to recompute it at each measurement update interval.

This measurement model has one additional, non-standard component that arises due to the nature of the accumulation computations. Standard Kalman filters compute their expected measurements using the state vector that is the output of the expected propagation of the dynamics model in Eq. (3.5), commonly denoted $\bar{\mathbf{x}}_{k+1}$. However, accumulation-based measurement models compute their expected measurements using the state vector that applies prior to propagation, $\mathbf{x}_k$. This state vector is used because the accumulations sum RF samples over the measurement interval that starts at time t_k and ends at time t_{k+1}. Therefore, the measurement model must use the state, $\mathbf{x}_k$, at the start of the accumulation interval, time t_k. This is a common technique, and a more thorough discussion of accumulation-based measurement models can be found in [13]. The resulting Kalman filter measurement model equation that is used to update the state vector at the interval that ends at time t_{k+1} is:

$$\mathbf{z}_{k+1} = \mathbf{h}(\mathbf{x}_k) + \mathbf{w}_{k+1} = \begin{bmatrix} I^2_{0,\text{ideal}}(\mathbf{x}_k) + Q^2_{0,\text{ideal}}(\mathbf{x}_k) \\ \vdots \\ I^2_{N-1,\text{ideal}}(\mathbf{x}_k) + Q^2_{N-1,\text{ideal}}(\mathbf{x}_k) \end{bmatrix} + \mathbf{w}_{k+1} \tag{6.10}$$

where the discrete time indices k and $k+1$ in the above equation correspond to those used in Eq. (3.5), $\mathbf{x}_{k+1} = \mathbf{\Phi}(t_{k+1}, t_k; \mathbf{x}_k)\,\mathbf{x}_k + \mathbf{\Gamma}(t_{k+1}, t_k; \mathbf{x}_k)\,\mathbf{v}_k$.

The measurement model of Eq. (6.10) is nonlinear, and thus a nonlinear Kalman filter must be implemented to estimate the state vector $\mathbf{x}$. In the remainder of this work, it is assumed that the EKF is used to track the PPD signals. EKFs use Taylor series expansions to linearly approximate the nonlinear models in a region about the current state and noise vector estimates. The second term in the Taylor series uses the Jacobian matrix $\mathbf{H}$. This is the matrix of partial derivatives of the measurement model vector with respect to the state

vector. The row of the matrix $\mathbf{H}$ that corresponds to frequency bin l, denoted $\mathbf{H}_{l+1}$, is:

$$\begin{aligned}\mathbf{H}_{l+1} &= \frac{\partial}{\partial \mathbf{x}} \mathrm{h}_{l+1}(\mathbf{x}) \\ &= 2\left[I_{l,\mathrm{ideal}}(\mathbf{x}) \frac{\partial I_{l,\mathrm{ideal}}(\mathbf{x})}{\partial \mathbf{x}} + Q_{l,\mathrm{ideal}}(\mathbf{x}) \frac{\partial Q_{l,\mathrm{ideal}}(\mathbf{x})}{\partial \mathbf{x}} \right]\end{aligned} \tag{6.11}$$

where $\frac{\partial I_{l,\mathrm{ideal}}(\mathbf{x})}{\partial \mathbf{x}}$ is the partial derivative of the noise-free in-phase accumulation model with respect to the state vector, and $\frac{\partial Q_{l,\mathrm{ideal}}(\mathbf{x})}{\partial \mathbf{x}}$ is defined similarly for the quadrature term. The two partial derivatives are evaluated at the current state estimate of $\mathbf{x}$. Recall that the noise term w_{l+1} is defined in Eq. (6.6) is dependent on the state estimate. However, the model of Eq. (6.10) suppresses this dependence. Therefore, the Jacobian matrix of Eq. (6.11) is only an approximation, but it is typically valid because the Taylor series is taken about the *a priori* noise $\boldsymbol{\nu}' = \mathbf{0}$, which causes the Jacobian of $\mathbf{w}_k$ with respect to $\mathbf{x}_k$ to be zero.

The term $\frac{\partial I_{l,\mathrm{ideal}}(\mathbf{x})}{\partial \mathbf{x}}$ is defined for each state element x_p as:

$$\frac{\partial I_{l,\mathrm{ideal}}(\mathbf{x})}{\partial x_p} = \frac{I_{l,\mathrm{ideal}}(\mathbf{x})}{A} \qquad \text{if } x_p \text{ is A} \tag{6.12A}$$

$$\frac{\partial I_{l,\mathrm{ideal}}(\mathbf{x})}{\partial x_p} = Re\left(\sum_{n=0}^{N-1} e^{\mathrm{i}2\pi\left(\theta(t_n;\mathbf{x}) - f_{\mathrm{mix}} t_n - \frac{ln}{N}\right)} \mathrm{i}2\pi \frac{\partial \theta(t_n;\mathbf{x})}{\partial x_p} \right) \qquad \text{if } x_p \text{ is any element not A} \tag{6.12B}$$

The operator $Re(*)$ is the real part of the quantity $*$. Equation (6.12B) can be evaluated by applying the partial derivative operator to Eq. (3.4) if the ramp mode does not change during the accumulation interval. If multiple modes are present, then the formula for $\theta(t_n;\mathbf{x})$ becomes more complicated, and its explicit partial derivative is omitted for the sake of brevity. The formula for $\frac{\partial Q_{l,\mathrm{ideal}}(\mathbf{x})}{\partial \mathbf{x}}$ is very similar to the above equation, but $I_{l,\mathrm{ideal}}$ is replaced by $Q_{l,\mathrm{ideal}}$ and the bottom line uses the imaginary part instead of the real part. Note, the calculations

in Eq. (6.12B) and in the corresponding equation for $\frac{\partial Q_{l,\text{ideal}}(\mathbf{x})}{\partial x_p}$ constitute an FFT of $(e^{\mathrm{i}2\pi(\theta(t_n;\mathbf{x})-f_{\text{mix}}t_n)}\mathrm{i}2\pi\frac{\partial\theta(t_n;\mathbf{x})}{\partial x_p})$. Therefore, an FFT implementation can speed the calculation of these partial derivatives.

6.4 FFT-Based Multi-Jammer Measurement Model

The single PPD measurement model of the previous section must be modified if multiple PPDs are present. Fortunately, the multi-jammer FFT-based measurement recipes are the same as the single jammer scenario from Eq. (6.1); the FFTs are computed using raw data.

The derivation of the multi-PPD measurement model parallels that of the single-PPD model; the measurement model will be presented and then the Jacobian matrix will be presented. The primary difference is that the multi-PPD measurement model uses the multi-PPD y_n model of Eq. (3.28), instead of the single-PPD y_n model of Eq. (3.25), in Eq. (6.1). Fortunately, the FFT is a linear operator that distributes itself amongst the incoming signals:

$$\mathbf{h}\left(\underline{\mathbf{x}}\right)+\mathbf{w}=\begin{bmatrix}\{\sum_{m=1}^{N_\text{J}}I_{0,\text{ideal}}(\mathbf{x}^m)\}^2+\{\sum_{m=1}^{N_\text{J}}Q_{0,\text{ideal}}(\mathbf{x}^m)\}^2\\ \vdots\\ \{\sum_{m=1}^{N_\text{J}}I_{N-1,\text{ideal}}(\mathbf{x}^m)\}^2+\{\sum_{m=1}^{N_\text{J}}Q_{N-1,\text{ideal}}(\mathbf{x}^m)\}^2\end{bmatrix}+\mathbf{w} \tag{6.13}$$

where the superscript ^{m} terms are PPD indices and not exponents. Recall that $\mathbf{x}^m$ is the subset of elements of $\underline{\mathbf{x}}$ that applies to the m^{th} PPD. The noise term $\mathbf{w}$ is defined as follows for the row corresponding to frequency bin l, w_{l+1}:

$$\mathrm{w}_{l+1}=2\left[\{\sum_{m=1}^{N_\text{J}}I_{l,\text{ideal}}(\mathbf{x}^m)\}n_{l,I}(\boldsymbol{\nu}')+\{\sum_{m=1}^{N_\text{J}}Q_{l,\text{ideal}}(\mathbf{x}^m)\}n_{l,Q}(\boldsymbol{\nu}')\right]+\left[n_{l,I}^2(\boldsymbol{\nu}')+n_{l,Q}^2(\boldsymbol{\nu}')\right] \tag{6.14}$$

The measurement noise is very similar to that in the previous section. The noise is still approximated as being a Gaussian random variable with the same expected value $\bar{\mathbf{w}}$ from Eq. (6.20). The diagonal entries of the covariance matrix

change to:

$$\mathbf{R}_{l+1,l+1}(\mathbf{x},\boldsymbol{\nu}') = 4N\sigma_\nu^2\left[\{\sum_{m=1}^{N_J} I_{l,\text{ideal}}(\mathbf{x}^m)\}^2 + \{\sum_{m=1}^{N_J} Q_{l,\text{ideal}}(\mathbf{x}^m)\}^2\right] + 4N^2\sigma_\nu^4 \tag{6.15}$$

The multi-jammer measurement model will use the same pre-propagation state vector, $\mathbf{x}_k$, that was used in Eq. (6.10) to compute the accumulation measurements.

The measurement model is still nonlinear, and it is assumed that an EKF is used to estimate the state vector $\underline{\mathbf{x}}$. The multi-jammer Jacobian matrix, $\underline{\mathbf{H}}$, is similar to Eq. (6.11), and its $(l+1)^{\text{st}}$ row, corresponding to frequency bin l is:

$$\begin{aligned}\underline{\mathbf{H}}_{l+1} =& \frac{\partial}{\partial \underline{\mathbf{x}}} \mathrm{h}_{l+1}\left(\underline{\mathbf{x}}\right) \\ =& 2\{\sum_{m=1}^{N_J} I_{l,\text{ideal}}(\mathbf{x}^m)\}\left[\frac{\partial I_{l,\text{ideal}}(\mathbf{x}^1)}{\partial \mathbf{x}^1},\ldots,\frac{\partial I_{l,\text{ideal}}(\mathbf{x}^{N_J})}{\partial \mathbf{x}^{N_J}}\right] \\ &+2\{\sum_{m=1}^{N_J} Q_{l,\text{ideal}}(\mathbf{x}^m)\}\left[\frac{\partial Q_{l,\text{ideal}}(\mathbf{x}^1)}{\partial \mathbf{x}^1},\ldots,\frac{\partial Q_{l,\text{ideal}}(\mathbf{x}^{N_J})}{\partial \mathbf{x}^{N_J}}\right]\end{aligned} \tag{6.16}$$

6.5 Multi-Jammer Signal Interference

One additional algorithmic modification is made to the proposed Kalman filter. The modification is the inclusion of a relative phase parameter that is optimized at each measurement update interval of the Kalman filter. This change is necessitated by the interference effects resulting from multiple sinusoidal signals. The signals of two jammers can constructively and destructively interfere with each other at the signal reception point. The type and extent of the interference is a function of the relative phase of the signals. Fig. 6.1 was created using a multi-PPD data file and shows both types of interference. The interference of the two signals in Fig. 6.1 is most pronounced when the frequencies are similar. Note how on the left side of the plot the two PPD signals have ramp-up sections that over-lap. During these overlaps the maximum FFT power increases and

fades at successive times in the typical beat pattern produced by nearly identical frequencies.

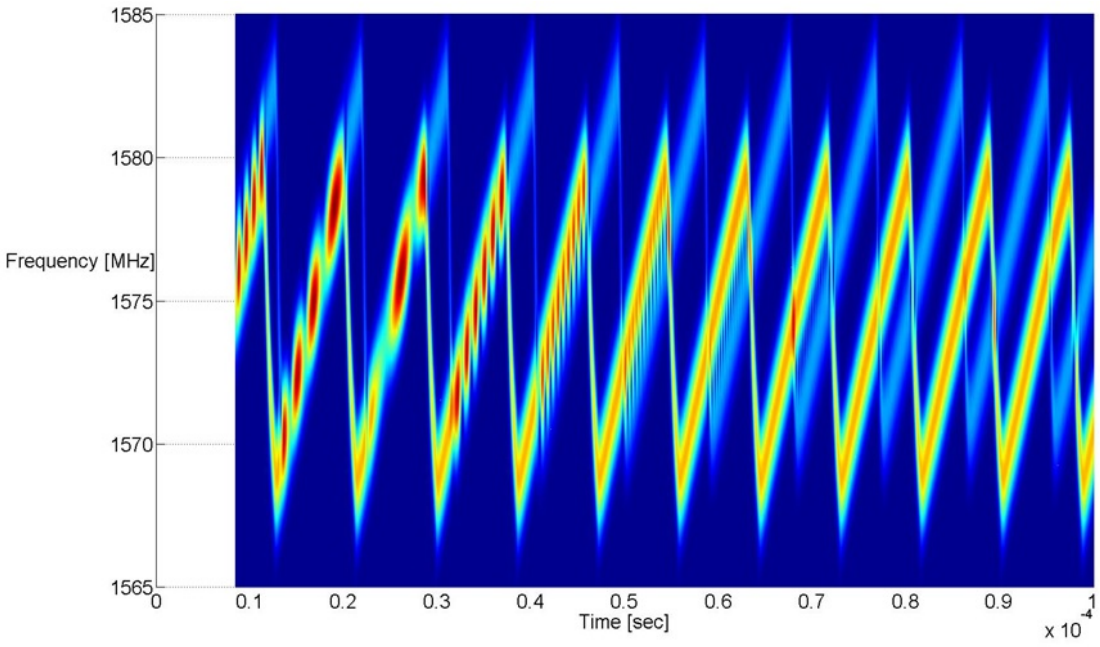

Figure 6.1: Spectra of two combined PPD laboratory data files.

The relative phase of the PPDs must be accounted for in the measurement model, otherwise, the measurement model will not be able to emulate the actual FFT-based measurements computed using the raw data. The approach taken in this work is to optimally fit the phase state, θ_0, to the data for every PPD at every measurement update interval. As mentioned previously, θ_0 is unobservable with the energy of the FFTs used as the measurement model. However, when multiple PPDs are present, the relative phase of the jammers is observable. There will be $N_J - 1$ phase parameters that must be estimated; θ_0 for the first PPD is arbitrarily set to 0.

A brute-force search is used to estimate the θ_0 value for each of the PPDs that will optimally match the FFT-based measurements in $\mathbf{z}$ and the multi-PPD model's predicted $\mathbf{z}$ vector. The phase is assumed to be uniformly distributed over the interval of 0–1 cycles. Therefore, each PPD's θ_0 state (except for the

first) is evaluated at multiple values spaced evenly in the range of 0–1 cycles. The search scales as $N_{\text{rel}}^{N_J-1}$, where N_{rel} is the number of θ_0 evaluation points for each of the $N_J - 1$ dimensions. Experience has shown that a reasonable value for N_{rel} is 20. The optimal θ_0 values are the ones that minimize the following square-root negative log-likelihood form of a maximum likelihood cost function for a single measurement interval:

$$J\left(\theta_0^2, \ldots, \theta_0^{N_J}\right) = \left[\mathbf{R_a}^{-T}\{\mathbf{z} - \mathbf{h}\left(\underline{\mathbf{x}}\langle\theta_0^2, \ldots, \theta_0^{N_J}\rangle\right)\}\right]^T \left[\mathbf{R_a}^{-T}\{\mathbf{z} - \mathbf{h}\left(\underline{\mathbf{x}}\langle\theta_0^2, \ldots, \theta_0^{N_J}\rangle\right)\}\right] \quad (6.17)$$

where $\mathbf{x}\langle\theta_0^2, \ldots, \theta_0^{N_J}\rangle$ is the multi-PPD state vector with variable initial phase values for PPDs 2–N_J, but with the values of all other states fixed at their current Kalman filter estimates. The term $\mathbf{R_a}^{-T}$ is the Cholesky factorization of the inverse and transpose of the measurement noise covariance matrix $\mathbf{R}$ that is defined in Eq. (6.21):

$$\mathbf{R} = \mathbf{R}_a^T \mathbf{R}_a \quad (6.18)$$

6.6 Practical Considerations

One practical issue regarding the implementation of the developed Kalman filter signal tracking algorithm is discussed here: RF filtering.

The RF filters in the front ends (FEs) of most data acquisition systems distort the received signal in some way. Often, special-purpose RF equipment is designed so that the effects of the RF filters are negligible for the desired task. However, live data were collected to validate this work's developed algorithms using general-purpose RF equipment. The FE of this equipment has a significant attenuation that is dependent on the received signal's frequency.

The FE's RF filter shape must typically be determined before the filtering effects can be fully addressed. If an off-line determination of the filter shape is

not possible, then the signals of the PPDs can be used to determine the filter shape. The chirp structure of the PPD signal is effectively a single tone that is swept across many different frequencies. The amplitude of the incoming tone will change in response to the filter shape. The filter's attenuation characteristics for the relevant frequency range can be determined using a batch of FFTs computed on data that span at least one chirp period. The FFTs can be converted to a magnitude value using the absolute value operator, and then the magnitudes of each frequency bin can be normalized by the maximum magnitude FFT accumulation for that batch. The resulting magnitude versus FFT frequency bin number provides a discrete set of attenuation values for an incoming signal at the corresponding frequencies. The attenuation can then be incorporated into the FFT model of the measurement and measurement noise in a straight-forward manner. The method used in this work is shown below for the single-PPD measurement model:

$$\mathbf{z}_{k+1} = \mathbf{h}\left(\mathbf{a}; \mathbf{x}_k\right) + \mathbf{w}_{k+1}(\mathbf{a}) = \begin{bmatrix} a_0^2\{I_{0,\text{ideal}}^2(\mathbf{x}_k) + Q_{0,\text{ideal}}^2(\mathbf{x}_k)\} \\ \vdots \\ a_{N-1}^2\{I_{N-1,\text{ideal}}^2(\mathbf{x}_k) + Q_{N-1,\text{ideal}}^2(\mathbf{x}_k)\} \end{bmatrix} + \begin{bmatrix} a_0^2 w_1 \\ \vdots \\ a_{N-1}^2 w_N \end{bmatrix} \tag{6.19}$$

where $\mathbf{a}$ is the N-by-1 parameter vector whose elements are the attenuation factors a_l for FFT bins $l = 0...N-1$. The noise statistics are still Gaussian, but they have been modified to include the attenuation factors:

$$\bar{\mathbf{w}}(\boldsymbol{\nu}') = 2N\sigma_\nu^2\, \mathbf{a}_2 \tag{6.20}$$

where $\mathbf{a}_2$ is the normal $\mathbf{a}$ vector, but each of its elements have been squared. The diagonal element of the covariance matrix $\mathbf{R}$ for frequency bin l is:

$$\mathbf{R}_{l+1,l+1}(\mathbf{x}, \boldsymbol{\nu}') = a_l^4\{4N\sigma_\nu^2\left[I_{l,\text{ideal}}^2(\mathbf{x}) + Q_{l,\text{ideal}}^2(\mathbf{x})\right] + 4N^2\sigma_\nu^4\} \quad \text{for} \quad l = 0...N-1 \tag{6.21}$$

There is a corresponding model for the multi-PPD attenuation factors, but that has been omitted for the sake of brevity. This simple RF filter attenuation estimate appears to be sufficient for a benign attenuation condition, but a more rigorous filter shape estimation method might provide better results for some attenuation conditions.

6.7 Signal Tracking Results

The Kalman filter signal tracking algorithm developed in this chapter uses the polynomial signal state, dynamics model, and FFT-based measurement model discussed earlier. The filter's initialization uses the method from Chapter 5. The Kalman filter is tested using the real-world data who's collection were discussed in Chapter 2. The presented results have been generated using a Square Root Information (SRI) implementation of an Iterated Extended Kalman filter (IKF). The reader is assumed to be familiar with this type of filter, but more information on SRI implementations can be found in [7], and more information on Kalman filters is presented in [5]. Effectively, the EKF linearizes its nonlinear equations around the current state estimate using first-order Taylor series expansions; it then executes the standard Kalman filter equations. The SRI implementation is a more numerically stable form of the standard Kalman filter.

This section is subdivided into four subsections. The first subsection provides results of the proposed signal tracking algorithm applied to three different PPD data files collected in a laboratory setting. The tracking algorithm is shown to work well on all three data files. The second subsection provides results of the proposed signal tracker when applied to a PPD from a field test, and it is shown to track the data well for a high carrier-to-noise density ratio when the PPD is close to the receiver station and for a low carrier-to-noise density ratio

when the PPD is approximately 1.8 kilometers distant from the receiver station. The third subsection considers one laboratory data file that contains the signals of two different PPDs, and the proposed filter is shown to be able to track both signals simultaneously. Unfortunately, the reliability of the signal tracking is weak and is found to be very sensitive to the filter's initial conditions. The fourth subsection considers two PPD signals in a field experiment, where the dual PPD tracking algorithm fails. The issues that cause the proposed signal tracking algorithm to fail are discussed. The results of the first subsection use the energy-based FFT measurement model, and the rest use an absolute value-based FFT measurement model that replaces the original elements of the $\mathbf{z}$ vector with their square-roots. It also modifies the $\mathbf{h}(\mathbf{x})$ measurement model and the $\mathbf{w}$ measurement noise definition accordingly. Note, however, that the non-zero mean measurement noise $\bar{\mathbf{w}}$ has been neglected in some of the results involving FFT absolute values, which will bias the estimates of the amplitude state A.

6.7.1 Tracking Results for a Single Jammer: Laboratory

The Kalman filter signal tracking algorithm is first applied to three different models of PPDs using data collected in a laboratory environment. They are presented in the order from the most similar to a canonical first-order linear chirp to the least like a first-order linear chirp. The difficulty of tracking the signals increases in the same order, i.e., the less that the PPD signal resembles a canonical first-order linear chirp the more difficult it is to track using the developed algorithm. The increase in difficulty is due to numerical issues and the mismatch between the behavior of the real signal and the model of the signal, particularly for the third PPD.

The results of the signal tracking algorithm are shown in Figs. 6.2, 6.3,

and 6.4. They display the frequency power spectra of the raw received signal, with time on the x-axis and frequency on the y-axis. The Kalman filter's frequency estimate is displayed in green on top of the spectra. The results in this subsection used a rough state initialization that assumed a first-order frequency polynomial signal state, as opposed to the full initialization procedure outlined in Chapter 5. Only the rough initialization procedure was used so that the convergence properties of the Kalman filter could be displayed, particularly for the second and third PPDs that significantly deviate from the canonical chirp form. The full acquisition procedure of Chapter 5 would have improved the convergence time of the following results. The displayed results are from the state estimates after each chirp is complete, i.e., just before the mode switch either from ramp-up to ramp-down, or vice versa. Therefore, these results are smoothed over each mode. Given that the longest mode lasts less than 30 μs, this slight non-causality does not give rise to any significant processing lag when using the Kalman filter outputs in down-stream calculations such as geolocation.

The PPD used to create Fig. 6.2 was one of the more benign PPDs considered in [35]. The filter is able to track the jammer's frequency state quite well.

The PPD used to create Fig. 6.3 was a more complicated PPD than that considered in Fig. 6.2. The filter is able to track the jammer's frequency state even though it has clear non-first-order frequency polynomial behavior.

The PPD used to create Fig. 6.4 was the least canonical PPD from [35]. The filter is able to approximately track the jammer's frequency state even though it is nonrepeating and has some nearly instantaneous jumps in frequency. The Kalman filter's state estimate will not perfectly reproduce the data recorded from this jammer because it cannot emulate the instantaneous frequency jumps. The filter instead assumes a large degree of process noise and creates the best possible frequency polynomial approximation to the data. Fortunately, this was

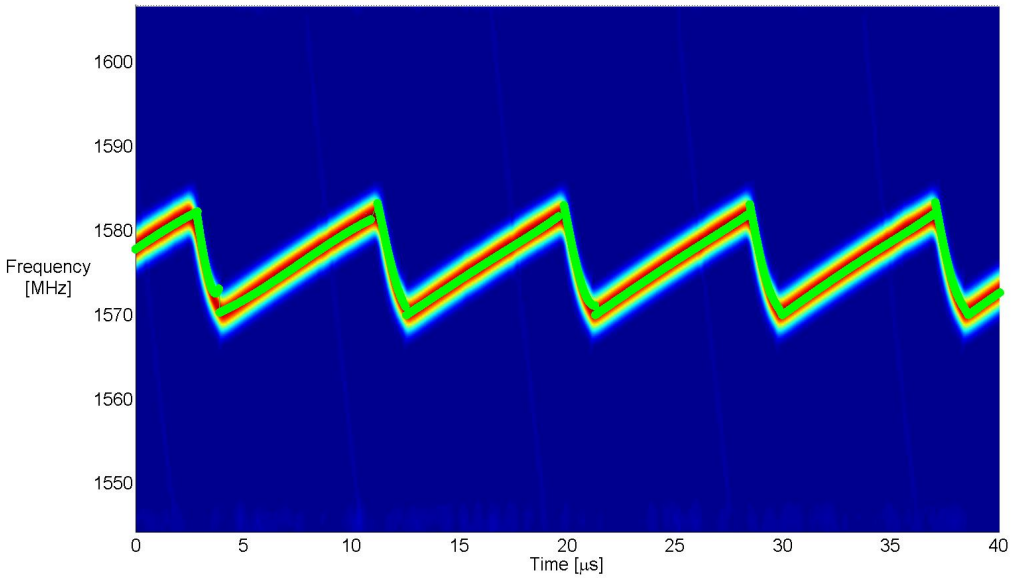

Figure 6.2: Frequency power spectra and estimated frequency of the Kalman filter (green curve) for the easiest PPD to track using the developed algorithm.

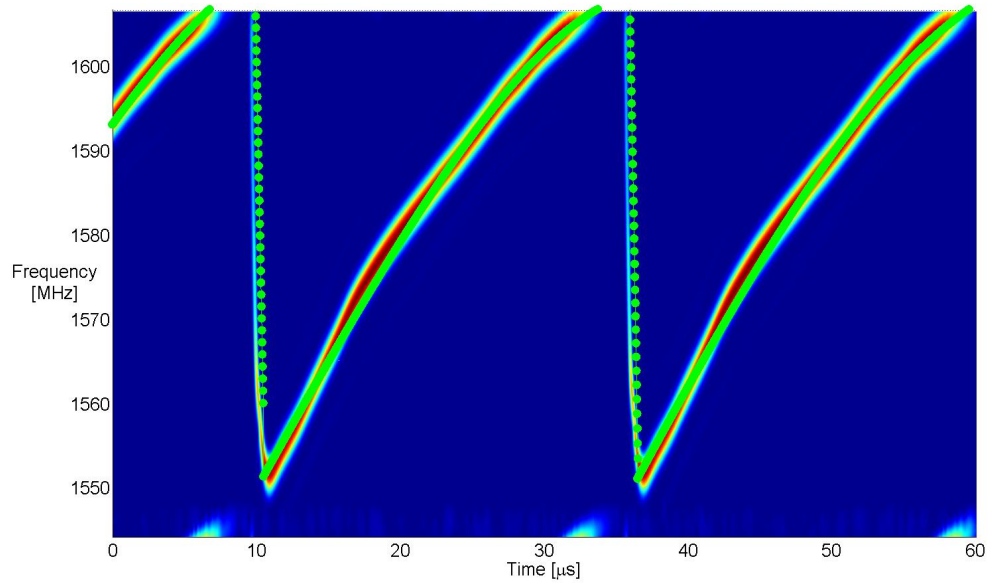

Figure 6.3: Frequency power spectra and estimated frequency of the Kalman filter (green curve) for the moderately difficult PPD to track using the developed algorithm.

the only PPD in [35] that exhibited this type of non-polynomial behavior.

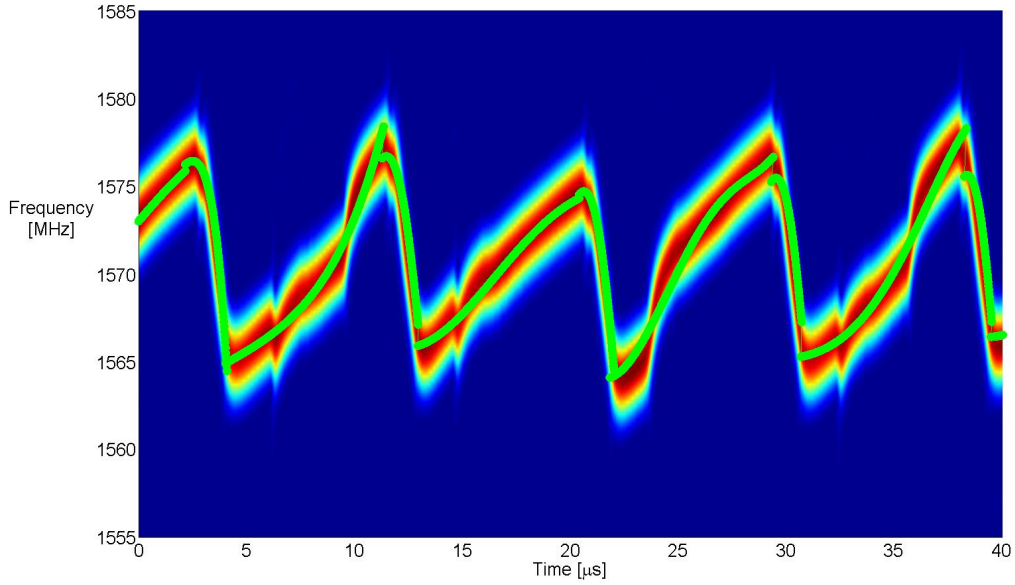

Figure 6.4: Frequency power spectra and estimated frequency of the Kalman filter (green curve) for the hardest PPD to track using the developed algorithm.

The results of Figs. 6.2–6.4 will naturally degrade with a lower sample rate and an increased noise level. That situation is considered in the next subsection using field data.

Note that Figs. 6.2–6.4 start with $t = 0$ on the time axis and that this is the initialization time of each signal tracking Kalman filter. Therefore, the entire filter initialization transient is visible in each of these figures. In fact, these look like steady-state figures, which indicate that initial transients die out very rapidly. The same is true for all Kalman filter results that will be shown in succeeding subsections.

6.7.2 Tracking Results for a Single Jammer: Field

The Kalman filter signal tracking algorithm was next applied to data from the WSMR test. The algorithm was applied to two different parts of the data set,

each with different start times and corresponding distances between the PPD and receiver station. The results make use of the full two-part acquisition algorithm from Chapter 5, in contrast to the previous subsection where only the first part of the acquisition algorithm was used.

The results of the tracking algorithm applied to the first part of the data set are shown in Fig. 6.5. In this case, the PPD was approximately 50 meters distant from the receiver station. The filter is able to track the PPD signal despite the reduced sample rate and the presence of significant RF attenuation effects. The attenuation affects in this plot are evidenced by the fades in the raw power spectra when the chirp signal approaches the top or bottom of the dark blue region that indicates the Nyquist range. Note, the state estimate is untrustworthy for the times when there is no data from the PPD inside the Nyquist bounds. The polynomials prescribe a frequency for those times, e.g., frequencies greater than approximately 1580 MHz or less than 1571 MHz in Fig. 6.5, but there is no guarantee that they are correct. Although, they appear to be reasonable.

The results of the tracking algorithm applied to the second part of the data set are shown in Fig. 6.6. In this case the PPD was approximately 1.8 kilometers distant from the receiver station. The filter is able to track the PPD signal despite the reduced sample rate, the presence of significant RF attenuation effects, and the low carrier-to-noise density ratio. This successful tracking result has been verified by comparing this scenario's estimates of the states c_1^{u}, c_1^{d}, and T to the estimates of those state provided by the first scenario with the same PPD, the one with a higher signal-to-noise density ratio. The states were a close match. The algorithm is effectively not able to acquire and track the PPD signal at a distance any greater than that listed above. Additionally, signal acquisition is not always reliable at the displayed carrier-to-noise density ratio.

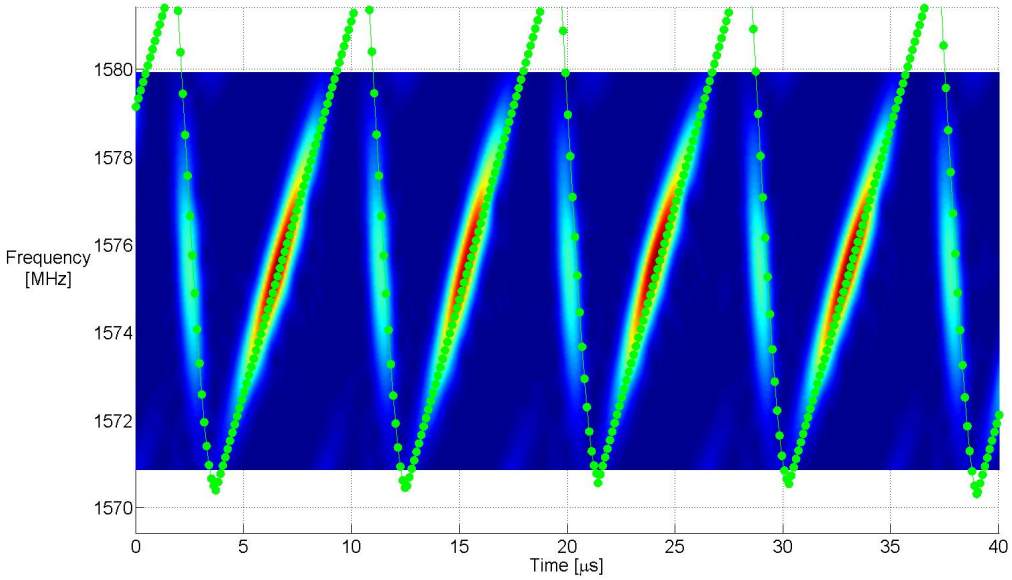

Figure 6.5: Frequency power spectra and estimated frequency of the Kalman filter (green curve) for a PPD at WSMR that was approximately 50 meters away from the recording station.

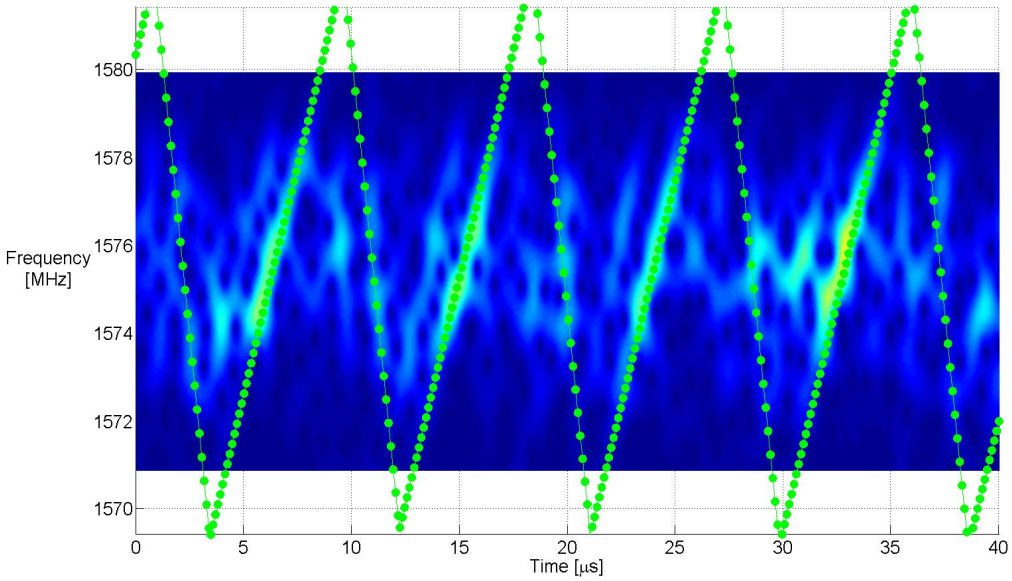

Figure 6.6: Frequency power spectra and estimated frequency of the Kalman filter (green curve) for a PPD at WSMR that was approximately 1.8 kilometers away from the recording station.

6.7.3 Tracking Results for a Multiple Jammers: Laboratory

The Kalman filter multi-jammer signal tracking algorithm has been applied to a data set that combined the RF samples of two different PPDs collected in a laboratory environment. The Kalman filter's frequency estimates of the two jamming signals are shown in Fig. (6.7). The one PPD's Kalman filter frequency estimate is shown in red and the other in green. There is close correspondence between the Kalman filter's estimated frequency time-histories and the PPD's raw power spectrum time-histories. Thus, the 2-PPD tracker is successful in this case.

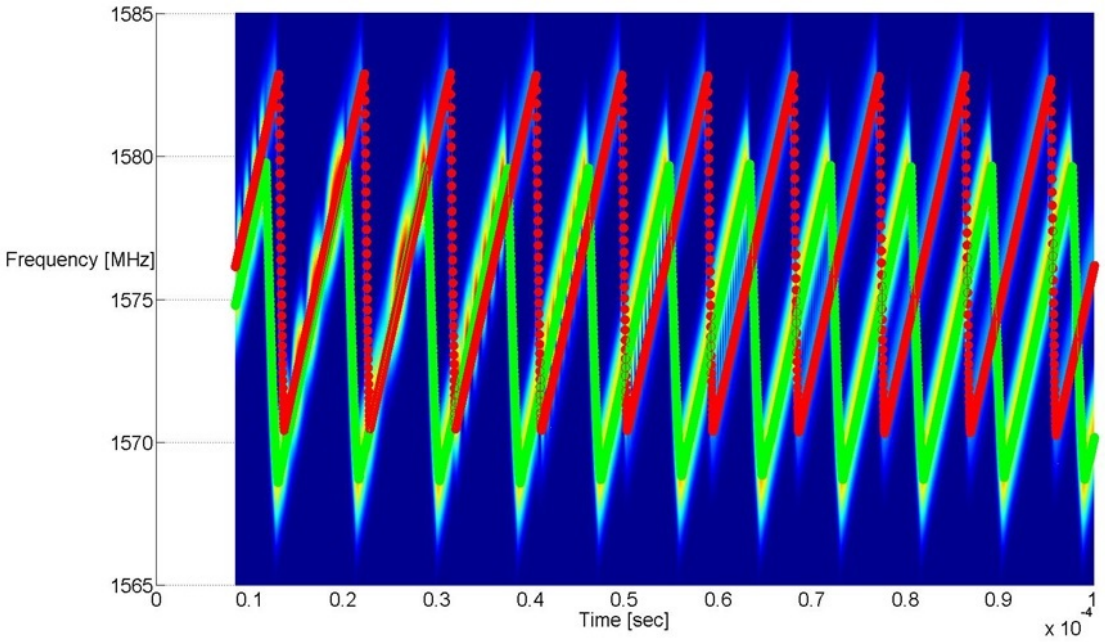

Figure 6.7: Spectra of two combined PPD laboratory data files, with the Kalman filter frequency estimates overlaid (red and green curves).

Multi-jammer signal tracking is difficult, and the successful results presented here required significant experimentation on the initial states and the tuning of the noise covariances. The tracking of multiple jammer signals may become more reliable if a different filter architecture were to be implemented, e.g., a Gaussian mixture filter or a particle filter.

6.7.4 Tracking Results for a Multiple Jammers: Field

The multi-jammer tracking algorithm has been tried using field data, but it has not been successful. There are several differences between the laboratory data and the field data, any one of which could explain this failure. First, there are significant RF filtering effects in the field data, but not in the laboratory data. Second, the field data has a reduced sample rate. Therefore, fewer measurements were used to estimate every chirp, and the chirp-signal's frequency passed outside of the system's Nyquist range. Third, the PPDs used in the two tests were different. Additionally, the encouraging multi-PPD laboratory results required "by-hand" initialization, which is unreliable. Some of the above challenges are present in the single-PPD signal tracking algorithm. However, the multi-PPD signal tracking algorithm is more sensitive to these factors. A different filter architecture, a more accurate RF filter shape estimate, a better initial state estimate, and a more accurate estimate of the system noise values might permit the developed algorithm to reliably track multiple jammers simultaneously in the field. This is an area for future study.

CHAPTER 7

SIGNAL LOCALIZATION

7.1 Jammer Geolocation Overview

This section focuses on one way that the previously developed Kalman filter PPD signal tracker can be used to facilitate PPD geolocation. The PPD geolocation algorithm used in this chapter is like that used in [37]. It is specific to the modeled chirp-style signals. The position of the PPD is estimated using the square-root information iterated extended Kalman filter discussed in Chapter 6. This new Kalman filter is developed for a new state vector, and it uses a new dynamics model and measurement model, all of which are discussed in the next few sections. The state and dynamics are intentionally designed to have low complexity. The measurements provided to the Kalman filter are the times that a signal feature arrives at each of the receiver stations. The filter assimilates the receiver data in short time-duration batches, where each batch is processed in a chirp-by-chirp manner. In the remainder of this section it is assumed that only one PPD signal is present at the receiver stations. Note, other estimation methods might be able to provide equivalent results for the same data, or equivalent results for received PPD signals with lower carrier-to-noise density ratios. The benefit of this work's array-based geolocation method is that it requires a low-inter-receiver array communication bandwidth.

7.2 Background on Signal Localization

There are many ways that a signal can be geolocated, and a full survey of the potentially applicable techniques is beyond the scope of this work. However, several relevant works are discussed here briefly. Some authors have consid-

ered using the received interference power to geolocate PPDs [17, 30]. Others have considered using an array of antennas to determine the interference signal's direction of arrival [59, 58]. Crowdsourcing approaches have also been considered [47]. Other authors have considered general purpose geolocation systems [21, 39], and some have focused specifically on the effects of urban environments [39]. One common technique uses time-aligned data streams from multiple stations to compute time-difference-of-arrival (TDOA) measurements for emitter geolocation [22, 6].

This chapters's geolocation algorithm differs from the above algorithms in the following way. It uses *a priori* knowledge of the PPD signal structure to compute time-of-arrival (TOA) measurements of a particular feature of that structure at several receiver stations. The signal feature's time of arrival is determined using the signal tracking Kalman filter's estimated state. The TOA measurements then drive another Kalman filter, one that does geolocation. This chapters's TOA method is verified using data collected from PPDs deployed at White Sands Missile Range (WSMR).

7.3 Geolocation State and Dynamics

The most important quantity in the signal geolocation problem is the emitter's position in a relevant coordinate system. Therefore, this chapter's geolocation state and dynamics will be restricted to considering this position quantity and one other required state. The coordinate system used in this work is the Earth-Centered Earth-Fixed (ECEF) coordinate system. The resulting low-order state

for PPD geolocation, $\mathbf{x}_g$, is simply:

$$\mathbf{x}_g = \begin{bmatrix} t_B^{L_1} \\ X_{ECEF} \\ Y_{ECEF} \\ Z_{ECEF} \end{bmatrix} \tag{7.1}$$

where $*_{ECEF}$ corresponds to the ECEF position for coordinate $*$. The term $t_B^{L_1}$ is the time that the broadcast PPD signal crosses the L_1 frequency at the output of the PPD transmitter antenna. This frequency crossing is the signal feature that is used for signal localization. The explanation of how to use this signal feature for geolocation, and the justification for the inclusion of $t_B^{L_1}$, is deferred until the discussion of the geolocation measurement model.

The above state could be reduced by one dimension with the assumption that the PPD is fixed to the surface of the earth, i.e., an altitude constraint. This assumption is normally valid in the PPD geolocation problem because PPDs are typically used in vehicles on a road, at sea, or are kept on the user's person as they move around on the ground. Instead of modifying the above state, the altitude constraint is enforced in the measurement model of the next section as a pseudo-measurement with a user-defined measurement noise covariance. The two methods are equivalent if the altitude measurement noise covariance is set to a very small value. Both the added pseudo-measurement and the altitude constraint reduce the number of receiver stations required for geolocation by one.

It is not immediately clear whether velocity states should be added to the state vector of Eq. (7.1). The velocity is not directly of interest, but it affects the position dynamics, and it couples with the measurements in the yet-to-be-developed geolocation measurement model. After investigation, it was found that the inclusion of the velocity states would only change the presented results

by less than a meter in position accuracy. The low error magnitude occurs for two reasons. The first reason is that the vehicle dynamics change the position state very slowly over the time-span required for accurate geolocation, e.g., less than 0.5 feet over several milliseconds. The second is that typical vehicle velocities generate only minor relative inter-receiver Doppler shifts at the receiver stations. The minor Doppler shifts have a minimal effect on the accuracy of the measurement model and the geolocation algorithm.

The first state of vector $\mathbf{x}_g$, $t_B^{L_1}$, will be re-estimated at each time step. Therefore, it has no dynamics model that relates the state at time t_k to the one at time t_{k+1}, and its process noise is effectively infinite. In information filtering terminology, the state and its associated information reset to *a priori* values of zero at every time step.

The dynamics of the PPD position state elements can be cast into state-space form, similar to Eq. (3.5). The resulting STM of the position terms is simply the identity matrix, $\mathbf{\Phi} = \mathbf{I}$. The process noise influence matrix, $\mathbf{\Gamma}$, is once again a user defined quantity, but it would be reasonable to add noise to all of the state position elements in order to allow receiver motion. This addition causes the three position states to be modeled by independent random walks. Alternatively, one could add noise in the local east-north plane and rotate that noise into ECEF coordinates. Note, the dynamics model could be modified to include vehicle dynamics. However, the more complicated dynamics would add little in the way of accuracy due to the short time-span required for geolocation. Therefore, vehicle dynamics more precise than a random walk model are not considered.

Note, this Kalman filter typically uses the chirp period as its sample period with one vector of TOA measurements per chirp period, so that there is one dynamics propagation and measurement update per chirp. In order to save computation, this Kalman filter has been run only on short windows of data, each

lasting about 1–2 millisecond and involving 30–200 chirps/samples. For a given pass of a PPD through the geolocation sensor network the Kalman filter is used to process many such windows of data, typically one every five seconds. It is reinitialized at the start of each window instead of performing a single dynamic propagation over the typical interval of about 4.998–4.999 seconds between windows. There is negligible loss of accuracy due to these reinitializations because of the system's excellent observability and crude dynamic model.

7.4 Geolocation Measurement Model Considerations

Two common types of measurements used for array-based emitter geolocation are the received signal TDOAs and the TOAs. The measurements are computed using the data collected from an array of multiple recording stations, such as those shown in Fig. 2.12. The TDOA measurements are typically computed using the numerical cross-correlation of two time-aligned vectors of received RF samples, which are collected simultaneously at different receiver stations. The numerical correlation has a peak that is offset from zero by the TDOA that is caused by the relative positions of the emitter and the pair of receiver stations. The TOA measurements are typically computed using the time that a particular signal feature is measured at each station. The signal feature will arrive at a different time at each station. The time of arrival is dependent on the relative positions of the emitter and receiver stations. The TOA measurement relates to the TDOA measurement by a differencing of the signal arrival times at the separate stations.

There are several positive and negative aspects of the TDOA and TOA measurements that should be considered before selecting which to use in the geolocation measurement model. One positive aspect of the TDOA measurement is

that it does not require significant knowledge of the signal structure. Additionally, it can use a large amount of RF data to increase the measurement sensitivity. The corresponding negative aspect of the TDOA measurement is that it can require a significant amount of inter-station communication bandwidth to transmit the raw data that is required to compute the numerical cross-correlations between the different stations. One positive aspect of the TOA measurement is that it requires very little inter-station communication bandwidth to transmit its geolocation data between different stations. The bandwidth requirement is reduced because the TOA measurement is generated after processing the raw RF samples. The corresponding negative of the TOA measurement is that some amount of preprocessing must be applied at each station before geolocation can occur.

This chapter uses the TOA measurement model for two reasons. The first reason is that the PPDs considered in this work broadcast a significant amount of power. Therefore, the increased sensitivity of the simplistic TDOA model is not necessary for this geolocation problem. The second reason is that the signal tracking Kalman filter provides the necessary algorithms for preprocessing the data for use in the TOA measurement model.

7.5 Geolocation Measurement Model

The signal feature selected to compute the TOA measurement is the time that the *received* PPD chirp signal crosses the GPS L_1 frequency during the frequency ramp-up, denoted $t_R^{L_1}$. This time can be determined very precisely using the PPD frequency polynomial signal model and the Kalman filter signal tracker that was developed earlier in this thesis. The determination starts by finding the local time of L_1 crossing based on $\mathbf{x}$. Before transmitting this time to another

receiver, however, it must be mapped to a common time of the receiver array.

There are many ways that the stations' local times can be mapped to a common time. The current work uses the GPS signal as a common timing reference. This might appear to be counter-intuitive, as the PPDs jam GPS receivers. However, a shielded antenna was connected to the second USRP at each station. That antenna was used to collect relatively clean L-band GPS data. These data were processed to determine GPS time and thus synchronize all of the stations. The processing uses standard GPS techniques to determine a receiver clock offset time-history at each station. This offset time-history is interpolated to each L_1 crossing time of the chirp signal and is used to correct that crossing time, and yield synchronized time of crossing as an absolute GPS time.

Note, ovenized crystal oscillators were used at all of the stations. Therefore, the rate of drift of the receiver clock offsets is typically small, on the order of $0.018\,\mu$s/second. The relative smallness of these drift rates is important because the drift rate multiplied by 1.57542 GHz constitutes a direct error in the definition of the f_{L_1} frequency crossing. This error translates directly into a TOA error after division by the slope of the particular PPD's frequency versus time curve. Fortunately, the f_{L_1} errors are low enough, and the PPD frequency slopes high enough, to keep these errors from being significant.

The vector of measurements provided to the Kalman filter for geolocation purposes is:

$$\mathbf{z}_{\mathrm{g}} = \begin{bmatrix} t_{R,1}^{L_1} \\ \vdots \\ t_{R,N_S}^{L_1} \\ z_{\mathrm{alt}} \end{bmatrix} \tag{7.2}$$

where $t_{R,i}^{L_1}$ is the GPS arrival time of the chirp signal feature at receiver station i in units of seconds, and z_{alt} is the *a priori* known altitude pseudo-measurement.

A parameter vector $\mathbf{p}$ must be defined before the measurement model can be presented:

$$\mathbf{p} = \begin{bmatrix} \mathrm{X}_1 \\ \mathrm{Y}_1 \\ \mathrm{Z}_1 \\ \vdots \\ \mathrm{X}_{N_\mathrm{S}} \\ \mathrm{Y}_{N_\mathrm{S}} \\ \mathrm{Z}_{N_\mathrm{S}} \end{bmatrix} \tag{7.3}$$

where X_i, Y_i, and Z_i are, respectively, the ECEF x, y, and z positions of the antennas at receiver station i (not the imaginary number i). N_S is the total number of receiver stations used in the TOA geolocation model. The results section uses $N_\mathrm{S} = 4$.

The TOA geolocation measurement model defines the relationship between the state vector $\mathbf{x}_\mathrm{g}$, the parameters $\mathbf{p}$, and the time of signal feature arrival for receiver i, $t_{R,i}^{\mathrm{L}_1}$, through the following simple pseudorange equation:

$$\mathrm{c}t_{R,i}^{\mathrm{L}_1} = \mathrm{c}t_B^{\mathrm{L}_1} + \rho_i\left(\mathbf{x}_\mathrm{g}, \mathbf{p}\right) \tag{7.4}$$

for each station $i = 1...N_\mathrm{S}$. The term c is the speed of light in units of meters per second. The term $\rho_i\left(\mathbf{x}_\mathrm{g}, \mathbf{p}\right)$ is the distance between the PPD and receiver i in units of meters:

$$\rho_i\left(\mathbf{x}_\mathrm{g}, \mathbf{p}\right) = \sqrt{(\mathrm{X}_i - \mathrm{X}_\mathrm{ECEF})^2 + (\mathrm{Y}_i - \mathrm{Y}_\mathrm{ECEF})^2 + (\mathrm{Z}_i - \mathrm{Z}_\mathrm{ECEF})^2} \tag{7.5}$$

where all of the above terms have been defined previously. More terms could be added to Eq. (7.4) to account for other effects, such as the refractivity effects of the atmosphere that cause the signal to travel at a speed less than c—as is commonly done in GNSS radio-navigation, but such terms are not necessary for this work's developments.

The above model has not yet addressed the measurement noise that is a part of every real system. The TOA measurement, $t_{R,i}^{\mathrm{L1}}$ in Eq. (7.4), will include noise that is a function of many different things, in particular the RF sample noise, unmodeled effects, simplifying assumptions, and clock synchronization errors between the various receivers. For simplicity, the noise is assumed to be added linearly to the TOA measurement for station *i*:

$$t_{R_i}^{\mathrm{L1}} = t_{R_i,\mathrm{true}}^{\mathrm{L1}} + n_{t_{\mathrm{L_1}},i} \tag{7.6}$$

where $n_{t_{\mathrm{L_1}},i}$ is the time of arrival measurement noise for receiver *i*. A full analysis of the statistics of the noise in this type of system would be very complicated and it is beyond the scope of the current work. Therefore, the noise is approximated as a Gaussian random variable with the following statistics:

$$\mathbf{n}_{t_{\mathrm{L_1}}} \sim \mathcal{N}(\mathbf{0}, \mathbf{G}) \tag{7.7}$$

where $\mathbf{n}_{t_{\mathrm{L_1}}}$ is an N_{S}-by-1 column vector that is composed of the separate $n_{t_{\mathrm{L_1}},i}$ terms and $\mathbf{G}$ is a user-defined positive semidefinite symmetric covariance matrix. The value of $\mathbf{G}$ can be regarded as a tuning parameter, typically a diagonal matrix is used.

The final TOA geolocation measurement model can be written in the standard nonlinear Kalman filter measurement model form:

$$\mathbf{z}_{\mathrm{g}} = \begin{bmatrix} \mathrm{h}_{\mathrm{g},1}(\mathbf{x}_{\mathrm{g}}; \mathbf{p}) + n_{t_{\mathrm{L_1}},1} \\ \vdots \\ \mathrm{h}_{\mathrm{g},N_{\mathrm{S}}}(\mathbf{x}_{\mathrm{g}}; \mathbf{p}) + n_{t_{\mathrm{L_1}},N_{\mathrm{S}}} \\ \mathrm{h}_{\mathrm{alt}}(\mathbf{x}_{\mathrm{g}}) \end{bmatrix} \tag{7.8}$$

where:

$$\mathrm{h}_{\mathrm{g},i}(\mathbf{x}_{\mathrm{g}}; \mathbf{p}) = \frac{1}{c}\left[c t_B^{\mathrm{L1}} + \rho_i\left(\mathbf{x}_{\mathrm{g}}, \mathbf{p}\right)\right] \tag{7.9}$$

where $h_{alt}(\mathbf{x}_g)$ is the altitude with respect to the WGS-84 ellipsoid [16, 34]. Its formula is not presented in this thesis.

The above measurement model is nonlinear, and it is assumed that an EKF can be implemented using the above model. The computation of the EKF's Taylor series expansion of Eq. (7.8) is straight-forward, but it has been omitted for the sake of brevity.

7.6 Geolocation Results: Field

The Kalman filter signal tracker with the automated initialization method and the Kalman filter TOA geolocation algorithm have been applied to one set of PPD data collected at several stations at WSMR. The following results use batches of data at 5 second intervals, where each data batch spans approximately 1 ms. Each batch is initialized with a starting position in the center of the receiver array and uses no information from the previous batches. The use of *a priori* information might improve the results, but it would also cause undesired correlations between the errors of each batch's position estimates.

The geolocation results are shown in Fig 7.1. The red squares are the receiver stations, the blue dots are the IMU position estimates that are assumed to be the true position, and the green dots are the TOA-based position estimates from the Kalman filter. The average error magnitude in the two dimensional East-North coordinate system is approximately 8.7 meters, and the average error in the full ECEF coordinate system is approximately 12 meters. The use of the Kalman filter signal tracker shows an improvement over the ad-hoc method of [37]. That method produced an average East-North error magnitued of 15m, which is almost twice the error magnitude achieved using TOA measurements from the signal tracking Kalman filter.

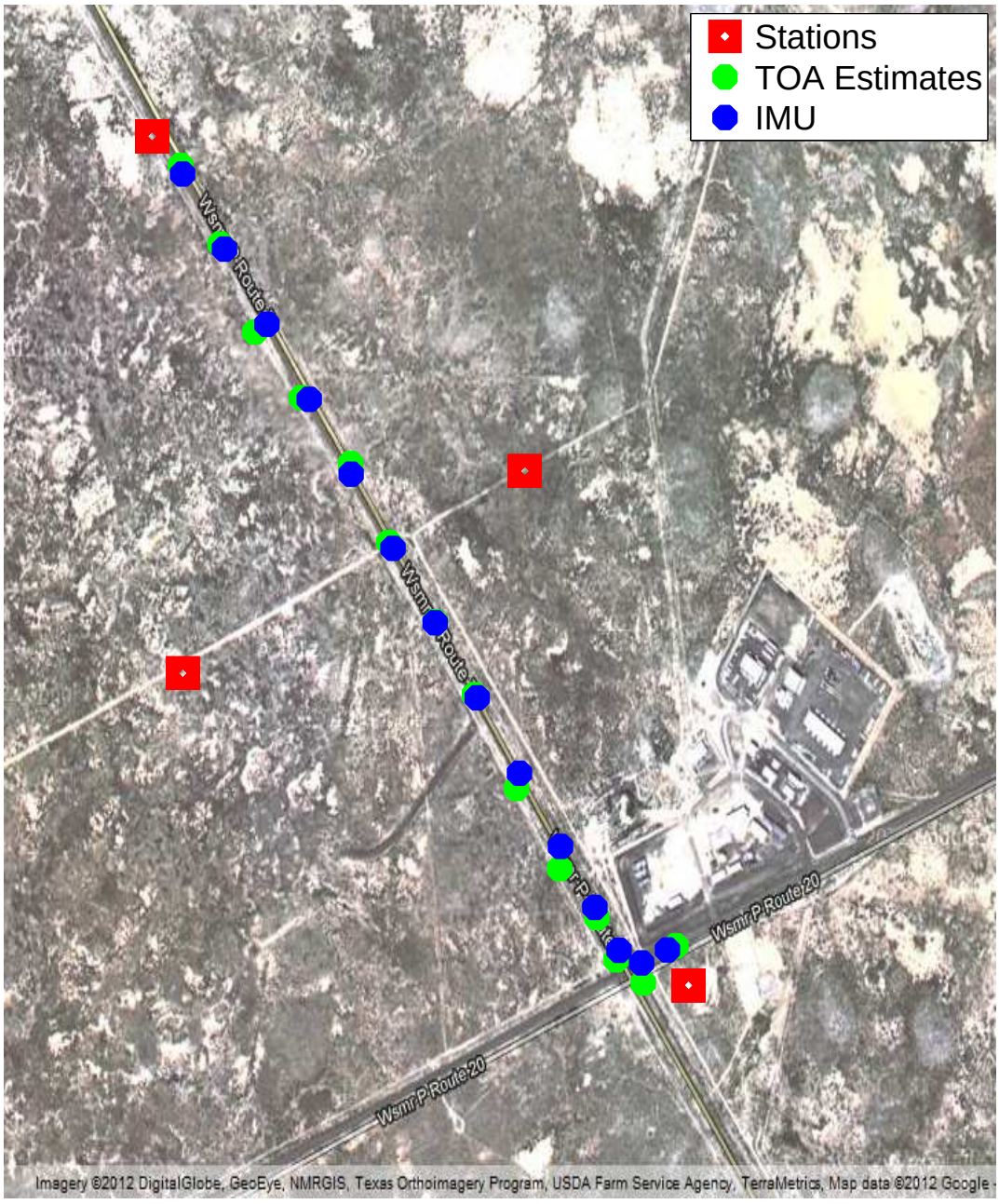

Figure 7.1: Results of the Kalman filter geolocation algorithm applied to data collected at WSMR and post-processed using the Kalman filter signal tracker with the absolute value measurement model.

7.7 Practical Considerations

Real-world implementations of the proposed system, such as the one that produced the above results, may have intermittent blackouts due to non-ideal shielding of the second GPS antenna. In fact, such blackouts occurred for the data collected in this campaign. In this situation, the geolocation algorithm is not able to maintain the best possible time synchronization between the various receivers. Instead, it is forced to rely on its best estimate of GPS time on either side of the blackout and to "fly-wheel" through the blackout using an interpolation. The accuracy of the geolocation algorithm will suffer if the drift of the receivers' clocks is inaccurately modeled by the interpolation. If real-time operation is required, then the compensation for GPS outages must be causal. In this situation, interpolation is replaced by extrapolation from the most recent time of GPS availability. In the present work, the longest GPS outage during the one minute geolocation interval was approximately 30 seconds, and interpolation has been used.

The error introduced due to this drift is dependent on the clock quality. For example, this work's data collection efforts used ovenized crystal oscillators (OCXO). This type of oscillator is a moderately stable clock. A truth-model simulation using the Allan variances of a typical OCXO was conducted using the same receiver spacing as that shown in Fig. 7.1. The resulting PPD position errors due to a 1 minute extrapolated clock drift, which is the approximate amount of time that it took the PPD to move through the array, were on the order of 5 meters. The final error of 8.7 meters might be partially attributable to the clock drift during the GPS black-outs when the PPDs were very close to the receiver stations. The remaining error might be caused by the ignored effects of Doppler shift, noise in the system, and other simplifying assumptions.

CHAPTER 8

CONCLUSION

This dissertation considered the technical aspects of the so-called personal privacy devices (PPDs) that enable technical laymen to jam all GNSS devices in their vicinity. It developed models of these PPD's signals and a variety of model-based algorithms for processing these signals. The first contribution has been the determination of the signal characteristics of the PDDs provided by the U.S. Department of Homeland Security. The second contribution has been a new high-fidelity state-space model of the PPDs' chirp-style signals. The validity of the model has been verified by the Kalman filter signal tracking algorithm. The third contribution has been a new PPD signal detection algorithm. The detection algorithm has been designed, optimized for computation speed, implemented, and tested on several real jamming signals. The theoretical and experimental probabilities of detection has been compared and found to match well. The fourth contribution has been an FFT-based two-step PPD state acquisition algorithm; it uses a rough acquisition, followed by a fine acquisition. The acquisition algorithm has been implemented successfully on several real PPD signals; two laboratory signals and one field signal. The acquisition algorithm also has been applied several times in conjunction with the final tracking algorithm and PPD geolocation algorithm. The fifth contribution has been a signal tracking Kalman filter. The filter has been applied to multiple data sets; three laboratory data sets and one field data set. The signal tracking filter was also applied successfully at multiple times and at multiple different stations in support of the final geolocation algorithm. The sixth contribution has been a geolocation algorithm that operates with low inter-node communication bandwidth between the receivers of a PPD gelocation array. The geolocation algorithm has been shown to work well on a set of field data collected at four receiver stations

at White Sands Missile Range.

BIBLIOGRAPHY

[1] M. Adjrad, A. Beloucharni, and A. Ouldali. Estimation of chirp signal parameters using state space modelization by incorporating spatial information. In *Signal Processing and Its Applications, 2003. Proceedings. Seventh International Symposium on*, volume 2, pages 531–534, 2003.

[2] M. Adjrad and A. Belouchrani. Estimation of multicomponent polynomial-phase signals impinging on a multisensor array using state–space modeling. *Signal Processing, IEEE Transactions on*, 55(1):32–45, 2007.

[3] D. Aloi and A. Steffes. Vehicle impact on personal privacy device (ppd) performance. In *Proceedings of the 25th International Technical Meeting of The Satellite Division of the Institute of Navigation (ION GNSS 2012)*, pages 3558–3562, Sept. 2012. Nashville, TN.

[4] N. Balachandran and C. Creusere. Classification of chirps using hidden markov models. In *Signals, Systems and Computers, 2006. ACSSC '06. Fortieth Asilomar Conference on*, pages 545–549, 2006.

[5] Y. Bar-Shalom, R. X. Li, and T. Kirubarajan. *Estimation with Applications to Tracking and Navigation*. John Wiley & Sons, 605 Third Avenue, New York, NY, 1st edition, 2001.

[6] J.A. Bhatti, T.E. Humphreys, and B.M. Ledvina. Development and demonstration of a tdoa-based gnss interference signal localization system. In *Position Location and Navigation Symposium (PLANS), 2012 IEEE/ION*, pages 455–469, April 2012.

[7] G. J. Bierman. *Factorization Methods for Discrete Sequential Estimation*. Dover Publications, 31 East 2nd Street, Mineola, NY, 1st edition, 1977.

[8] B. Boashash. Estimating and interpreting the instantaneous frequency of a signal–part 2. algorithms and applications. *Proceedings of the IEEE*, 80(4):540–568, 1992.

[9] D. Borio, J. Fortuny-Guasch, and C. O'Driscoll. Characterization of gnss jammers, May 2013.

[10] A. Charles. Car theives using gps jammers. online, Feb. 2010. TheGaurdian.com., Guardian news and Media.

[11] E. Chassande-Mottin and P. Flandrin. On the timefrequency detection of chirps1. *Applied and Computational Harmonic Analysis*, 6(2):252 – 281, 1999.

[12] E. Chassande-Mottin and A. Pai. Discrete time and frequency wigner-ville distribution: Moyal's formula and aliasing. *Signal Processing Letters, IEEE*, 12(7):508–511, 2005.

[13] K.Q.Z. Chiang and M.L. Psiaki. Kalman filter tracking of limb scan signal using a bank of correlators. *Aerospace and Electronic Systems, IEEE Transactions on*, 49(1):118–133, Jan 2013.

[14] F.S. Cohen, S. Kadambe, and G.F. Boudreaux-Bartels. Tracking of unknown nonstationary chirp signals using unsupervised clustering in the wigner distribution space. *Signal Processing, IEEE Transactions on*, 41(11):3085–3101, 1993.

[15] G. Cornelia, M. Lucian, and R. Romulus. Detection and estimation of linear fm signals. In *Signals, Circuits and Systems, 2005. ISSCS 2005. International Symposium on*, volume 2, pages 705–708 Vol. 2, 2005.

[16] BL Decker. World geodetic system 1984. Technical report, DTIC Document, 1986.

[17] D. Fontanella, R. Bauernfeind, and B. Eissfeller. In-car gnss jammer localization with a vehicular ad-hoc network. In *Proceedings of the 25th International Technical Meeting of The Satellite Division of the Institute of Navigation (ION GNSS 2012)*, pages 2885–2893, Sept. 2012. Nashville, TN.

[18] J. Gal, A. Campeanu, and I. Nafornita. Estimation of chirp signals in gaussian noise by kalman filtering. In *Signals, Circuits and Systems, 2007. ISSCS 2007. International Symposium on*, volume 1, pages 1–4, 2007.

[19] J. Gal, A. Campeanu, and I. Nafornita. The estimation of chirp signals parameters by an extended kalman filtering algorithm. In *Signals, Circuits and Systems (ISSCS), 2011 10th International Symposium on*, pages 1–4, 2011.

[20] G. Gao, K. Gunning, T. Walter, and P. Enge. Impact of personal privacy device for waas aviation users. In *Proceedings of the 25th International Technical Meeting of The Satellite Division of the Institute of Navigation (ION GNSS 2012)*, pages 235–241, Sept. 2012. Nashville, TN.

[21] K. G. Gromov. *GIDL: Generalized Interference Detection and Localization System*. PhD thesis, Standford University, March 2002.

[22] O. Isoz, A. T. Balaei, and D. Akos. Interference detection and localization

in the gps l1 band. In *Proceedings of the ION ITM*, pages 925–929, Jan. 2010. San Diego, CA.

[23] F.A. Jenet and T.A. Prince. Detection of variable frequency signals using a fast chirp transform. *Physical Review D*, 62(12):1–12, 2000.

[24] W.E. Kaakour, M. Guglielmi, J. M. Piasco, and E. Le Carpentier. Two identification methods of chirp parameters using state space models. In *Digital Signal Processing Proceedings, 1997. DSP 97., 1997 13th International Conference on*, volume 2, pages 903–906 vol.2, 1997.

[25] S. Kay and G.F. Boudreaux-Bartels. On the optimality of the wigner distribution for detection. In *Acoustics, Speech, and Signal Processing, IEEE International Conference on ICASSP '85.*, volume 10, pages 1017–1020, 1985.

[26] Thomas Kraus, Roland Bauernfeind, and Bernd Eissfeller. Survey of in-car jammers - analysis and modeling of the rf signals and if samples (suitable for active signal cancellation). In *Proceedings of the ION GNSS 2011*, pages 430–435, Sept. 20-23, 2011. Portland, OR.

[27] S. Krishnan and R.M. Rangayyan. Detection of chirp and other components in the time-frequency plane using the hough and radon transforms. In *Communications, Computers and Signal Processing, 1997. 10 Years PACRIM 1987-1997 - Networking the Pacific Rim. 1997 IEEE Pacific Rim Conference on*, volume 1, pages 138–141 vol.1, 1997.

[28] Hsiang-Tsun Li and P.M. Djurie. Mmse estimation of nonlinear parameters of multiple linear/quadratic chirps. *Signal Processing, IEEE Transactions on*, 46(3):796–800, 1998.

[29] Weiping Li. Wigner distribution method equivalent to dechirp method for detecting a chirp signal. *Acoustics, Speech and Signal Processing, IEEE Transactions on*, 35(8):1210–1211, 1987.

[30] J. Lindstrom, D. M. Akos, O. Isoz, and M. Junered. Gnss interference detection and localization using a network of low-cost front-end modules. In *Proceedings of the ION GNSS Meeting*, pages 1165–1172, Sept., 25-28 2007. Fort Worth, TX.

[31] Yufeng Lu, R. Demirli, G. Cardoso, and J. Saniie. A successive parameter estimation algorithm for chirplet signal decomposition. *Ultrasonics, Ferroelectrics and Frequency Control, IEEE Transactions on*, 53(11):2121–2131, 2006.

[32] B.R. Mahafza. *Introduction to Radar Analysis*. CRC press, 1998.

[33] B.R. Mahafza. *Radar Signal Analysis and Processing Usin MATLAB*. CRC Press, second edition, 2009.

[34] Pratap Misra and Per Enge. *Global Positioning System: Signals, Measurements, and Performance*, pages 53–58. Ganga-Jamuna Press, Lincoln, Massachusetts, 2nd edition, 2006.

[35] R. H. Mitch, R. C. Dougherty, M. L. Psiaki, S. P. Powell, B. W. O'Hanlon, J. A. Bhatti, and T. E. Humphreys. Signal characteristics of civil gps jammers. In *Proceedings of the ION GNSS 2011*, pages 1907–1919, Sept. 20-23, 2011. Portland, OR.

[36] R. H. Mitch, R. C. Dougherty, M. L. Psiaki, S. P. Powell, B. W. O'Hanlon, J. A. Bhatti, and T. E. Humphreys. Know your enemy. *GPS World*, 23(1):64, 2012.

[37] R. H. Mitch, M. L. Psiaki, B. W. O'Hanlon, S. P. Powell, and J. A. Bhatti. Civilian gps jammer signal tracking and geolocation. In *Proceedings of the ION GNSS 2012*, pages 2901–2920, Sept. 18-21, 2012. Nashville, TN.

[38] R.H. Mitch, M.L. Psiaki, S.P. Powell, and B.W. O'Hanlon. Signal acquisition and tracking of chirp-style gps jammers. In *Proceedings of the ION GNSS+ 2013*, pages 2893–2909, Sept., 2013. Nashville, TN.

[39] M. B. Montminy. Passive geolocation of low-power emitters in urban environments using tdoa. Master's thesis, Air Force Institute of Technology, March 2007.

[40] A.A. Nashat and Lonnie C. Ludeman. Detection and estimation of chirp signals using state space representation. In *Circuits and Systems, 1992. ISCAS '92. Proceedings., 1992 IEEE International Symposium on*, volume 3, pages 1609–1612 vol.3, 1992.

[41] F.D. Nunes and F.M.G. Sousa. Jamming detection in gnss signals using the sample covariance matrix. In *Satellite Navigation Technologies and European Workshop on GNSS Signals and Signal Processing, (NAVITEC), 2012 6th ESA Workshop on*, pages 1–8, 2012.

[42] A. Papandreou, S.M. Kay, and G. Boudreaux-Bartels. The use of hyperbolic time-frequency representations for optimum detection and parameter estimation of hyperbolic chirps. In *Time-Frequency and Time-Scale Analysis,*

1994., Proceedings of the IEEE-SP International Symposium on, pages 369–372, 1994.

[43] B. Potter, K. Shallberg, and J. Grabowski. Personal privacy device interference in the waas. In *Proceedings of the 25th International Technical Meeting of The Satellite Division of the Institute of Navigation (ION GNSS 2012)*, pages 2868–2874, Sept. 2012. Nashville, TN.

[44] M. L. Psiaki. Block acquisition of weak gps signals in a software receiver. In *Proceedings of the ION GPS 2001*, pages 2838–2850, 2001.

[45] A.W. Rihaczek. *Principles of High-Resolution Radar*. McGraw-Hill Book Company, 1969.

[46] S.B. Sahay, D. Pande, V. Gadre, and P. Sohani. Model-independent approach for chirp parameter estimation employing collection of filters. In *Communications (NCC), 2012 National Conference on*, pages 1–5, 2012.

[47] L. Scott. J911: The case for fast jammer detection and location using crowdsourcing approaches. In *Proceedings of the ION GNSS 2011*, pages 1931–1940, Portland, OR, Sept. 2011.

[48] R. Sharif and S. Abeysekera. Efficient wideband signal parameter estimation using a radon-ambiguity transform slice. *Aerospace and Electronic Systems, IEEE Transactions on*, 43(2):673–688, 2007.

[49] P. Shui, Z. Bao, and H. Su. Nonparametric detection of fm signals using time-frequency ridge energy. *Signal Processing, IEEE Transactions on*, 56(5):1749–1760, 2008.

[50] Spilker, J. Jr. and Van Dierendonck, A. J. *Global Positioning System: Theory and Applications Volume 2*. American Institute of Aeronautics and Astronautics, Inc., Washington, DC, 1 edition, 1996.

[51] J. Torres, A. Vega, S. Torres, and D. Andina. Chirp detection through discrete wavelet transform. In *Proceedings of the World Scientific and Engineering Academy and Society Conference on Signal Processing, Robotics And Automation (ISPRA'02)*, volume 1975, pages 121–167, 1971.

[52] V.C. Vannicola, T.D. Hale, M.C. Wicks, and P. Antonik. Ambiguity function analysis for the chirp diverse waveform (cdw). In *Radar Conference, 2000. The Record of the IEEE 2000 International*, pages 666–671, 2000.

[53] M. Wang, A.K. Chan, and C.K. Chui. Linear frequency-modulated signal detection using radon-ambiguity transform. *Signal Processing, IEEE Transactions on*, 46(3):571–586, 1998.

[54] P. Wang, H. Li, I. Djurovic, and B. Himed. Integrated cubic phase function for linear fm signal analysis. *Aerospace and Electronic Systems, IEEE Transactions on*, 46(3):963–977, 2010.

[55] D.R. Wehner. *High-Resolution Radar*. Artech House, second edition, 1995. Boston.

[56] A. Wojtkiewicz and R. Rytel-Andrianik. Optimal detection and estimation in fmcw radar. In *Microwaves, Radar and Wireless Communications, 2002. MIKON-2002. 14th International Conference on*, volume 3, pages 778–781 vol.3, 2002.

[57] X. Xia. Discrete chirp-fourier transform and its application to chirp rate estimation. *Signal Processing, IEEE Transactions on*, 48(11):3122–3133, 2000.

[58] Z. Xu and M. Trinkle. Weak gps interference direction of arrival estimation using gps signal cancellation. In *Proceedings of the 25th International Technical Meeting of The Satellite Division of the Institute of Navigation (ION GNSS 2012)*, pages 2940–2945, Sept. 2012. Nashville, TN.

[59] X. Yuan, J. Wan, Z. Cheng, H. Liu, and G. Li. A novel gnss interference suppression and doa estimation processing system. In *Transportation, Mechanical, and Electrical Engineering (TMEE), 2011 International Conference on*, pages 1568–1571, Dec 2011.

[60] R. Zarifeh, N. Alinier, S. Krishnan, and A. Anpalagan. Interference detection in spread spectrum communication using polynomial phase transform. In *Communications, 2007. ICC '07. IEEE International Conference on*, pages 2979–2984, 2007.